Summer 2016

Development and Implementation of a Propeller Test Capability for Gl-10 "Greased Lightning" Propeller Design

Brian Edward Duvall
Old Dominion University

DEVELOPMENT AND IMPLEMENTATION OF A PROPELLER TEST CAPABILITY FOR GL-10 "GREASED LIGHTNING" PROPELLER DESIGN

by

Brian Edward Duvall
B.S. May 2014, Old Dominion University

A Thesis Submitted to the Faculty of
Old Dominion University in Partial Fulfillment of the
Requirements for the Degree of

MASTER OF SCIENCE

AEROSPACE ENGINEERING

OLD DOMINION UNIVERSITY
August 2016

Approved By:

Dr. Drew Landman (Director)

Dr. Colin Britcher (Member)

Dr. Thomas Alberts (Member)

ABSTRACT

DEVELOPMENT AND IMPLEMENTATION OF A PROPELLER TEST CAPABILITY FOR GL-10 "GREASED LIGHTNING" PROPELLER DESIGN

Brian Edward Duvall
Old Dominion University, 2016
Director: Dr. Drew Landman

Interest in small unmanned aerial vehicles has increased dramatically in recent years. Hybrid vehicles which allow forward flight as a fixed wing aircraft and a true vertical landing capability have always had applications. Management of the available energy and noise associated with electric propeller propulsion systems presents many challenges. NASA Langley has developed the Greased Lightning 10 (GL-10) vertical takeoff, unmanned aerial vehicle with ten individual motors and propellers. All are used for propulsion during takeoff and contribute to acoustic noise pollution which is an identified nuisance to the surrounding users. A propeller test capability was developed to gain an understanding of how the noise can be reduced while meeting minimum thrust requirements. The designed propeller test stand allowed for various commercially available propellers to be tested for potential direct replacement of the current GL-10 propellers and also supported testing of a newly designed propeller provided by the Georgia Institute of Technology. Results from the test program provided insight as to which factors affect the noise as well as performance characteristics. The outcome of the research effort showed that the current GL-10 propeller still represents the best choice of all the candidate propellers tested.

ACKNOWLEDGMENTS

There are many people who have aided in the completion of this thesis project. I would like to thank my advisor, Dr. Drew Landman, for his time spent helping me, Dr. Colin Britcher who co-advised me and made this project possible, and Dr. Thomas Alberts for being on my committee. Charles Lowe, is another important contributor who showed me how to setup the microphones and taught me about acoustics. Also, I would like thank the Old Dominion University 2016 “Greased Lightning-10” senior design group for designing and building the propeller test stand. This includes William Foronda, Alfredo Deschamps, Robert Hughes, Joshua Cruz, Raul Gomez, Larry Johnson, Mihir Patel, and Arthur Terlecki. Lastly, I would like to thank my parents for supporting me over the years.

NOMENCLATURE

C_T	Coefficient of thrust
C_Q	Coefficient of torque
C_P	Coefficient of power
J	Advance ratio
η	Efficiency
T	Thrust, lbf
Q	Torque, in-lbf
ρ	Density, slugs/ ft^3
n	Revolution per second, rev/sec
D	Propeller diameter, ft
V	Velocity, ft/sec
t_c	Time duration of noise cycle, sec
Δp	Microphone pressure differential, Pa
$\bar{p}^2$	Mean square average, Pa
p_{ref}	Reference pressure, Pa
SPL	Sound Pressure Level, db
$\bar{P}_A{}^2$	A-Weighted mean square average, Pa
SPLA	A-Weighted sound pressure level, db
n	Normal vector, ft
A	Airscrew disc area, ft^2
t	Time, sec
S	Cross Sectional Area of the Slipstream, ft^2
C	Cross Sectional Area of the Wind Tunnel, ft^2
u_1	Velocity from the Propeller Slipstream, ft/sec

u_o	Velocity between the Propeller Slipstream and the Wind Tunnel Wall, ft/sec
u	Velocity at the Propeller, ft/sec
p	Freestream Pressure, lbf/in^2
p_1	Pressure between the Propeller Slipstream and the Wind Tunnel Wall, lbf/in^2
F	Force on Control Volume, lbf
V'	Corrected Freestream Velocity, ft/sec
α	Propeller Area Divided by Wind Tunnel Cross Sectional Area
τ	Thrust Divided by Linear Momentum through Control Volume
r	General Data Reduction Equation
b_x	Systematic Error for x
b_y	Systematic Error for y
N	Number of Samples
X_i	Measured Value
$\bar{X}$	Average of Measured Value

TABLE OF CONTENTS

Page

LIST OF FIGURES

Figure Page

Figure Page

Figure Page

Figure Page

Figure Page

CHAPTER 1 - INTRODUCTION

Performance characteristics of small scale propellers are important when trying to optimize for thrust, acoustics and efficiency. This project focuses on understanding the propeller performance characteristics for use on the so-called "Greased Lightning 10" (GL-10) aircraft. The GL-10 is a vertical takeoff, unmanned aerial vehicle prototype of the National Air and Space Administration (NASA). The GL-10 model has eight motors along the leading edge of the wing that pivots to allow for forward versus vertical flight. There are also two motors on a similar pivoting tail for support during a vertical takeoff or landing. Figure 1 shows the GL-10 during a vertical takeoff.

Figure 1- Greased Lightning 10

Due to the amount of power these ten motors will be drawing during takeoff and the noise production, it is important that all ten propellers are optimized. This includes having sufficient thrust while taking off vertically and having acceptable efficiency at the same time. The thrust needs to be maximized to have the ability to lift more weight while maintaining control in the vertical flight mode. Not all of the motors will be able to run at their maximum thrust at one time. If all of the motors are allowed to run at max throttle to increase the payload ability there is no remaining margin for control during a vertical takeoff [1]. For instance, when countering a gust, the model will not have the ability to counteract the disturbance with increased motor power since all of the motors are already at their maximum throttle.

The impetus for this research project arose because during vertical takeoffs and hover the current propellers generate excessive noise. The current propeller is the Aeronaut 16×8 with three blades. This propeller allows the GL-10 to lift useful payloads and possibly deliver supplies to an area without drawing attention with its noise signature if it can be reduced. There is a great interest in developing a propeller design that is acoustically quieter.

This project was a joint project with Georgia Institute of Technology. The task at ODU focused on the design and implementation of a propeller test stand to collect data from different propellers. Georgia Tech was tasked with designing a new optimized propeller with the goal of meeting or exceeding the current thrust performance and lowering the noise. The overarching design goal for the propeller test stand was to measure how much thrust and torque a given propeller generates at a given flight speed and angular velocity, and at the same time accommodate the measurement of the acoustic noise. In addition, portions of the test stand were adapted for use in an anechoic chamber for high-fidelity measurements of hover performance.

The provided performance goals for this project were to have nominal thrust of 6.2 pounds and a peak of 9.3 pounds at hover. For forward flight at 44 knots the desired nominal thrust was 3.1 pounds with a peak thrust of 5.1 pounds. The goal for the noise signature was for the selected propeller design to be quieter than the current Aeronaut 16×8 three blade propeller, with minimal loss in efficiency. To test for these requirements two different locations were chosen to collect data. Performance data would be found at the Old Dominion University Wind Tunnel while the acoustic data would be collected at the NASA Langley Structural Acoustics Loads and Transmission (SALT) anechoic chamber. At each of these locations the same propeller test stand would be used with the same measuring devices, supporting hardware, and software.

The propeller test stand was also studied to validate the results produced and provide bounds on the accuracy. Validation of results is performed through comparisons to the published results of others and correlation to trends found in Xrotor, a rotor design code.

CHAPTER 2 - PROPELLER PERFORMANCE CHARACTERIZATION

2.1 AERODYNAMIC PERFORMANCE CHARACTERIZATION

Traditional characterization of propeller aerodynamic performance is through non-dimensional coefficients for comparison of the experimental results.[2] Eliminating the units scales all of the performance characteristics for simplicity of plotting and direct comparison. The main non-dimensional performance characteristics used are coefficient of thrust, torque, power and efficiency evaluated at a range of advance ratios. The definitions of these parameters follow.

Coefficient of Thrust $$C_T = \frac{T}{\rho n^2 D^4} \quad (1)$$

Coefficient of Torque $$C_Q = \frac{Q}{\rho n^2 D^5} \quad (2)$$

Coefficient of Power $$C_P = \frac{2\pi n Q}{\rho n^3 D^5} \quad (3)$$

Advance Ratio $$J = \frac{V}{nD} \quad (4)$$

Dynamic Efficiency $$\eta = J\frac{C_T}{C_P} \quad (5)$$

Static Efficiency (J=0) $$\eta = \frac{T^{\frac{3}{2}}}{2\pi n Q\sqrt{2\rho A}} \quad (6)$$

There are important considerations when performing direct comparisons with the shown coefficients. Propellers of similar design but different diameters will have nominally identical thrust coefficients, but these coefficients will be calculated at different thrusts measurements. With a fixed thrust target, the free variable within the coefficient formulas is the propeller RPM.

With this, propellers with a smaller diameter, or one with a lower thrust coefficient, will simply operate at a higher RPM.

Typical performance plots using these non-dimensional results can be seen in Figure 2 through Figure 4. These are results from experiments conducted by Selig using an APC 11×8 propeller.[3] These figures show a family of curves where each curve has a constant RPM and the velocity is varied. For performance data comparison, these plots simplify interpretation. For example efficiency combines thrust, torque, RPM, and velocity. When efficiency is plotted, as in Figure 2, it allows for quick comparison to other propellers. If an APC 11×6 propeller is plotted on the same plot it can be compared quickly to see if its efficiency is better or worse than the APC 11×8. This same comparison can be done for coefficient of thrust vs. advance ratio and coefficient of power vs. advance ratio. This is shown in Figure 3 and Figure 4, respectively.

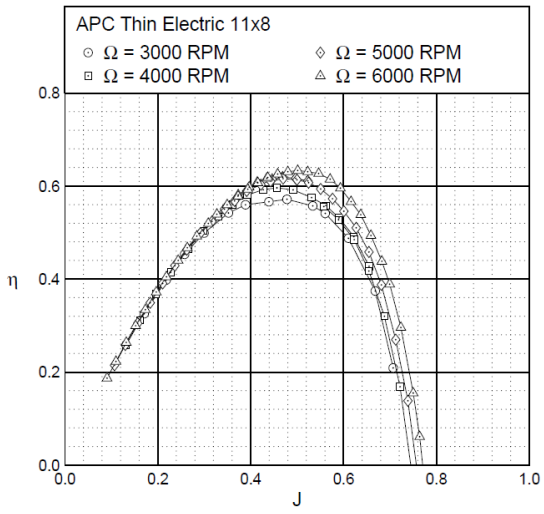

Figure 2- Typical efficiency vs. advance ratio plot of performance data [3]

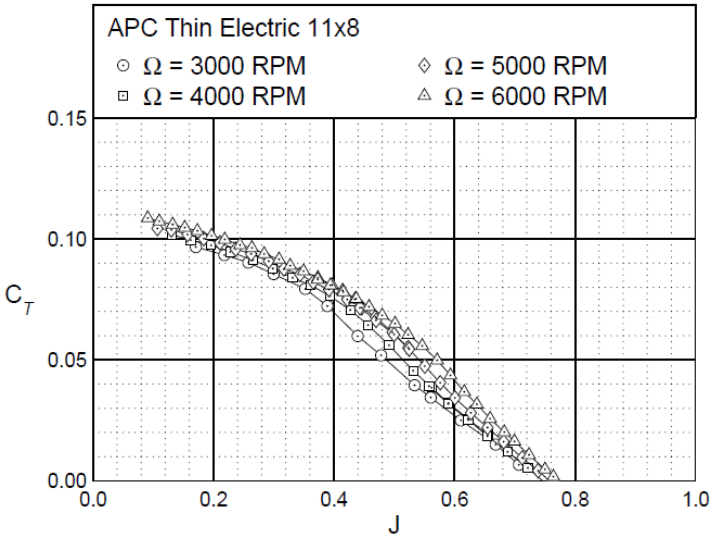

Figure 3- Typical coefficient of thrust vs. advance ratio plot [3]

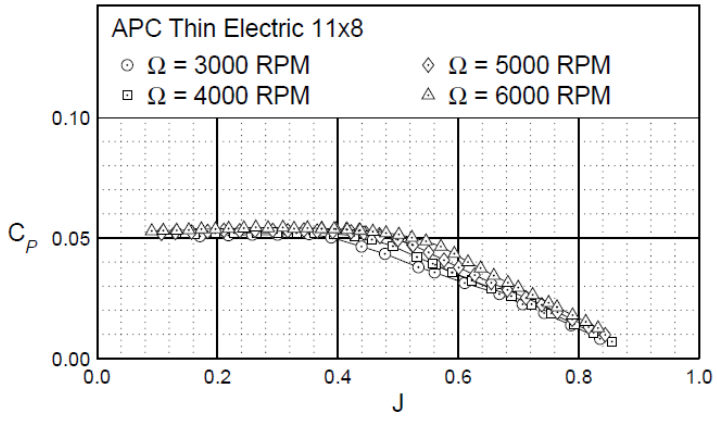

Figure 4- Typical coefficient of power vs. advance ratio [3]

2.2 REYNOLDS NUMBER EFFECTS

Reynolds numbers for model airplane propellers are low compared to full scale aircraft propellers because of their small chord size.[4] The range of blade chord Reynolds numbers for small propellers is approximately 30,000 to 300,000 for the rpm range typical of the GL-10. This range is derived from the wide range of flight conditions such from vertical takeoff through cruising in fixed wing flight.

In general, the Reynolds number affects performance by changing the produced lift and drag values. In general, higher Reynolds numbers are better as problems with laminar separation can be avoided.[3] Experiments performed by Selig found there was a trend in increasing efficiency with higher RPM. In Selig's experiment, different brands of model aircraft propellers showed the same trend; Increasing Reynolds number increased efficiency. The propellers Selig tested covered a range of brands and applications. Selig tested three different application types of four different brands. The application types are slow flyer, sport, and thin electric propellers. The four brands were APC, Graupner, GWS, and Master Airscrew. These are all plastic molded propellers of fixed pitch and hence can have defects such as seam lines along the leading edge of the propeller and at the tips. To ensure that the build quality of each manufacturer does not affect the results, Selig tested the as-built propellers, as if a user is unaware of defects. Figure 5 shows the results for an APC 11×8 propeller tested. It can be seen as the RPM is increased the efficiency increases. Since Reynolds number is dependent on velocity the same RPM to efficiency comparison can be made with Reynolds number. An increase in Reynolds will increase the efficiency.

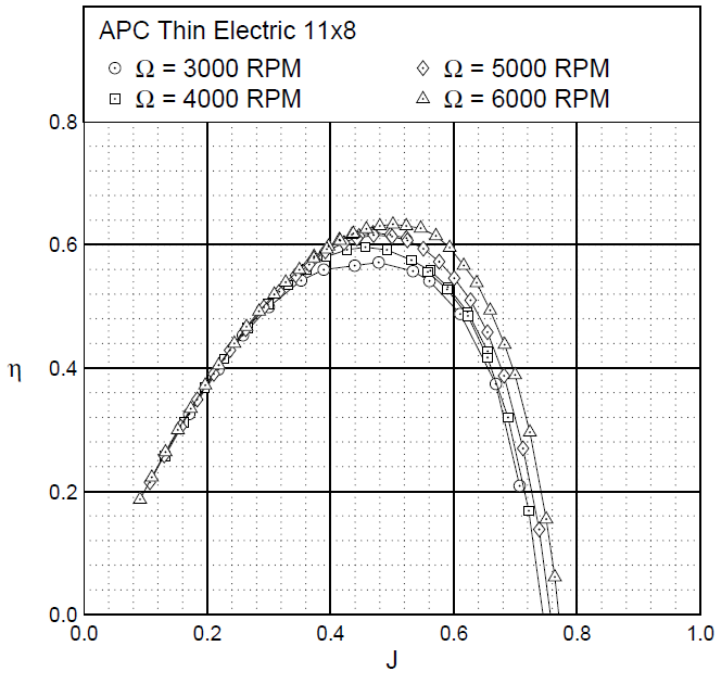

Figure 5- Increased efficiency with Reynolds number [3]

The results from this experiment concurred with work performed in the past on low Reynolds number airfoils as compiled in [5]. The results from this reference show the same trend. Figure 6 shows the results of a S7055 airfoil which is representative of the current GL-10 propeller profile. It can be seen as the Reynolds number increases, the coefficient of drag decreases and the maximum lift coefficient increases. The trends of these two coefficients increase the efficiency. In Equation (5) the coefficient of thrust in the numerator will be larger with a higher lift coefficient and the coefficient of power will decrease, serving to increase efficiency as well due to the decreasing coefficient of drag.

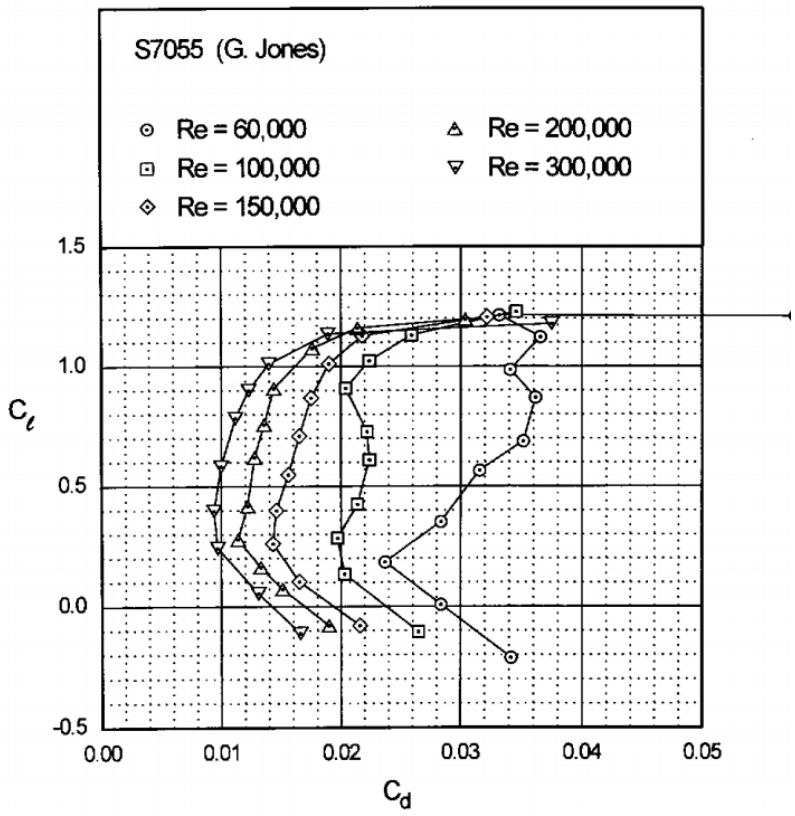

Figure 6- Low-Speed Airfoil Data shows increased performance with increased Reynolds number [5]

From reviewing these studies, it is apparent that Reynolds number will be a major factor in the selection of a high performance propeller for the GL-10. However this is working against the low acoustic signature knowledge in that the slower the propeller turns, the quieter it will tend to be.[6] The optimal propeller will be one with the best compromise.

2.3 ACOUSTIC CHARACTERIZATION

A microphone measurement of the change in pressure can be used to find the sound pressure level by first calculating the sound pressure.[7]

$$\bar{p}^2 = \frac{1}{t_c}\int_0^{t_c} \Delta p^2(x,t) \tag{7}$$

The term t_c is time duration of a noise cycle and Δp is the measurement from a microphone. These terms are used to find the mean square average for the sound pressure. The sound pressure can be converted to a sound pressure level(SPL) as shown in Equation (8).

$$SPL\ db = 10 \cdot \log_{10} \frac{\bar{p}^2}{p_{ref}^2} \tag{8}$$

The reference pressure is generally chosen to be $20\ x\ 10^{-6}\ Pa$.[8] This value is selected based on the lower threshold of the average human hearing. The result is that if the sound pressure is close to or has the same magnitude to the reference pressure then the SPL will be zero. If SPL is zero, this means there is nothing to be heard above the background sound level as perceived by the human ear.

For this project, the concern is how a propeller sounds to the human ear. This is dependent on the frequency of the noise. For this, an A-weighted sound pressure level is calculated shown in Equation (9).[7] The A-weighted SPL uses a filter on the sound pressure term to model the sensitivity of the human ear. The average human hears sound in a frequency range of 20Hz to 20kHz.[9] So the A-weighted filter tapers off the SPL on either side of this range. Without these corrections, frequencies below 20 Hz and above 20 KHz will increase the

SPL values. In order to determine the new A-weighted sound pressure level the filter is applied to the measured pressures from the microphone to provide an A-weighted mean square average for the sound pressure. With the A-weighted mean square average, $\bar{p}_A^2$, this can replace the unweighted mean square average in Equation (8).

$$SPLA\ dBA = 10 \cdot \log_{10} \frac{\bar{p}_A^2}{p_{ref}^2} \tag{9}$$

The reason for applying this A-weighted filter is that the area under the SPL curve can be integrated to provide an estimate of the sound reading in decibels. Without the filter the integrated value would be higher because the microphones can measure noise for a wider range of frequencies then the human ear can actually hear. Figure 7 shows the difference between the two curves. It can be seen there is significantly more area under the unweighted curve. For this project the A-weighted filter will be used for this reason.

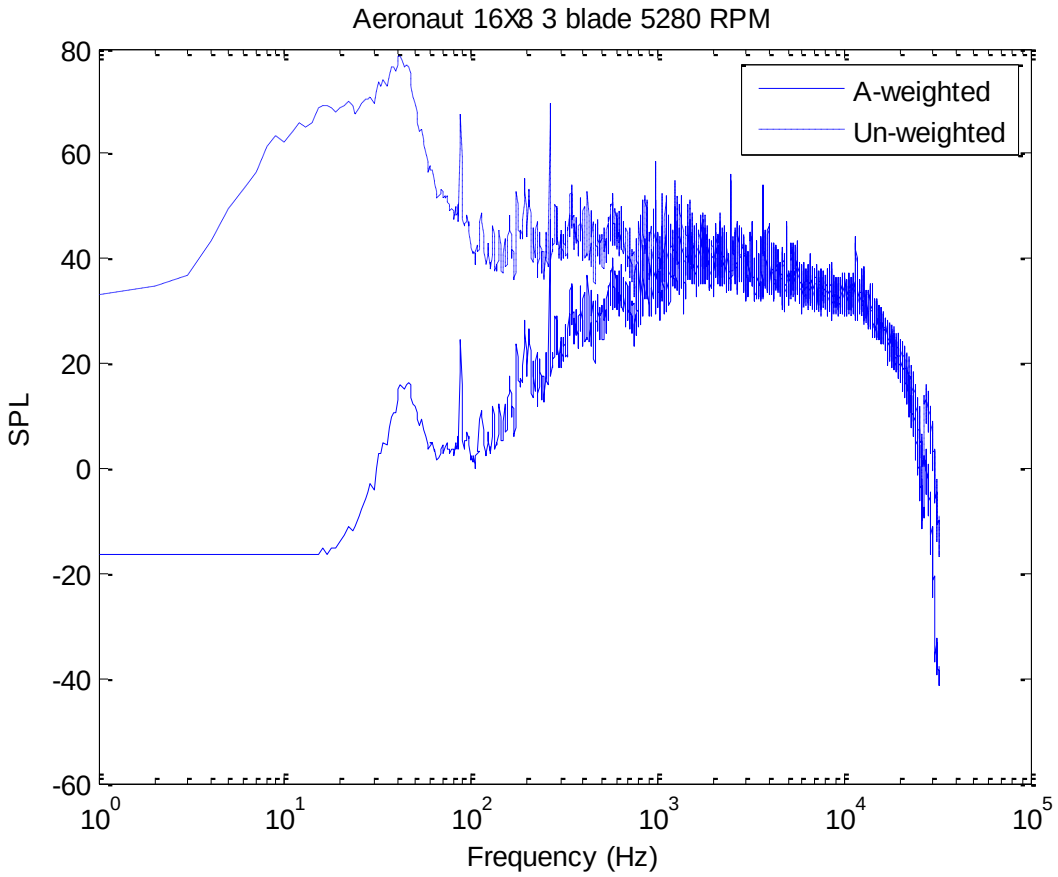

Figure 7-Comparison of Unweighted and A-weighted SPL vs. frequency plot

CHAPTER 3 - LITERATURE SEARCH

3.1 PROPELLER TEST STANDS

Performance test stands have been built for past experiments for testing small scale propellers in wind tunnels. Many of the designs involve a strut that aligns a motor with the longitudinal centerline of a wind tunnel test section. [10] The motor is typically fixed in place so it cannot be rotated to different angles, such as if it was on an aircraft that takes off vertically (or tilt wing) then transitions to forward flight. Researchers working with small propeller test stands chose a test stand design based on a rigid strut which was found to be the simplest and most reliable configuration. Rigid struts are able to minimize vibrations, while maintaining a simple design.[3]

Thomas's test stand used separate load cells to measure thrust and torque. [2] A beam load cell was used for the thrust axis and a cylindrical "can" load cell was mounted to the beam load cell to measure torque. From previous experiments at ODU using the same available model beam load cell, it was found that the propeller-motor combination caused excessive vibrations. For direct measurements with this model of load cell, the motor, and the motor mount are attached to the metric end. This means the load cell supports the weight of the motor and mount. When the propeller turns, this mass is excited causing excessive vibrations as it is essentially a spring-mass system with little or no damping. These vibrations lead to high uncertainty in the readings of both thrust and torque. The torque load cell used was a cylindrical single axis which appeared to be a good choice for this application. It is robust and can be mounted with a compact form factor. Since beam load cells have the majority of the material in the center cut out to allow for proper deflection of the strain gauges they can act as a spring.

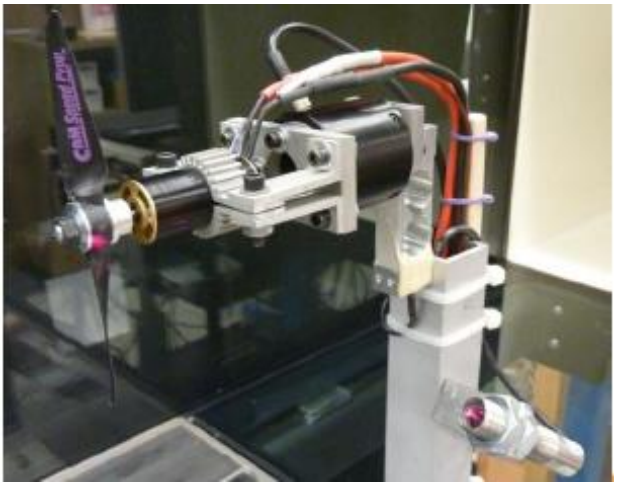

Figure 8- Thomas's propeller test stand [2]

In Selig's setup shown in Figure 9, linkages were used to separate and transfer the thrust and torque. There was a single strut that was suspended from the ceiling which all the loads passed through. This linkage was then connected to a perpendicular bar on top of the tunnel. It formed a "T" which provided mechanical advantage allowing adjustments to be made to the arm lengths to keep the load cell loaded at an optimal level. The load cells were located on the outside of the wind tunnel ceiling to minimize interference to the flow in the wind tunnel.

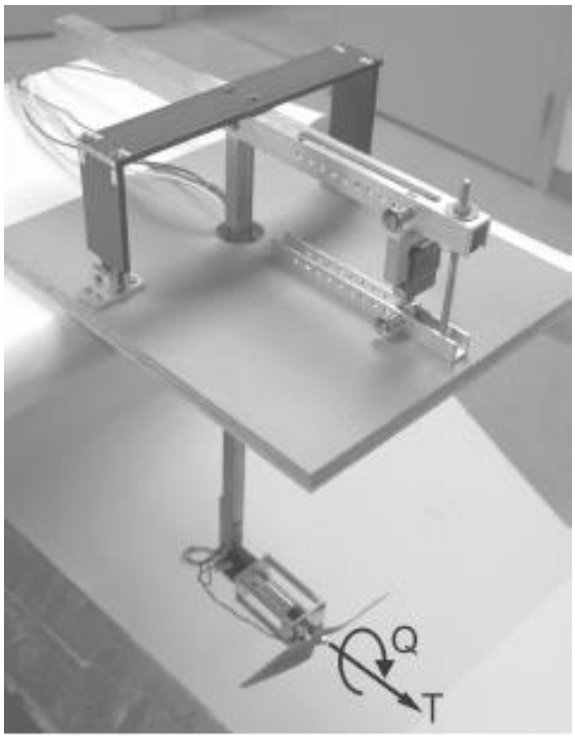

Figure 9- Selig's propeller test stand [3]

This design is optimum when looking at the uncertainty of load cell measurement of thrust. Common practice at NASA Langley is to attempt to load a load cell to 50% of full scale or more for best results. For example, if a load cell has a full scale loading of twenty pounds, the force applied should be at least ten pounds to get the best measurement. So if an experiment only has one load cell that has a high loading range, this can be a problem when used with propellers that produce small amounts of thrust. This is not the case with Selig's design; the linkages allow for adjusting the mechanical advantage to keep the forces within the optimal range of the load cell. The disadvantage to the design is that adjustment can be a time consuming process and this design requires special supports in the wind tunnel test section that penetrate the ceiling, hence is not portable.

Neither Thomas nor Selig made provisions for streamlining of the motor and hardware directly behind the propeller. In Figure 8, for instance, the exposed motor power wires, and the torque cell mounted to the thrust cell, will create drag that is seen in the thrust measurements as a reduction in thrust. The location directly behind the propeller exacerbates the problem as that region has a higher local velocity.

3.2 BOUNDARY CORRECTIONS

The propeller test stand experiments were to be performed in a wind tunnel in order to establish controlled conditions.[11] This is to minimize interference with outside disturbances such as wind and also lets the freestream flow speed be set to a specific velocity with confidence in the measurement. The consequence of putting the propeller test stand inside a wind tunnel is that this increases the wake velocity readings to values higher than they would be in free air.[12] Wall boundary corrections are required with the magnitude of corrections increasing as the propeller disk area approaches the test section area. A method developed by Glauert was found to be the most practical and is still popular today.[12, 13] His method is based on a control volume approach as shown in Figure 10. This approach looks at the inflow and outflow of the control volume to then derive a velocity correction. With the propeller mounted in the center of a wind tunnel, the propeller forms a disc area that has accelerated flow compared to the freestream. With the control volume enclosing this disc area from the floor to the ceiling of the wind tunnel, the area between the propeller blades and the walls of the wind tunnel can be found.

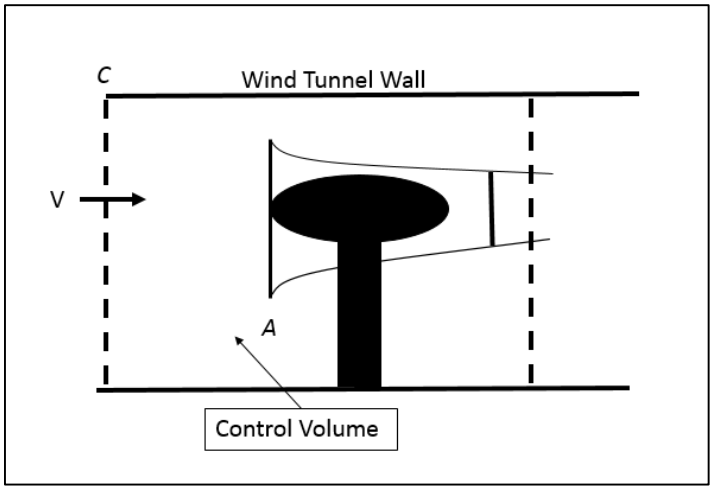

Figure 10- Control volume of propeller test stand in wind tunnel

Glauert defines a non-dimensional coefficient to include thrust and total linear momentum.

$$\tau = \frac{T}{\rho A V^2} \tag{10}$$

Using an additional simplification approach from reference [14], Equation (11) is determined.

$$\frac{V'}{V} = 1 - \frac{\tau\alpha}{2\sqrt{1+2\tau}} \tag{11}$$

$$\alpha = \frac{A}{C} \tag{12}$$

Starting from Equation (12) , where A is the propeller disc area while C is the cross sectional area of the wind tunnel. The calculation of τ from Equation (10), relates the thrust generated by the propeller to the linear momentum through the control volume. Lastly τ and α can be inserted into Equation (11) to get the corrected velocity, with V signifying the measured wind tunnel speed, and V' the corrected speed.

CHAPTER 4 - TEST STAND PRELIMINARY DESIGN

Previous experience with propeller test stands at ODU and literature research showed the test stand needed to be rigid and firmly mounted to avoid exciting resonant frequencies during testing.[15] In addition, the design had to be portable to facilitate testing in the wind tunnel and anechoic chamber which place the complex balance beam designs, such as Selig's test stand, at a disadvantage due to lack of portability.[3]

A surplus rigid strut was used for preliminary time history testing with an available six-axis gamma-sensor multi-axis load cell by ATI Industrial Automation. This was done to determine if there would be problems with vibrations. The preliminary strut was two feet long and had a symmetrical airfoil shape with a chord of three inches. A three-quarter inch thick, steel, ninety degree bracket was then bolted to the bottom of this strut for the motor and load cell attachment. This setup was supported by the ceiling of the wind tunnel test section. With this preliminary setup, a time history test was performed with an E-flight power 52 motor and an APC 13× 4 propeller. For each sample, data was collected for 45 seconds. Table 1 shows a typical run result with a mean and the standard deviation for thrust and torque. Since the standard deviation is small, the standard error about the mean is small.[16] Results showed that there is little interference from vibrations and a strut of similar design would be rigid enough for this project.

	Thrust (lbf)	*Torque (in-lbf)*
Mean	0.452	0.159
Standard Deviation	0.0013	0.000640

Table 1- Time history results for vibration test

Only two of the axes of the ATI Gamma-Sensor were used for data collection out of the six available. Thrust was measured through the Z axis and torque about the Z axis. There were initial concerns that the range of the load cell would be too large for expected loads despite the promising initial time history results. The load cell full scale value for thrust is one hundred pounds and the expected force is between one to twelve pounds of force. The expected torque is zero to ten inch pounds. If the forces are too small then this could increase the relative magnitude of the error in the readings resulting in a low signal-to-noise ratio. The load cell design was fixed by the limited budget so a detailed uncertainty analysis was conducted to quantify error.

In consideration of the measurement of the angular velocity of the propeller a first idea was to use an encoder. An encoder could simply be mounted to the back of a brushless motor that has an elongated shaft. A set screw would then attach the encoder to the shaft of the motor. This would make it simple to change to different brands and sizes of motors. However, an encoder is designed for precisely tracking the location of a moving shaft. A few examples are robotic arms, aircraft servos, and CNC machine drive mechanisms. Because of this precision requirement, there is an associated additional cost versus a simple counter sensor. This project only needed a way to read the angular rate at relatively high RPM, so the encoder was over qualified for the task. Due to the expense of encoders, other methods to capture RPM were studied.

A laser diode and detector was considered. The light beam would be directed across the arc of the propeller. Every time the propeller would interrupt the path of the collimated beam, it would be reflected back to a collector that was located adjacent to the laser diode. When the collector "sees" the reflected light, a pulse is generated and can be counted to give the number of revolutions per minute. The only calculation to be done was to divide by the number of blades to

yield revolutions per minute. Using this method of finding RPM made it simple to change motors since there would be nothing actually connected to the motor. The laser beam and collector sensor would be attached to the propeller test stand permanently. However, through the preliminary experimentation it was found that this method only worked well once the laser was pointed in exactly the right spot so the reflector could pick up the reflected light. The laser beam needed to be mounted so it was perpendicular to the face of the propeller blade. This made it infeasible because then the laser beam and collector sensor would have to be mounted at a distance from the test stand, adding to interference with the propeller blade in the wind tunnel. Even with the laser beam perpendicular to the face of the propeller blade at RPM's greater than 3,000 the reflected light sensor would stop producing pulses. These inconsistent results led to a third method to be studied using proximity sensors.

A proximity sensor produces a pulse when a metallic object comes close to the sensor. Just like the laser beam and collector sensor, the pulses can be counted using a counter board to get the RPM. For this test, an inductive proximity sensor was mounted on the test stand so that it could sense the head of a screw. Two screws spaced one hundred eighty degrees from each other were threaded into a collar. The collar was mounted to the shaft of the motor using set screws. Two screws were chosen to keep the balance of the rotating shaft and prevent vibrations. To get the true RPM, the counted pulses would be divided by two since there were two screws, hence two pulses per revolution. This method was found to be reliable and even a time conservative method if different brands of motors were to be used. The setup is shown in Figure 11.

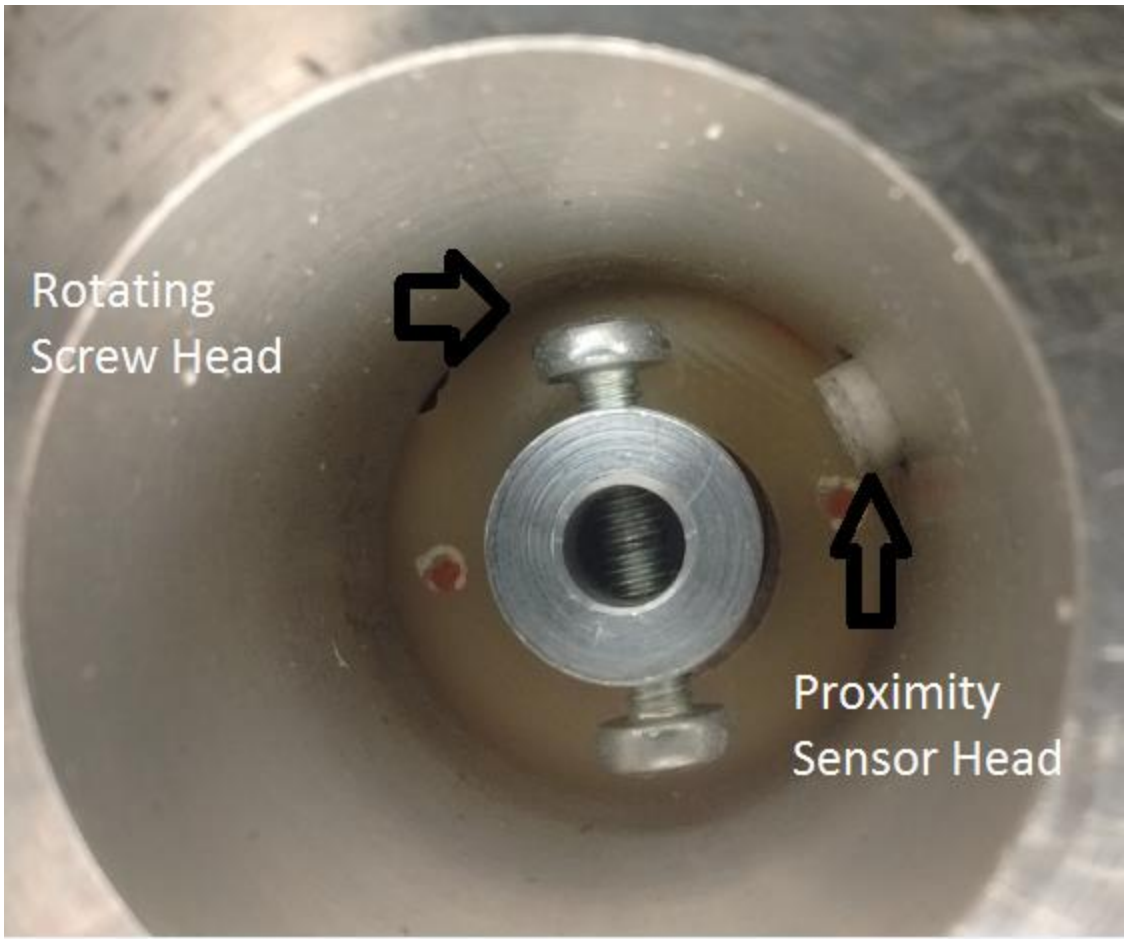

Figure 11- Proximity Sensor installation

The tunnel conditions collected are temperature, barometric pressure and dynamic pressure. Temperature was collected using an Omega TJ-USB thermocouple probe that is placed in the freestream just after the test section. The temperature signal is then read through a serial port into the computer and recorded using LabVIEW software. Barometric pressure is measured using a Mensor 2500 barometer which sends a signal via a serial port on the computer. Dynamic pressure is used when calculating velocity of the wind tunnel. Dynamic pressure was collected by a Mensor 6100 digital pressure transducer that measures the difference between static

pressure before and after the contraction just upstream of the test section. This signal is also read into the computer running LabVIEW via serial ports.

Supplied motor voltage and current are also factors considered for this experiment. This experiment used a Sorensen DCS55-55E power supply rated for 55 volts with a capacity of 55 amps. The necessary voltage for this experiment was 29 volts with a maximum current of 40 amps to prevent damage to the motor. This operating voltage was chosen as it is the nominal operating voltage of the GL-10 which uses a Lithium-Polymer 7-cell battery. 40 amps was a limit set by the motor manufacturer. Due to the voltage and current being high, it introduced some problems when using a National Instruments DAQ board rated for 0-10 volts analog input.

The voltage from the power supply to be read was 29 volts and had to be reduced to an adequate range to not damage the analog ports. To do this, a voltage divider was built to divide the voltage from 29 volts to 8.33 volts with a scale factor of 3.5. To prevent electrical losses wherever possible, wires were kept as short as possible between the power supply and the analog port input board.

The current flowing into the system was measured using a CR Magnetics CR5211-100 inductance ring. The inductance ring works with a Hall effect sensor and a magnetic ring. As the current flows through the magnetic ring a magnetic field is produced. As the current changes, or the magnetic field changes due to the current, the Hall effect sensor outputs a voltage in response to the changing magnetic field. The voltage output from the Hall effect sensor can then be read using the National Instruments analog voltage data acquisition board. For this particular current transducer, the ratio was one volt output for every ten amps. The max output voltage was ten volts. This allowed for the use of the full scale of the current transducer which was zero to 100

amps. As stated before, the current limit was 40 amps for this project so the 100 amp limit exceeded this greatly. Hence, there would be no issues with the voltage being too high for the analog input ports. For the installation of this sensor, the positive side supply wire of the system was passed through the current transducer. To avoid interference from the negative side of the system the inductance ring was placed securely away from the negative terminal.

Traditional control of small brushless motors such as the one used in this project is done with the use of an electronic speed control connected to a hobby grade radio control receiver. A user sends commands from a transmitter to a receiver, which in turn sends a pulse width modulated signal to the electronic speed controller which controls the speed of the motor. The problem with using a transmitter and a receiver is the throttle command cannot be repeatedly set to the same throttle position or to another position with great accuracy. This project required the ability to set the throttle at any location and have the ability to replicate this location. The solution was to use a USB to servo control board. The Pololu twelve-channel Mini Maestro replaces the transmitter and the receiver. The electronic speed controller plugs into the Mini Maestro instead of a receiver. The Mini Maestro then connects to the computer through a USB cable. A LabVIEW code is then used so the user can enter a precise desired throttle position.

It was desirable to streamline the test stand for minimum interference and for acoustic measurements there was a need to smoothly transition the flow. To do this, a tear drop shape nacelle was used to enclose the motor, load cell, and any other hardware that would otherwise be exposed to the prop slipstream. Since the experiment was based around acoustic measurement, the need to eliminate noise generators in the form of sharp corners was necessary.[17] The nacelle also makes the flow behave in a way that can be modeled in prediction programs such as Xrotor.[18] It is simpler and more accurate to model a single teardrop shape compared to not

having a nacelle at all. With no nacelle, there are wires going to the motor, load cell and to the tachometer sensor. These would all have to be modeled separately along with the complex contour of the propeller test stand structure just to get the interactions with the propeller. Even if this was done correctly, the flow would be complicated turbulent flow which reduces the accuracy of the model. So the teardrop shape would be best because it could be modeled accurately using potential flows. With the addition of the streamlined nacelle, cooling becomes a problem.

Due to the long duration of the test runs, keeping the motor and ESC at an appropriate temperature is important. Cooling will prolong the life of the motor and prevent the speed controller from overheating and going into an overheat protection mode, where all power to the motor is cut off. To avoid this problem, it was found that mounting the ESC outside the wind tunnel where a fan can then blow room temperature air over it kept it at an acceptable temperature. The motor had to stay within the nacelle. So the use of compressed air was introduced. The compressed air was set up to blow around the rear of the motor to remove as much heat through convection as seen in Figure 12. This warm air would then flow towards the rear of the nacelle where there is an exit hole for it to escape.

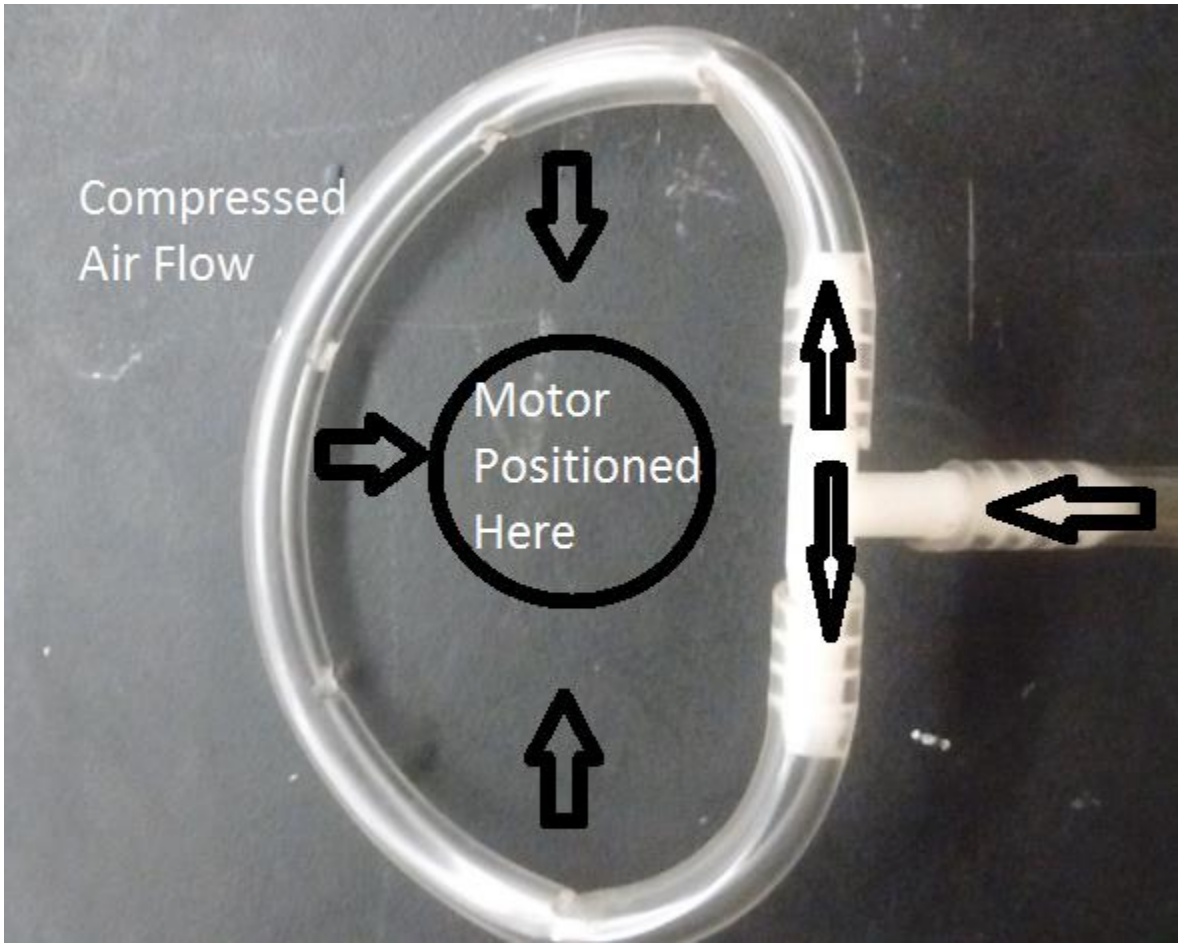

Figure 12- Compressed air ring for motor cooling

Acoustic measurements were to be made in the ODU Wind Tunnel as well as the NASA LaRC anechoic camber. Wind tunnel measurements were made using the Bruel and Kjaer hardware and software. A Bruel and Kjaer type 4190-L-001 microphone was mounted at the lateral center of the wind tunnel behind the propeller at 45 degrees from the plane of the propeller. An array of microphones could be implemented, but for simplicity, the 45 degree location was the only one used[19] This can be seen in Figure 13. Measurements from the

microphone were then sampled by a Bruel and Kjaer type 7536 data acquisition system that used Pulse software to record the data.

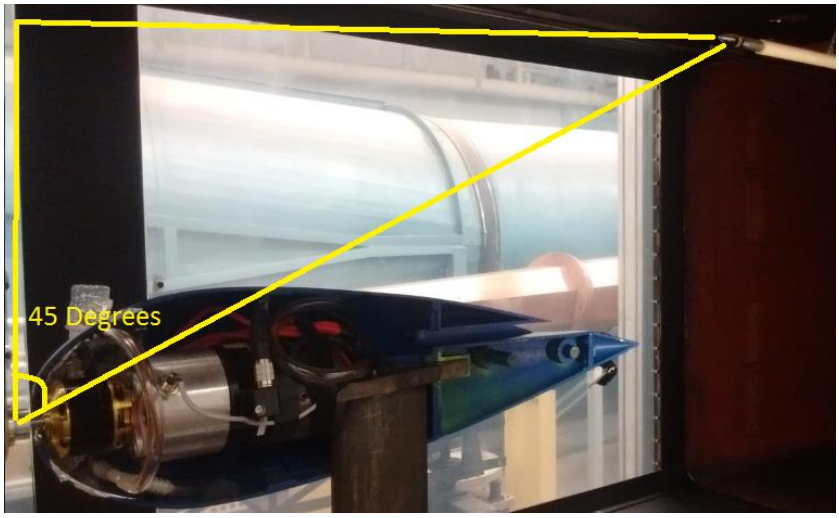

Figure 13- Microphone set up in the wind tunnel

CHAPTER 5 -TEST STAND FINAL DEVELOPED DESIGN

The experience with the preliminary propeller test stand allowed for the selection of the best parts to use for the final design and experiments. Uncertainty studies showed that the existing ATI Gamma-Sensor would provide meaningful measurements for comparison of propeller designs.

Power input calculations were performed using the in-house built precision voltage divider that allowed the power supply voltage to be recorded. For current flow measurement, the commercial current transducer was found to work well. With these two devices, outputs were then multiplied together to get input power in watts. The power readings were useful in troubleshooting if non-realistic thrust values arose. They also acted as a safety monitor in avoiding over-current situations.

The tachometer sensor was the last sensor to be chosen for the final test stand set up. The laser with the reflected light sensor was found to be too cumbersome to set up and reliability was an issue. The proximity sensor was used instead. It was found while implementing this sensor that the freedom to use other brands of brushless motors was still possible with minor modifications.

Motor control signals were sent using a LabVIEW code through a serial port to the Mini-Maestro motor control board. A Castle Creations™ Phoenix Edge Lite100 amp speed controller was then plugged into one of the ports on the Mini Maestro. The Mini Maestro allows for accurate replication of RPM settings. A value used by the Mini Maestro which sets the RPM of the motor can be recorded for future testing. This completely eliminated the use of hobby transmitters and receivers to control the speed of the motor.

The power supply used for the test stand motor was a Sorensen DCS55-55E. This is a switching power supply that converts AC 220 volts input to max DC of 55 volts output. The user can then select the desired output voltage and max current settings. This project required 29 volts DC with an available capacity of 40 amps.

The nacelle was manufactured at ODU using a 3D printer. Due to the length of the nacelle it was printed in six sections. Three sections per side were then glued together to make half of the nacelle. With the nacelle in two halves, there is easy access to all of the components inside. Figure 14 shows a cutaway of the propeller test stand. Half the nacelle can be seen as well as the other components for the final developed design. Figure 15 shows the completed propeller test stand installed in the ODU Wind Tunnel.

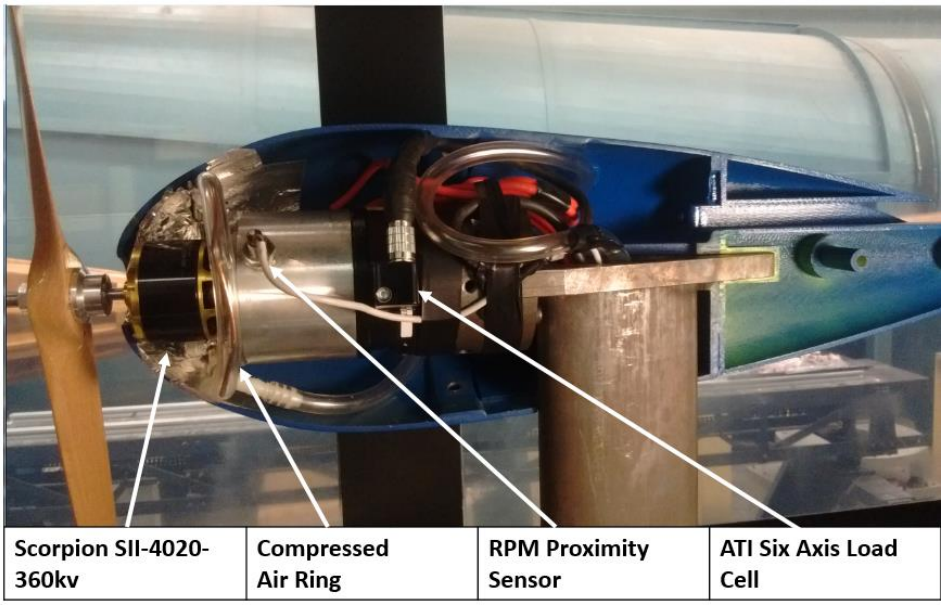

Figure 14- Cutaway of propeller test stand

Figure 15- Propeller test stand mounted in wind tunnel with Georgia Tech propeller installed

Figure 16 shows the complete layout of all the described parts used in the propeller test stand.

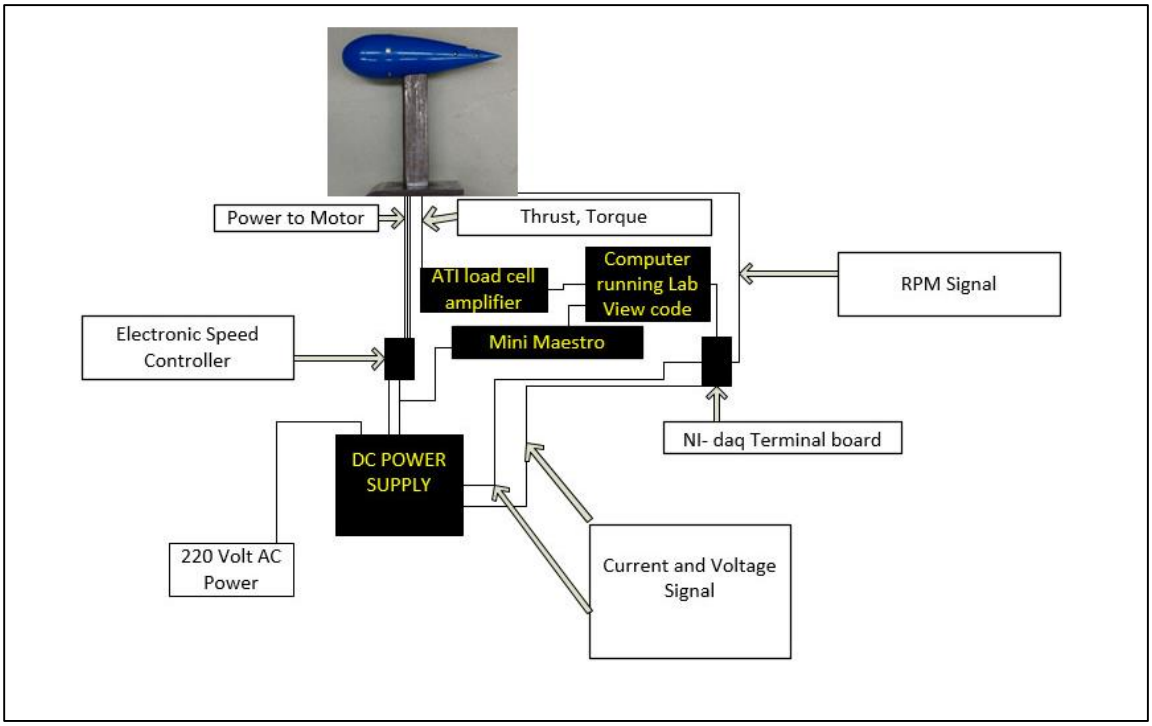

Figure 16- Layout of testing equipment

The wind tunnel used at ODU for the performance and acoustic testing is a closed return design. Figure 17 shows the location of the propeller test stand in the high speed test section. At this location in the wind tunnel, freestream velocities are available up to 50 meters per second. This is well over the maximum velocity required for the GL-10 testing. Wind tunnel fan speed can be set precisely using a variable frequency drive. A LabVIEW program is used to provide closed-loop control of tunnel velocity or dynamic pressure.

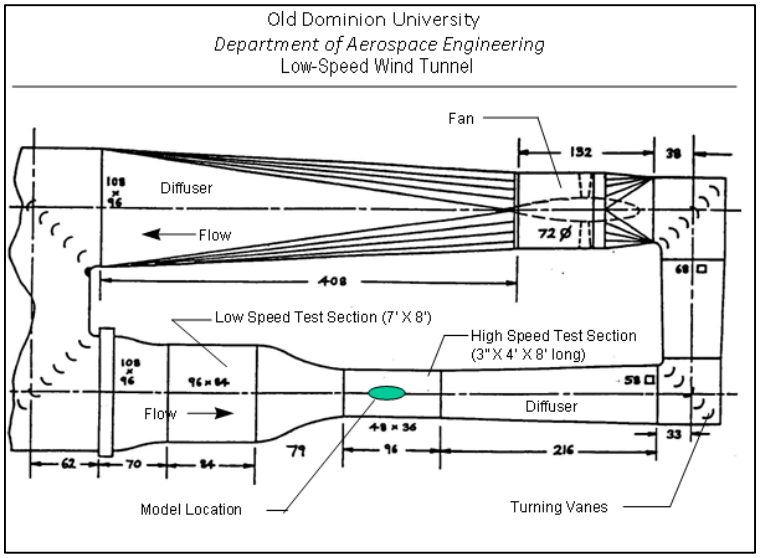

Figure 17- Layout of ODU wind tunnel (dimensions in inches and feet)

Tests were also performed at the NASA Langley Structural Acoustic Loads and Transmission (SALT) facility. At this facility, there are two rooms connected together, a reverberant source room and an anechoic receiving room. For this project, only the anechoic room was used and the connection between the rooms was covered with foam wedges. The anechoic receiving room has a volume of 11,900 ft^3 and is enclosed by acoustic wedges. Figure 18 shows an overview of what the room looks like with the propeller test stand mounted. The microphones used can also be seen in Figure 18 and are located at 0, 22.5, and 45 degrees from the plane of the propeller.

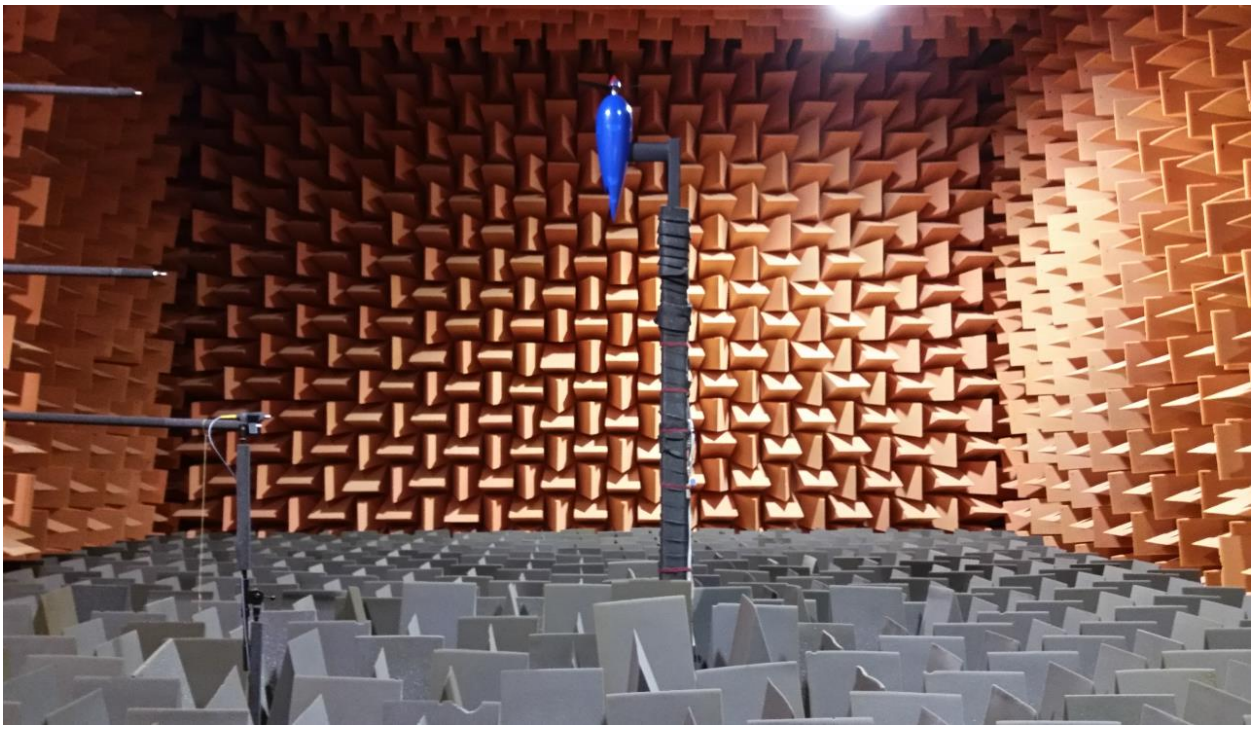

Figure 18- Overview of NASA Langley anechoic chamber

Testing in the anechoic chamber required one change to the structure of the test stand. The test stand was mounted in the vertical position on top of a tower. Figure 19 shows the replacement structure, where the components shown in Figure 14 can be quickly moved. Figure 20 shows the complete setup in the anechoic chamber.

Figure 19- Anechoic chamber propeller test stand mount

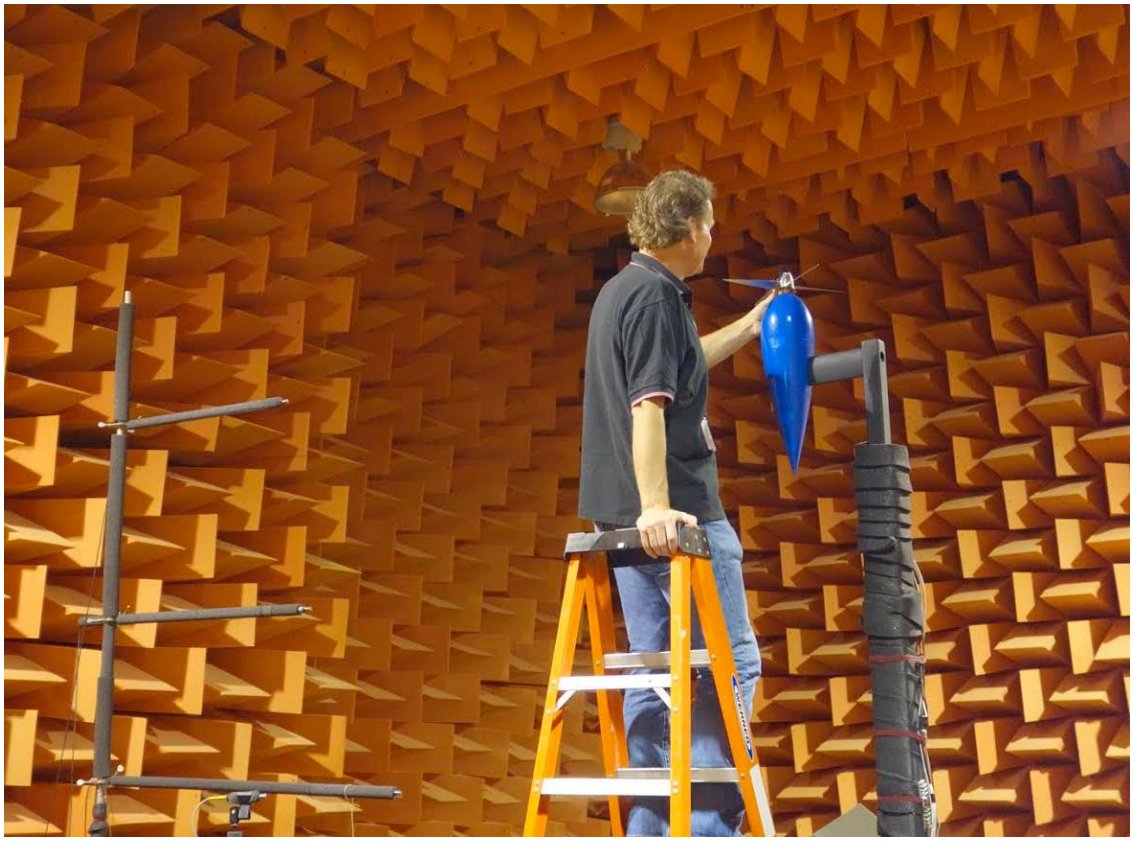

Figure 20- Propeller test stand in anechoic camber

5.1 LabVIEW SOFTWARE

LabVIEW is a visual programming language that utilizes a graphical user interface (front panel) and graphics based visual programming in the form of a block diagram (rear panel). The front panel shows in real time the measurements of thrust, torque, input voltage, input current, and RPM. Figure 21 shows the front panel for the propeller test stand. Tunnel speed control can be set manually or using the closed loop controls. Real time visual aids are employed, such as the plots showing the real time dynamic pressure and the RPM of the motor. This allows the user to verify that the wind tunnel and RPM are steady before allowing data collection to start. The front panel also allows the user to input the propeller diameter, data file name to be saved, and the RPM of the motor.

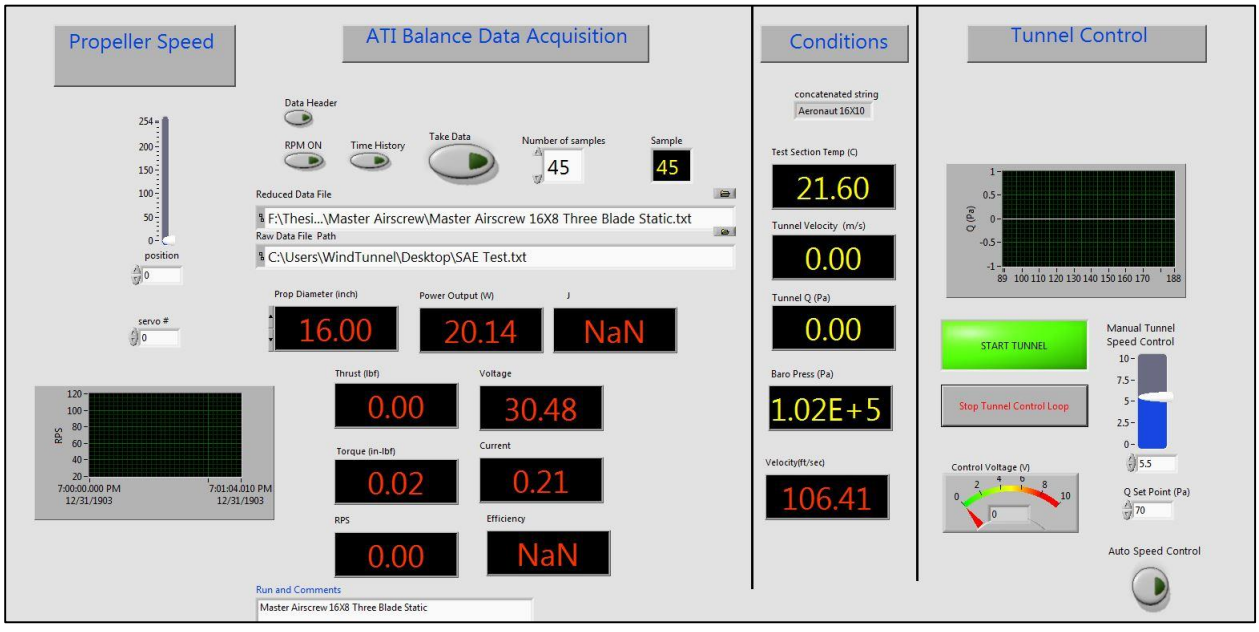

Figure 21- LabVIEW front panel

The rear panel contains the block diagram style coding. APPENDIX A shows the loads from the load cell being split apart and put into six different arrays. These arrays are sent to the front panel. If the “take data” button on the front panel is selected the data are also recorded to the text file selected by the user. Appendix A.1 shows the processing of the signal from the RPM, voltage, and current sensor. Here is where any corrections that need to be performed are completed. For example, the RPM count needs to be divided by two because two screw heads were counted for every revolution. The thermocouple and pressure transducer were read in a similar manner. Having all of the signals in LabVIEW allows for calculations of coefficients. Appendix A.2 shows the calculation of the coefficients described earlier. These coefficients require values such as density, propeller diameter, and loads from the load cell. LabVIEW allows formula nodes to be written so this necessary information can be mapped to the formula node while the output can go to the front panel or be recorded to a file.

5.2 IMPLEMENTATION

A user selects a propeller to test and installs it on the motor shaft of the propeller test stand. In LabVIEW, the name of the file where data are to be saved is entered by the user. The propeller diameter is also entered to be used in the calculations. The power supply for the motor is then turned on after the propeller test stand is free of obstructions and it is safe to do so. With LabVIEW running the user is able to control the motor with the RPM slider on the front panel. Before any tests in the wind tunnel are performed, the compressed air is turned on for motor cooling. Also, a tare load is subtracted from the ATI load cell to remove any residual measurements after each run.

For static testing the wind tunnel is left in the off position. A series of RPM values are then tested for each propeller. The RPM values are set manually by the user. For each value of

RPM the take data button is selected once the RPM is steady and data are collected for 45 seconds in the wind tunnel. Static testing in the anechoic chamber was performed in a similar manner. To measure only the noise from the propeller test stand, compressed air was turned on only after acoustic measurements were made. Data were only collected for ten seconds to prevent overheating of the motor, since the compressed air was not on. Ten seconds was also the longest period of time before backwash from the propeller would affect the microphones measurements. For dynamic testing the control of the motor and the data file naming is the same except the tunnel is running. The user can adjust the tunnel velocity to a specific velocity or adjust the velocity to achieve a desired advance ratio.

CHAPTER 6 - EXPERIMENTAL METHODS

Due to the number of propellers to be tested, an efficient way to change factors and collect data was necessary. The possible factors to change in tests included RPM, test section velocity, propeller diameter and propeller pitch. The motor and power requirements could have also have been factors; however this work is focused on using the current motor and power system being used on the GL-10.

The simplest and most widely used way to conduct experiments is by changing one factor at a time while keeping all other factors constant, often called the scientific method. Using this method would require, for instance, the experimenters to have a set of propellers that are incrementing in pitch for a constant diameter. This is not a logical approach.

For this project the current propeller blade dimensions were the focus. The project scope stated that the diameter of 16 inches should be kept the same to avoid contact with other propellers. RPM, wind tunnel velocity, and propeller blade pitch, and blade section design, are then the remaining factors. For a given blade section design, the remaining factors can then be further reduced into just two factors by using the non-dimensional coefficient called advance ratio described earlier in the paper. This allows the experimenter to select a range of advance ratios and propeller pitches. This greatly simplifies the experiment in that the wind tunnel does not have to be opened after each test. Only when the experimenter wants to change the pitch of the propeller blade does the wind tunnel test section have to be accessed.

With this information, the only factors to change during test were the propeller pitch, RPM, and wind tunnel velocity. Dynamic tests were performed by setting the RPM of the propeller to a set value then varying the velocity of the Wind Tunnel Five, or as many possible, advance ratios were run for each propeller tested. Some propellers stopped producing thrust

before the higher advance ratios were met. The range of advance ratio was then varied at other fixed RPM values. The advance ratios were based around the expected flight velocities provided for the project. For static data collection, only propeller pitch and RPM were factors. A range of RPM's were run for all propellers tested statically. The range of RPMs was selected based on the thrust requirement of the project. This was done in the ODU Wind Tunnel as well as in the anechoic chamber.

To insure maximum possible thrust and torque over the flight envelope, propeller blades with pitches of six and greater were selected. Also the RPM range was selected to include a point that is as high as possible for the drive motor. To ensure these constraints are feasible, validation was performed using the Aeronaut 16×8 3-blade propeller. Also the APC 15×8 was tested. Both of these propeller tests were replicated and compared to numerical models. Validation with these propellers allowed for testing of the propellers listed in Table 2.

Propellers Tested	
Aeronaut 16×6 3-Blade	Aeronaut 16×10 2-Blade
Aeronaut 16×8 3-Blade	Vess 16×6 2-Blade
Aeronaut 16×10 3-Blade	Vess 16×8 2-Blade
Aeronaut 16×6 2-Blade	Master Airscrew 16×8 3-Blade
Aeronaut 16×8 2-Blade	Georgia Tech 4-Blade
	APC 15×8

Table 2- List of propellers tested

6.1 UNCERTAINTY ANALYSIS

Using the developed test stand design there was a need to understand how much uncertainty was associated with the performance parameters C_T, C_Q,C_P and η. As stated before in the test stand design, the selected load cell was rated for forces and moments that were much greater than those produced by the propellers that were tested. An uncertainty calculation is necessary to quantify the expected error. One way to perform the uncertainty test is to use the Taylor Series Method(TSM) for Propagation of Uncertainty's.[20] This method is built on two components of uncertainty, systematic error and random error. Systematic error comes from error sources that do not vary between runs. This error is a measure of the difference between the true value and the mean of N measured values as shown in Figure 22.

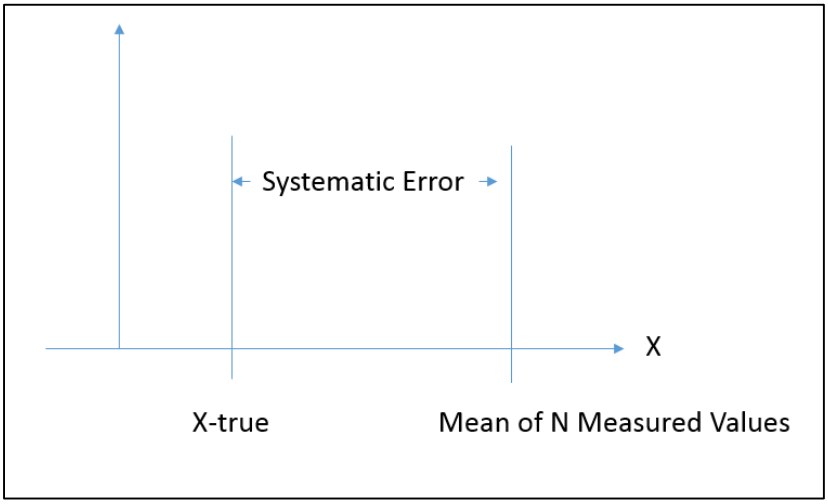

Figure 22- Systematic error

The random error comes from sources that vary during a measurement period. For example, computing velocity requires measurement of barometric pressure, temperature, and

dynamic pressure in the test section. Each of the involved instruments will have an associated random error meaning the instruments will provide a slightly different reading for each sample, even under constant conditions. The random error is captured in the standard deviation calculation of the N samples measured. Since the standard deviation is divided by the square root of N samples to yield the standard error, data sets are replicated to reduce the standard error, by increasing the sample size. Keeping the standard error small will keep the random component of uncertainty as low as possible. Figure 23 shows the random error in addition to the systematic error. The random error is combined with the systematic error and scaled by a t-statistic (often called a coverage factor) to obtain a two-sided confidence interval. Many standards choose two as a coverage factor which serves as an approximate t-statistic for samples with at least 10 observations.[16]

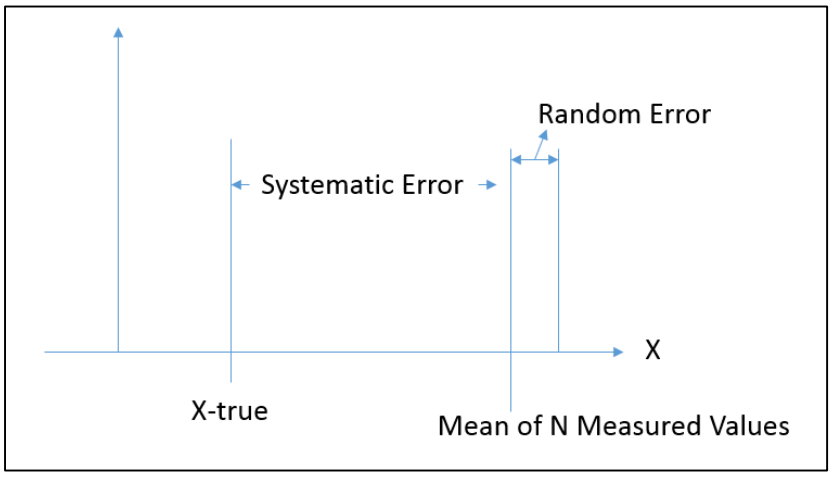

Figure 23- Systematic error and random error

The complete build-up of the TSM model starts with a data reduction equation r. An example of this given in reference [20], where r is a function of two variables x and y.

Data reduction equation $r=f(x, y)$ (13)

This function is used to determine the systematic error for the TSM uncertainty calculation. The systematic error is computed by taking the partial derivative of each variable which has an error source in the data reduction equation, then multiplying by the systematic error of the variable that is in the denominator of the partial derivative. This is shown in Equation (14) using equation (13).

$$\text{Systematic error} = \frac{\partial r}{\partial x}^2 \ b_x^2 + \frac{\partial r}{\partial y}^2 \ b_y^2 \tag{14}$$

where b_x, b_y are the systematic standard uncertainties for measured quantities x and y. This process can be applied to the coefficients used for characterizing, propeller performance, C_T, C_P, C_Q, J and η.

The systematic error of each term is derived first:

Data Reduction Equation C_T

$$C_T = \frac{T}{\rho n^2 D^4} \tag{15}$$

$$\frac{\partial C_T}{\partial T} = \frac{1}{\rho n^2 D^4} \tag{16}$$

$$\frac{\partial C_T}{\partial n} = -\frac{2T}{\rho n^3 D^4} \tag{17}$$

$$\frac{\partial C_T}{\partial \rho} = -\frac{T}{\rho^2 n^2 D^4} \tag{18}$$

$$\frac{\partial C_T}{\partial D} = -\frac{4T}{\rho n^3 D^5} \tag{19}$$

$$U^2_{C_T\,Systematic} = \frac{\partial C_T}{\partial T}^2 U_T^2 + \frac{\partial C_T}{\partial \rho}^2 U_\rho^2 + \frac{\partial C_T}{\partial n}^2 U_n^2 + \frac{\partial C_T}{\partial D}^2 U_D^2 \tag{20}$$

Data Reduction Equation C_Q

$$C_Q = \frac{Q}{\rho n^2 D^5} \tag{21}$$

$$\frac{\partial C_Q}{\partial Q} = \frac{1}{\rho n^2 D^5} \tag{22}$$

$$\frac{\partial C_Q}{\partial n} = -\frac{2Q}{\rho n^3 D^5} \tag{23}$$

$$\frac{\partial C_Q}{\partial \rho} = -\frac{Q}{\rho^2 n^2 D^5} \tag{24}$$

$$\frac{\partial C_Q}{\partial D} = -\frac{5Q}{\rho n^2 D^6} \tag{25}$$

$$U^2_{C_Q\,Systematic} = \frac{\partial C_Q}{\partial Q}^2 U_Q^2 + \frac{\partial C_Q}{\partial \rho}^2 U_\rho^2 + \frac{\partial C_Q}{\partial n}^2 U_n^2 + \frac{\partial C_Q}{\partial D}^2 U_D^2 \tag{26}$$

Data Reduction equation C_P

$$C_P = \frac{2\pi Q}{\rho n^2 D^5} \tag{27}$$

$$\frac{\partial C_P}{\partial Q} = \frac{2\pi}{\rho n^2 D^5} \tag{28}$$

$$\frac{\partial C_P}{\partial n} = -\frac{4\pi Q}{\rho n^3 D^5} \tag{29}$$

$$\frac{\partial C_P}{\partial \rho} = -\frac{-2\pi Q}{\rho^2 n^2 D^5} \tag{30}$$

$$\frac{\partial C_P}{\partial D} = -\frac{10\pi Q}{\rho n^2 D^6} \tag{31}$$

$$U^2_{C_P\,Systematic} = \frac{\partial C_P}{\partial Q}^2 U_Q^2 + \frac{\partial C_P}{\partial \rho}^2 U_\rho^2 + \frac{\partial C_P}{\partial n}^2 U_n^2 + \frac{\partial C_P}{\partial D}^2 U_D^2 \tag{32}$$

For systematic uncertainty of efficiency the systematic uncertainty of advance ratio is derived first since it is used in this calculation.

Data reduction equation J

$$J = \frac{V}{nD} \tag{33}$$

$$\frac{\partial J}{\partial V} = \frac{1}{nD} \tag{34}$$

$$\frac{\partial J}{\partial n} = -\frac{V}{n^2 D} \tag{35}$$

$$\frac{\partial J}{\partial D} = -\frac{V}{nD^2} \tag{36}$$

$$U^2_{J\,Systematic} = \frac{\partial J}{\partial V}^2 U_V^2 + \frac{\partial J}{\partial n}^2 U_n^2 + \frac{\partial J}{\partial D}^2 U_D^2 \tag{37}$$

Data reduction equation η

$$\eta = J\frac{C_T}{C_P} \tag{38}$$

$$\frac{\partial \eta}{\partial J} = \frac{C_T}{C_P} \tag{39}$$

$$\frac{\partial \eta}{\partial C_T} = \frac{J}{C_P} \tag{40}$$

$$\frac{\partial \eta}{\partial C_P} = -\frac{JC_T}{C_P^2} \tag{41}$$

$$U^2_{\eta\, Systematic} = \frac{\partial \eta}{\partial J}^2 U_J^2 + \frac{\partial \eta}{\partial C_T}^2 U^2_{C_T} + \frac{\partial \eta}{\partial C_P}^2 U^2_{C_P} \tag{42}$$

With all systematic uncertainties for each coefficient derived the random error is the remaining unknown. The random error in a measured quantity is best estimated by calculating the standard deviation of repeated samples.

$$\text{Random error } = \sqrt{\frac{1}{N-1}\sum_{i=1}^{N}(X_i - \bar{X})^2} \tag{43}$$

The addition of the systematic error and the random error provides the total amount of error in the experiment. Equation (44) is a general equation for the total of the systematic and random error where "r" represents any coefficient in this case.

$$U_r^2 = \frac{\partial r}{\partial x}^2 b_x^2 + \frac{\partial r}{\partial y}^2 b_y^2 + \sqrt{\frac{1}{N-1}\sum_{i=1}^{N}(X_r - \bar{X})^2} \tag{44}$$

CHAPTER 7 - RESULTS

7.1 UNCERTAINTY

Uncertainty estimates for coefficients computed from propeller test stand measurements were first calculated using the method previously described. This was done before validation or data were collected for comparison. It was important to establish error bounds in the results to make sure the developed design provided enough accuracy. The systematic error was calculated using the manufacturer's confidence intervals provided. For example, the ATI load cell provides an uncertainty reading for the thrust direction of 1/160th of a pound. Systematic uncertainties for density were found by using the ideal gas law with the measured quantities of temperature and barometric pressure. The systematic uncertainty can then be computed by combining the individual source values provided from the manufacturer of the thermocouple and the pressure transducer. Using these parameters collected, the partial derivatives computed in Equations (15) to (42), one can then calculate an estimate of systematic error. This was performed for C_T, C_P, C_Q, and η. To get the total amount uncertainty estimate, the random error is required. The random error is the standard deviation of a replicated data set.[20] The standard deviation was calculated for the Aeronaut 16×8 three blade propeller which is the current propeller on the GL-10. This standard deviation was calculated after the propeller had been run through two different advance ratio sweeps at 6,000 rpm at different times. This was to allow for any systematic change to occur over time for a genuine replicated data point. Now knowing a value for the systematic and random error, these terms can be combined as described in Equation (44). Once combined, the results were multiplied by the coverage factor of two so the confidence intervals in the following figures would be approximately ninety five percent. Figure 24 through Figure 27 show the results of these calculations.

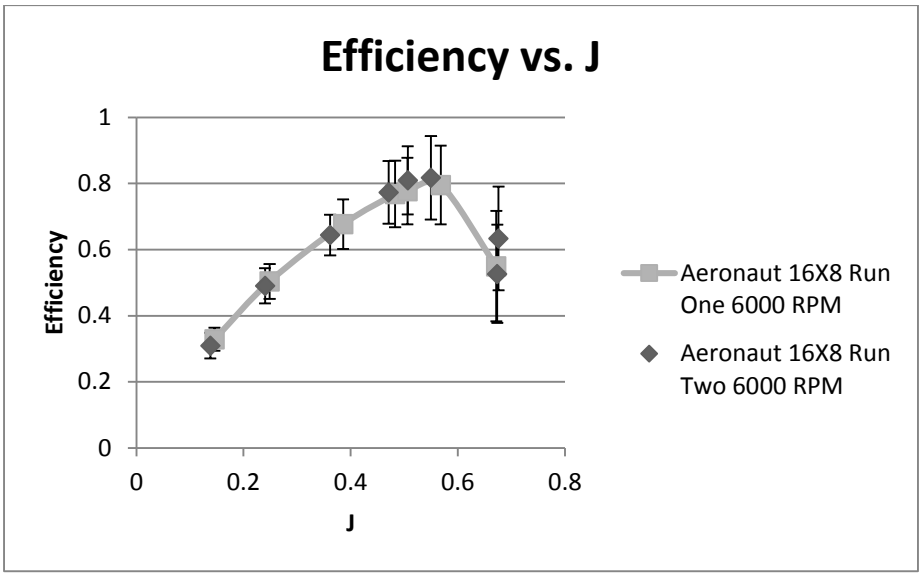

Figure 24- Uncertainty of efficiency

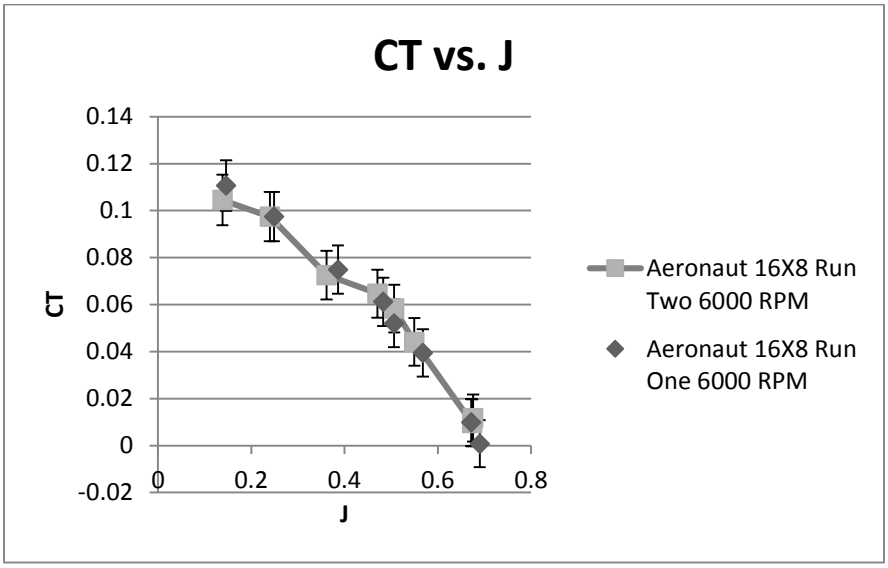

Figure 25- Uncertainty of coefficient of thrust

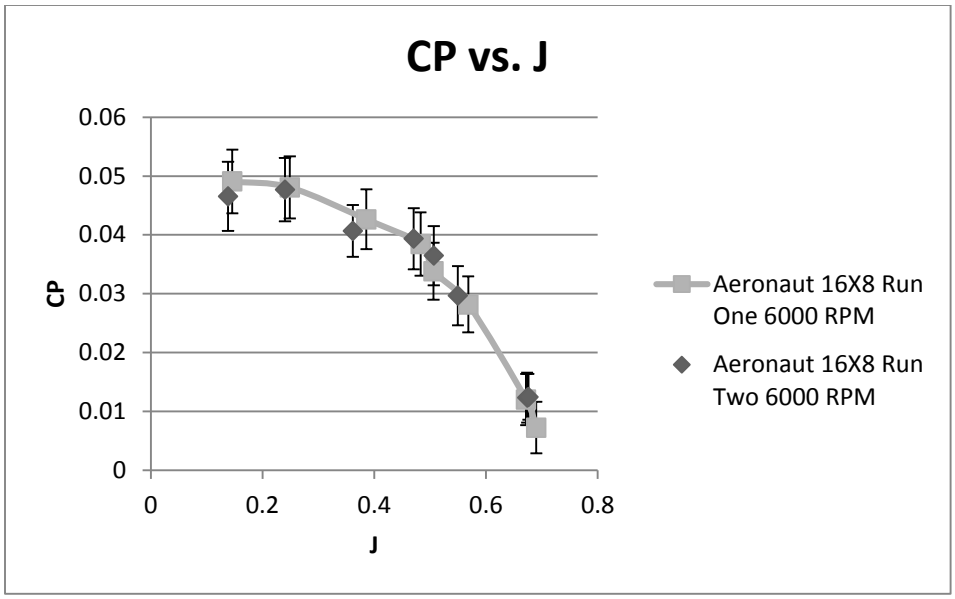

Figure 26- Uncertainty of coefficient of power

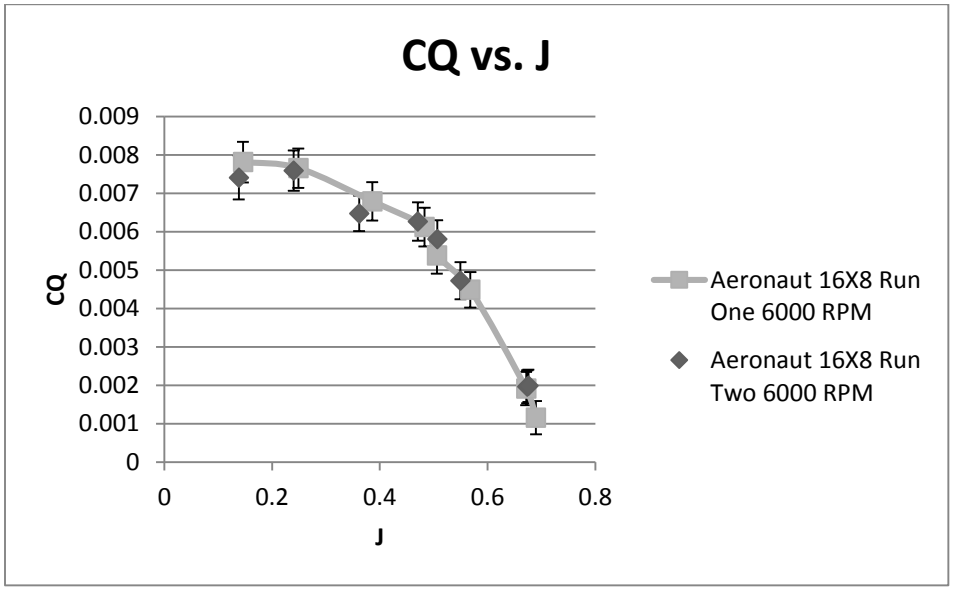

Figure 27- Uncertainty of Coefficient of Torque

The results of the uncertainty calculations show that comparisons between propellers are possible using the current test stand. Starting with the replicated data points, Figure 24 through Figure 27 show there is sufficient agreement between the runs. More importantly the confidence intervals between the two different data sets are very close to each other's length as well. The ninety five percent confidence interval represents an upper bound on the amount of error as it includes estimates of bias and precision. Looking at Figure 25, which shows the uncertainty for the coefficient for thrust, it can be seen that the overall uncertainty is about +/-0.01. Similar small changes were also found for C_P and C_Q uncertainty. Given the objectives of the study, the uncertainty was acceptable for the aerodynamic performance comparisons.

7.2 VALIDATION

7.2.1 AERONAUT 16×8 TO XROTOR

Validation for the propeller test was not as simple as comparing results to other published data. The literature search showed many other experimenters performing similar tasks but using propellers too small to be tested on the designed propeller test stand due to the relatively higher thrust requirements dictated by the load cell resolution of thrust. To solve this problem, it was decided to investigate numerical solutions for basic agreement.

The Aeronaut 16×8 three blade propeller is the current propeller being used on the GL-10. NASA Langley provided a CAD model of this propeller so cross section geometry could be accurately found at radial stations. Knowing this information, a model was built in Xrotor.[18]

Xrotor creates a numerical model of the propeller blade using given information at radial stations. To build a design in Xrotor a distance from the hub to the radial station of interest is divided by the blade radius for each station. Also, a ratio of chord length at each station to the blade radius is defined. Xrotor also requires the angle of inclination of the propeller blade with

respect to the disc for each radial station. Figure 28 shows the Aeronaut 16×8 propeller after the components have been entered.

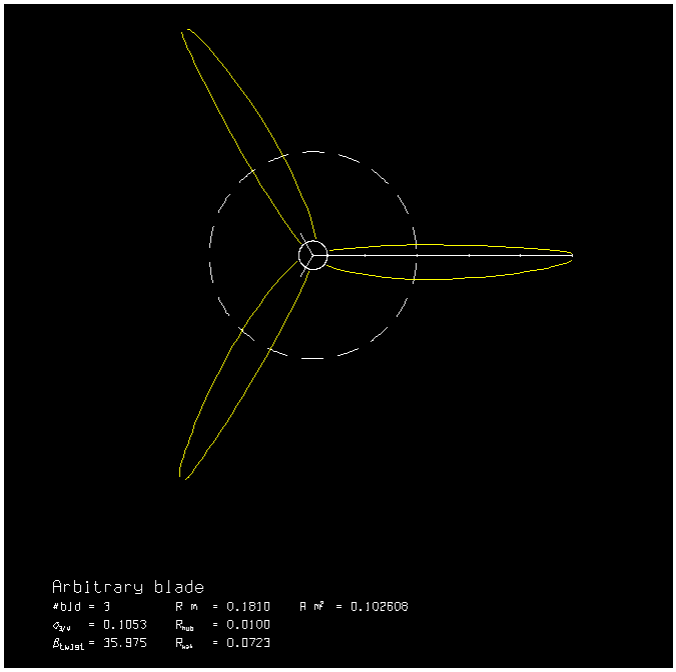

Figure 28- Aeronaut 16×8 geometry plot from Xrotor

Since the angle of attack changes based on the freestream velocity, Xrotor uses a beta angle to define the propeller blade inclination with respect to the plane of rotation as shown in Figure 29.[21] As the magnitude of the RPM or the freestream velocity vectors change this will affect the AOA.[22]

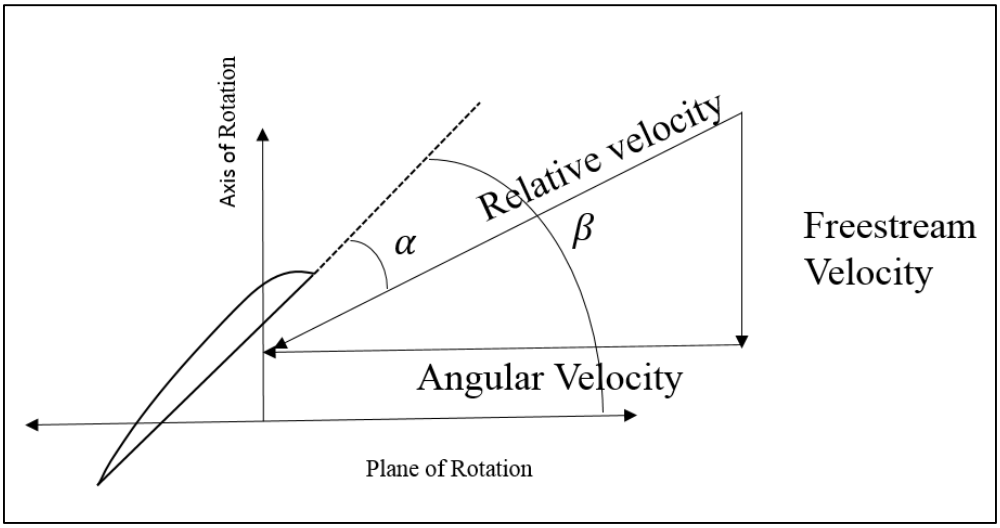

Figure 29- Angle of attack and beta comparison

The exact airfoil shape of the commercially available Aeronaut 16×8 propeller was unavailable from the manufacturer. To get the airfoil characteristics, a method of matching to known airfoils was implemented. Cross sections of the Aeronaut 16×8 scanned CAD model were taken. These slices were then compared to other known airfoil shapes. By observing all of the different slices of the CAD model the airfoil profile appeared to be relatively constant in the spanwise direction. By direct comparison it was found that the Selig S7055 airfoil was a close fit as shown in Figure 30. The gray background is the cross section of the Aeronaut 16×8 CAD model while the dashed black line is fit from coordinates of the S7055 plotted at the same chord length.[23]

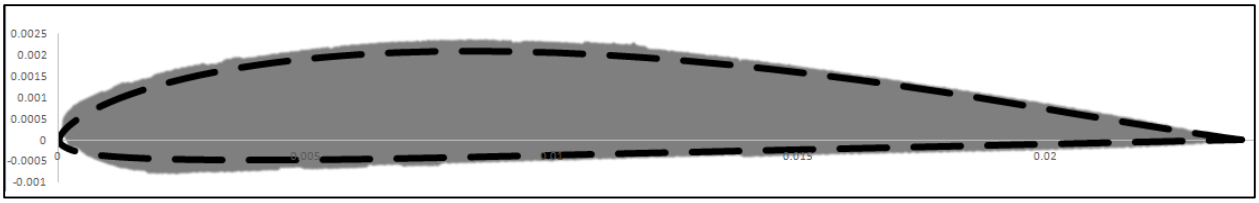

Figure 30- S7055 airfoil compared to CAD model cross section of Aeronaut 16×8

The lift curve slope of the S7055 airfoil was entered into Xrotor by providing Clmax and Clmin at the corresponding angles of attack. These values were selected from published performance data for the S7055 airfoil.[2] Xrotor linearly interpolates the lift curve slope to have coefficient of lift values for each radial station.

Xrotor models the propeller blades as a lifting line with trailing semi-infinite helical vortices. The model of the viscous losses comes from the profile drag of the airfoil section.[23] By entering a freestream velocity and an RPM of the propeller, Xrotor can calculate thrust, torque, and other desired coefficients.

Xrotor has the ability to model a nacelle by again using potential flows. Sources and sinks are combined to create an axisymmetric elementary flow model. The user provides the radius at different radial stations in a similar manner as the propeller blade radial stations. From this, Xrotor can then calculate the unknown source strengths to model the flow correctly. Using the model built in Xrotor, the results were compared graphically to the experimental results. Xrotor results for η, C_T, C_P, vs. J were compared directly to the experimental data. As mentioned before, the only CAD model provided was for an Aeronaut 16×8 three blade propeller. So this propeller was used for validation using Xrotor. Figure 31 through Figure 33 shows the results of the Aeronaut 16×8 propeller blade for a family of constant RPM with varied

velocity. These results show that there are some discrepancies between the experiment and Xrotor.

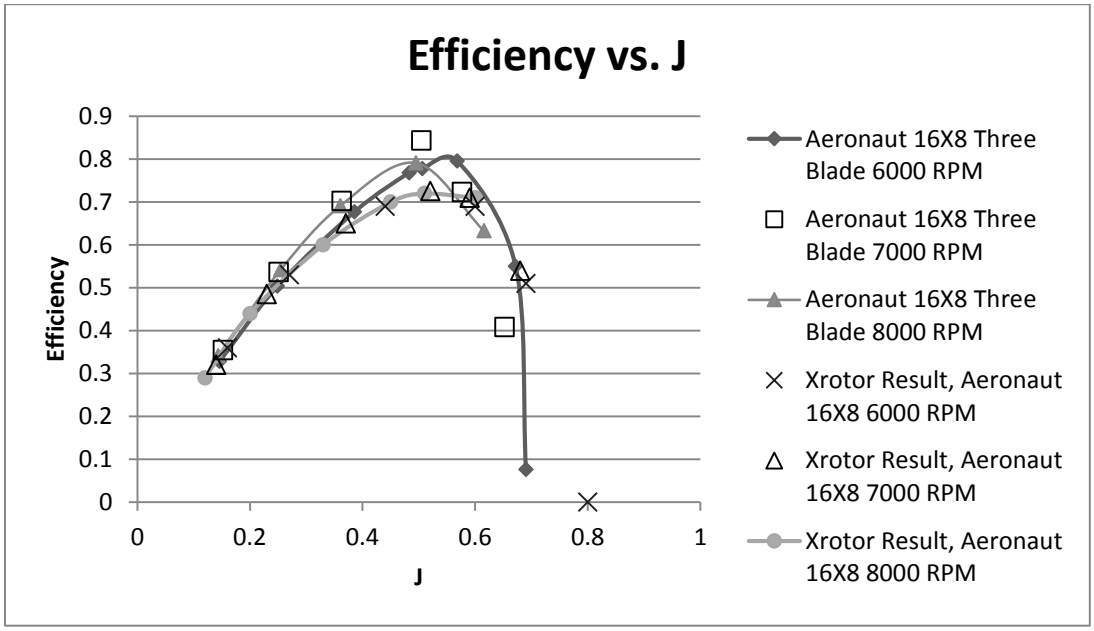

Figure 31- Xrotor efficency results compared to experimental results

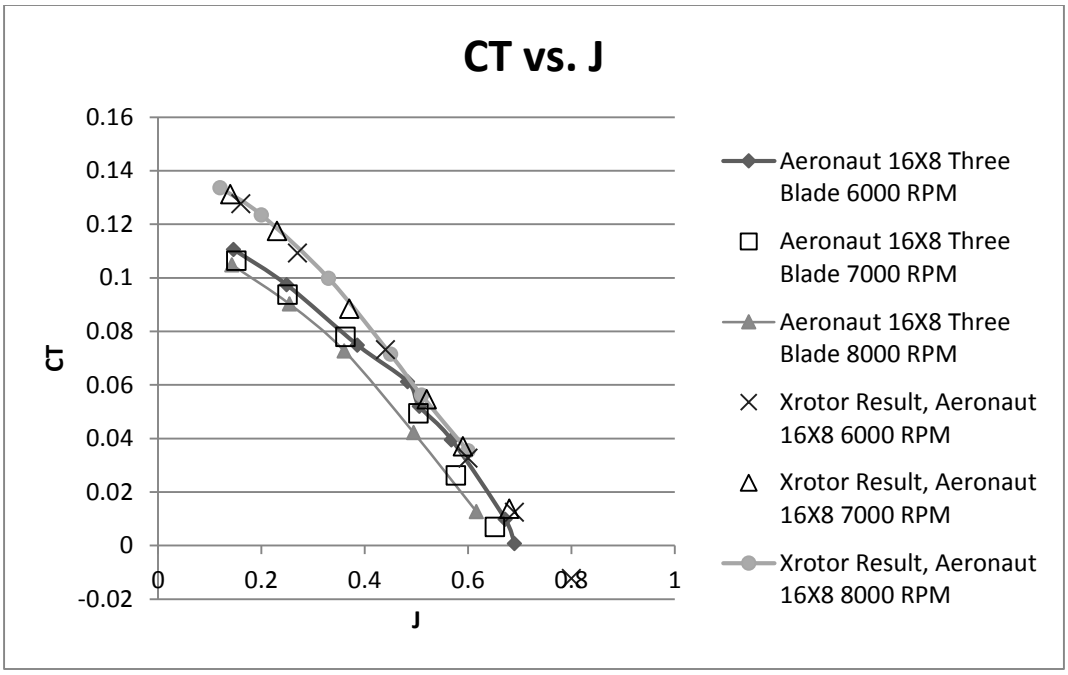

Figure 32- Xrotor coefficient of thrust results compared to experimental results

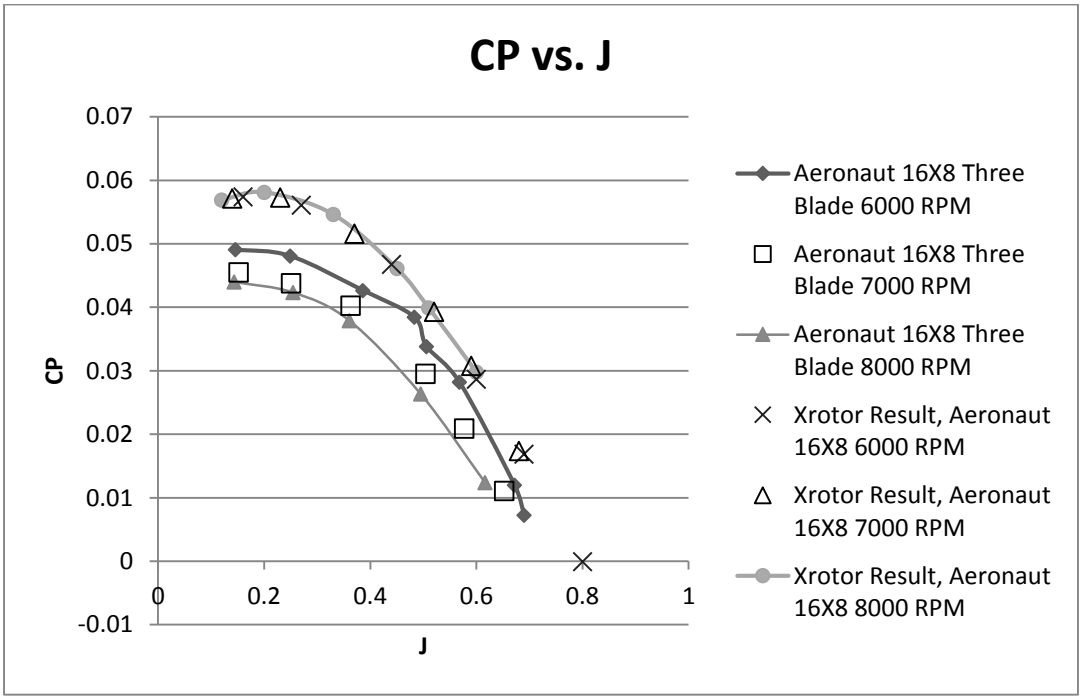

Figure 33- Xrotor coefficient of power results compared to experimental results

Comparing a numerical model to an experimental test is not a comprehensive validation and discrepancies are inevitable. To determine if this error is acceptable, the results of Figure 31 through Figure 33 are plotted with the uncertainty results for the 6,000 RPM case. Figure 34 shows that efficiency vs. advance ratio results from Xrotor still falls within the ninety five percent confidence intervals found previously. However, Figure 35 and Figure 36 do not completely show this for C_T vs. J and C_P vs. J, respectively.

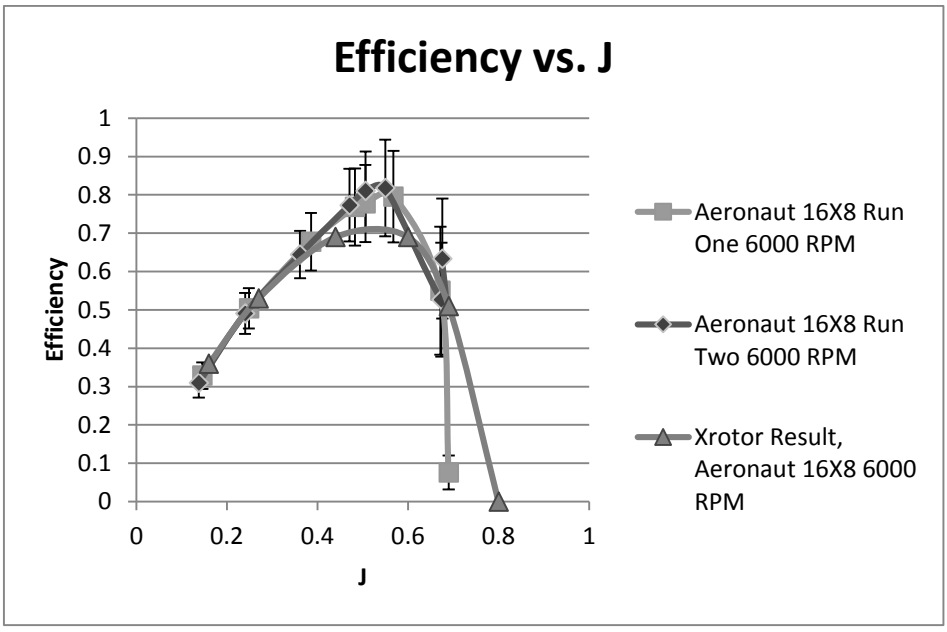

Figure 34- Xrotor efficiency results compared to experimental results with error bars

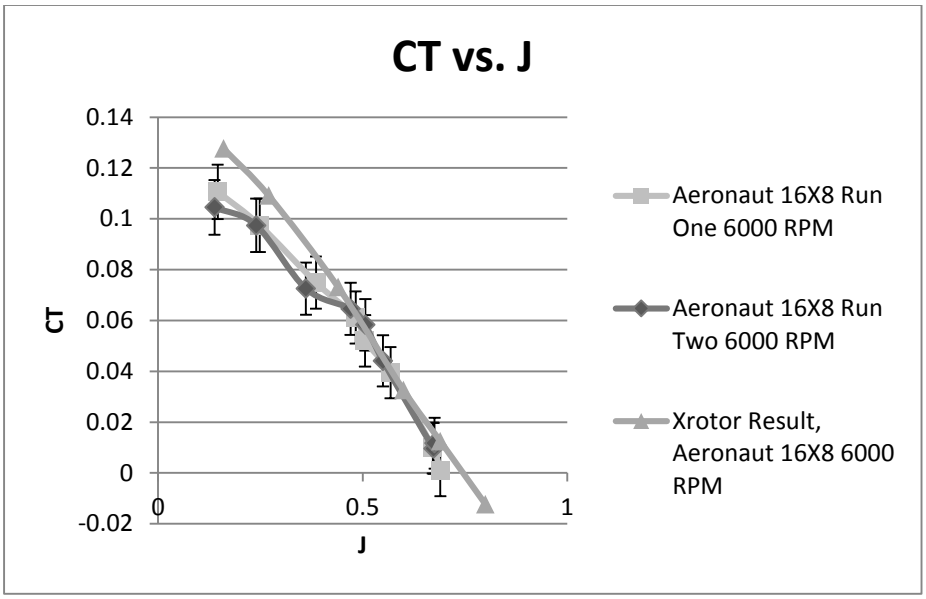

Figure 35- Xrotor coefficient of thrust results compared to experimental results with error bars

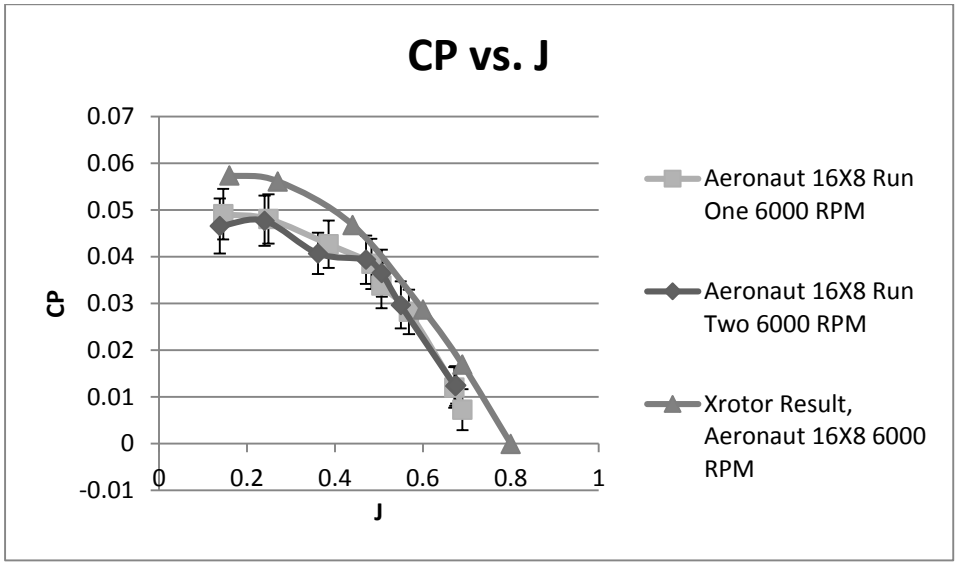

Figure 36- Xrotor coefficient of power results compared to experimental results with error bars

7.2.2 APC 15×8 TO APC DATA

An APC 15×8 was another propeller selected for validation. This propeller meets the requirements to maximize the force applied to the load cell. Numerical data from APC were also available for comparison [24]. Figure 37 shows the experimental results and the APC data are in agreement for the range of advance ratios tested. Figure 38 and Figure 39 show similar trends for experimental vs. APCs results but do not overlay as well. One interesting observation with these plots is the change in slopes for the APC and experimental data appear to occur in the same locations. This can be seen best in Figure 39 in the third set of data points.

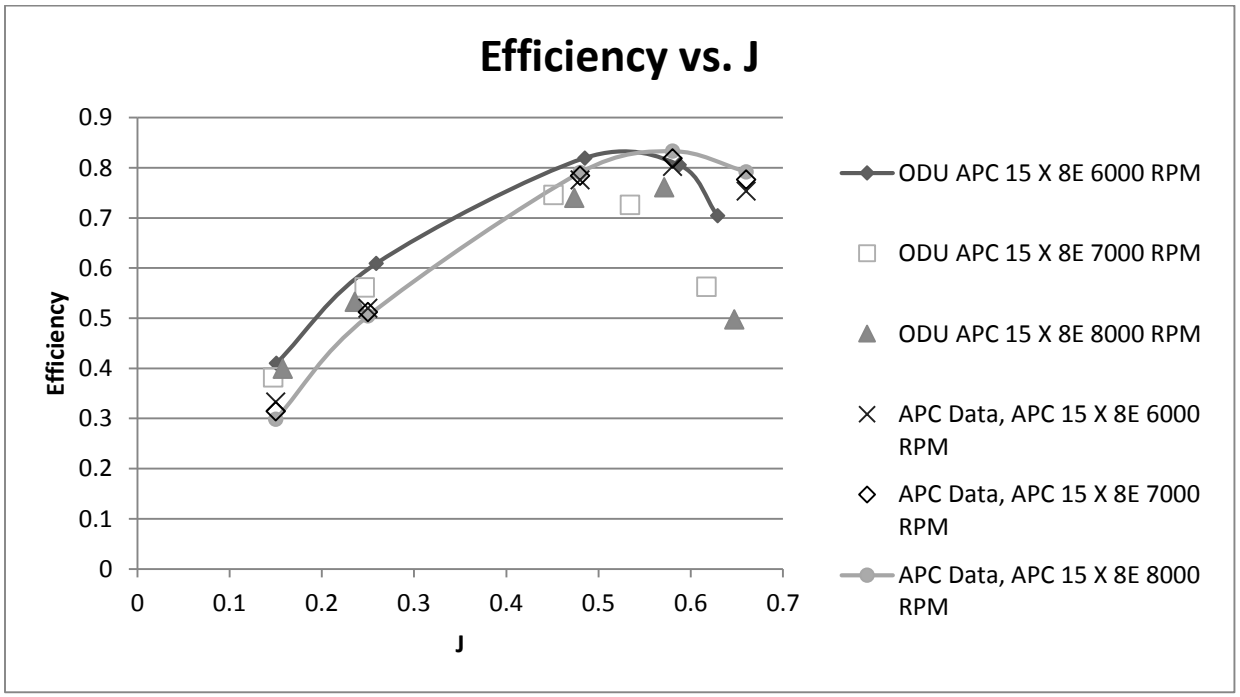

Figure 37- APC efficiency data compared to experimental results

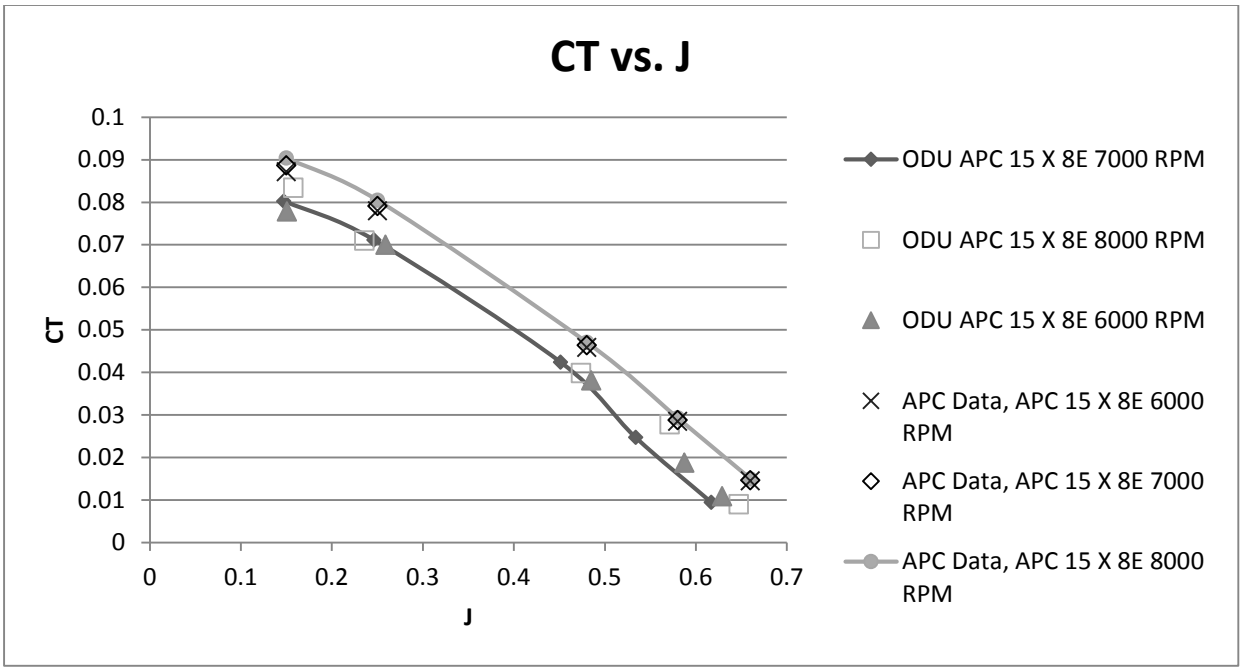

Figure 38- APC coefficient of thrust data compared to experimental results

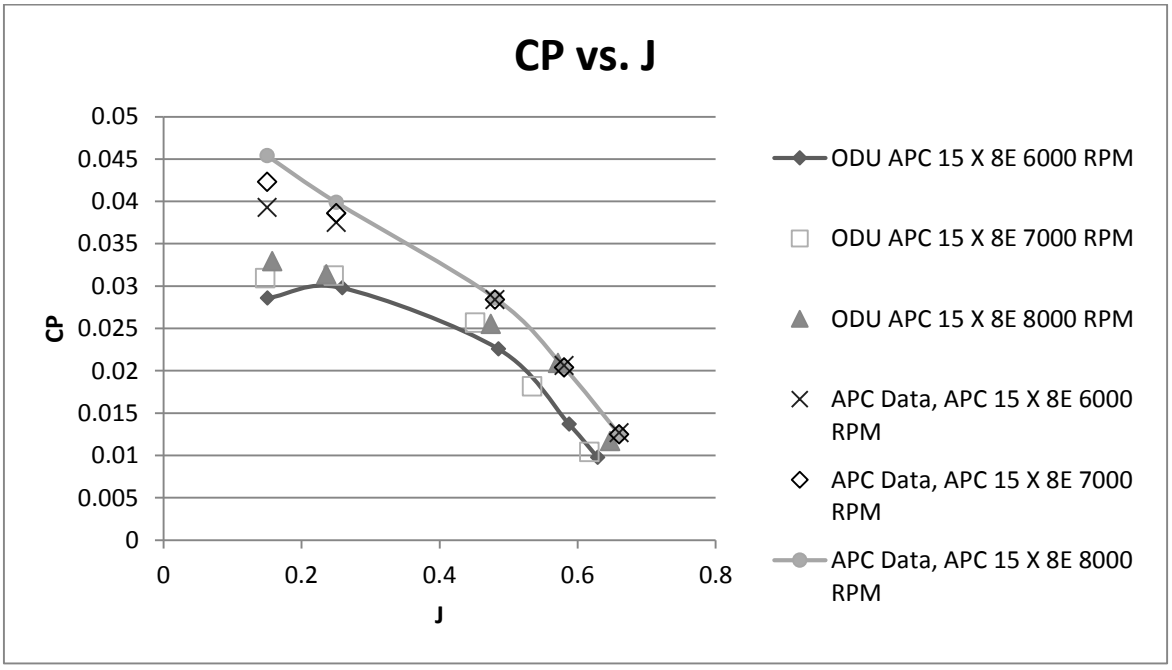

Figure 39- APC coefficient of power data compared to experimental results

With the addition of the corrected velocity from the method previously described, the corrected experimental results show a closer comparison as seen in Figure 40 through Figure 42. It should be stated again that this is a comparison to numerical data so there will be discrepancies. To add to this, the results from APC do not model the nacelle that is directly behind the plane of the propeller. For this project, these results were found to be sufficient in determining the propeller test stand was working properly.

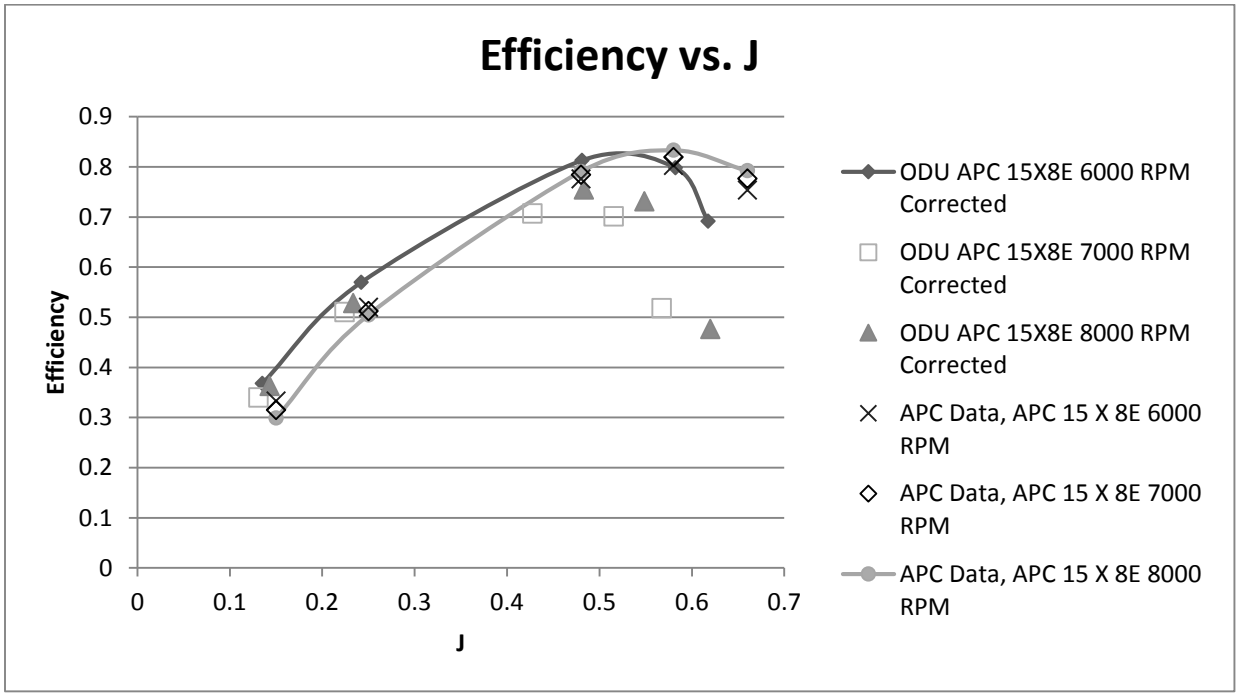

Figure 40- APC efficiency data compared to experimental results with corrected velocity

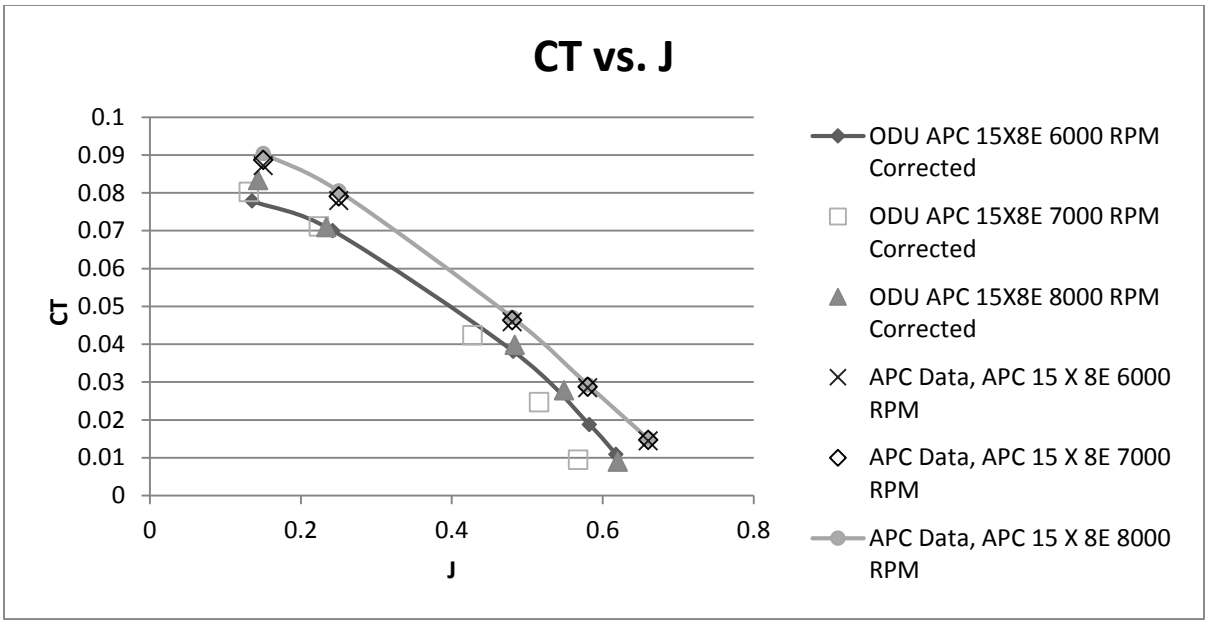

Figure 41- APC coefficient of thrust data compared to experimental results with corrected velocity

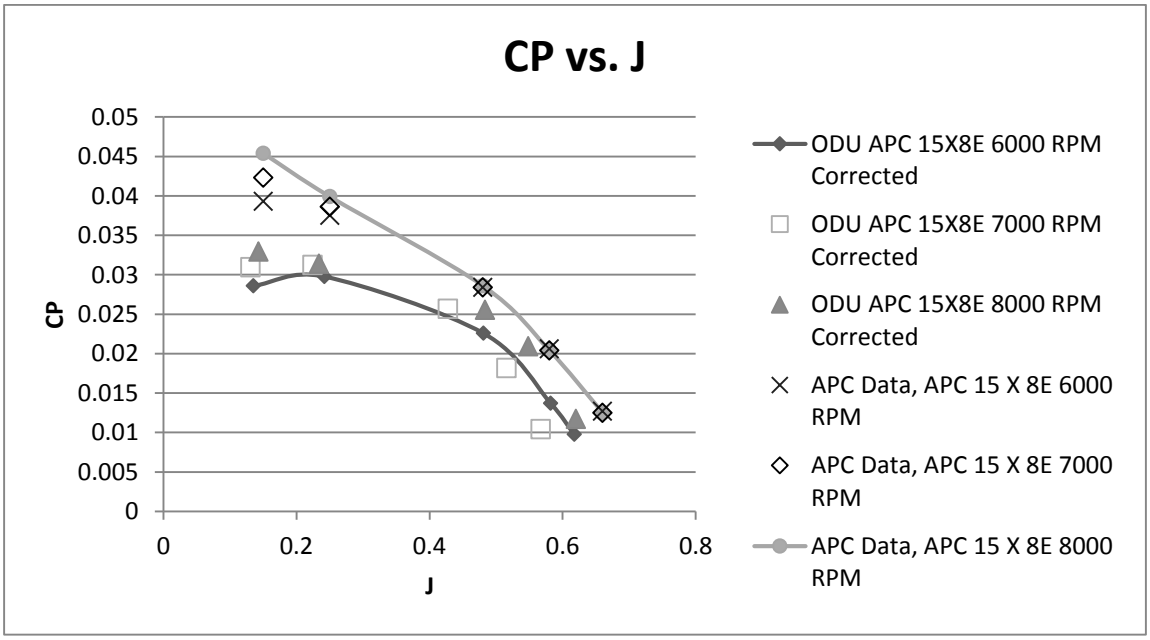

Figure 42- APC coefficient of power data compared to experimental results with corrected velocity

7.2.3 EFFECTS OF LOAD CELL HEATING

The effect of load cell heating was an important consideration in the validation of the previous results. During the validation process, excessive heat was found to have a detrimental effect. In early testing, it was found that the temperature of the motor actually stayed within an acceptable temperature range such that no damage occurred to the motor. However, the heat that was generated by the motor significantly affected the load cell which was discovered later in the test program. The available load cell appears to have very little temperature compensation, so even small changes in temperature (+5° C) affected the readings by tenths of a pound. This small error compounded the problems associated with the excessive load cell range. A residual force or torque value would grow as the motor was left on to collect data while the wind tunnel speed was varied. At one point the residual reading after a test was half a pound. These high residuals made the data unusable particularly for efficiency which depends on thrust and torque. To combat the heating of the load cell, compressed air was used to remove the heat from the rear of the motor. An eighth inch thick piece of G-10 fiberglass board was also added between the motor mount and the cylindrical aluminum spacer attached to the load cell. Figure 43 shows this set up. This reduced the conduction heat transfer between the motor and the aluminum spacer.

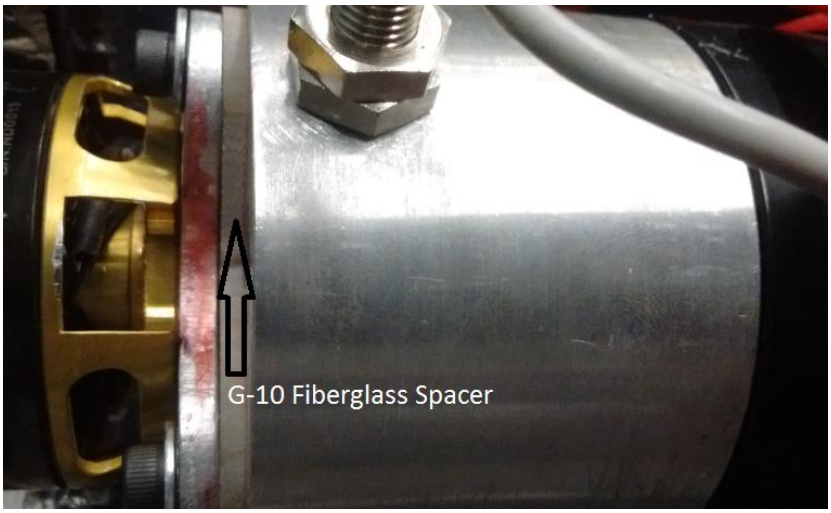

Figure 43- G-10 Fiberglass insulator

With the use of the compressed air, which exited thru the aft end of the nacelle, and the G-10 fiber glass insulator, residuals were reduced to reasonable values. Figure 44 through Figure 46 shows that these cooling measures are effective. Replicate One and Two were collected on the same day with a six hour time difference. Replicate Three was collected the next day with the test stand starting at room temperature. Replicate Four was performed the same day as replicate three but after several other propellers were tested. This was to see if measurements would change after several tests even with the compressed air on. The four replicated data runs are seen to overlay each other. Following this test it can be seen that any small change in temperatures do not have a drastic effect.

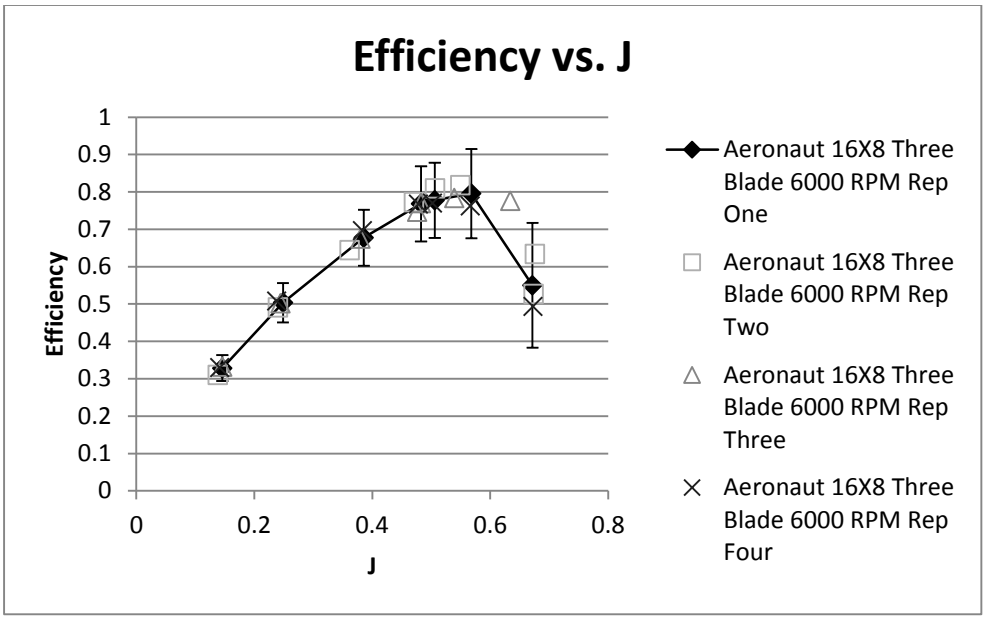

Figure 44- Aeronaut 16×8 replicated data of efficiency vs. advance ratio

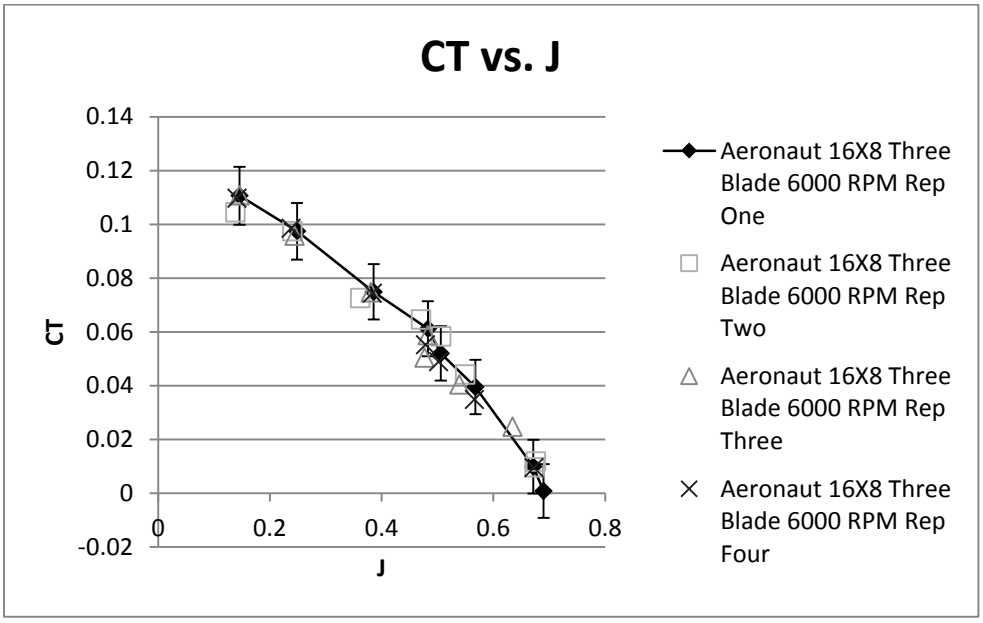

Figure 45- Aeronaut 16×8 replicated data of coefficient of thrust vs. advance ratio

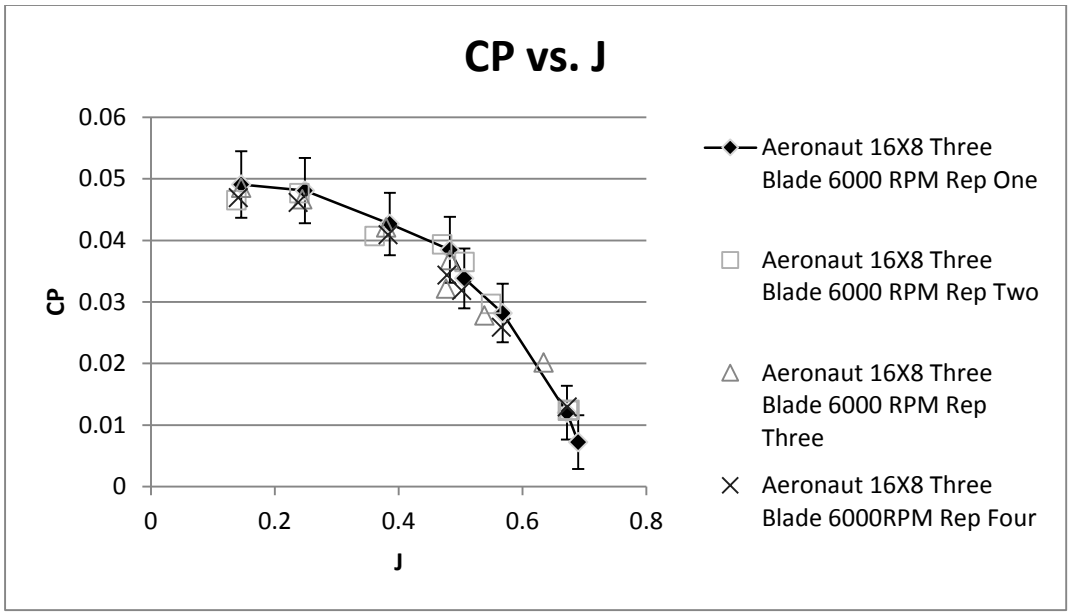

Figure 46- Aeronaut 16×8 replicated data of coefficient of power vs. advance ratio

7.3 CURRENT GL-10 PROPELLER

7.3.1 PERFORMANCE

The Aeronaut 16×8, seen in Figure 47, is the baseline propeller used for comparison of potential improved propellers.

Figure 47- Top view of Aeronaut 16×8 three blade propeller

In the ODU Wind Tunnel, three series of RPM sweeps were performed while varying velocity. As stated previously, the cruise speed for is the GL-10 is 44 knots. If the advance ratio is calculated for 44 knots at 6,000 RPM the result is 0.55. Figure 48 shows an advance ratio of 0.55 allows the motor to perform most efficiently during cruise.

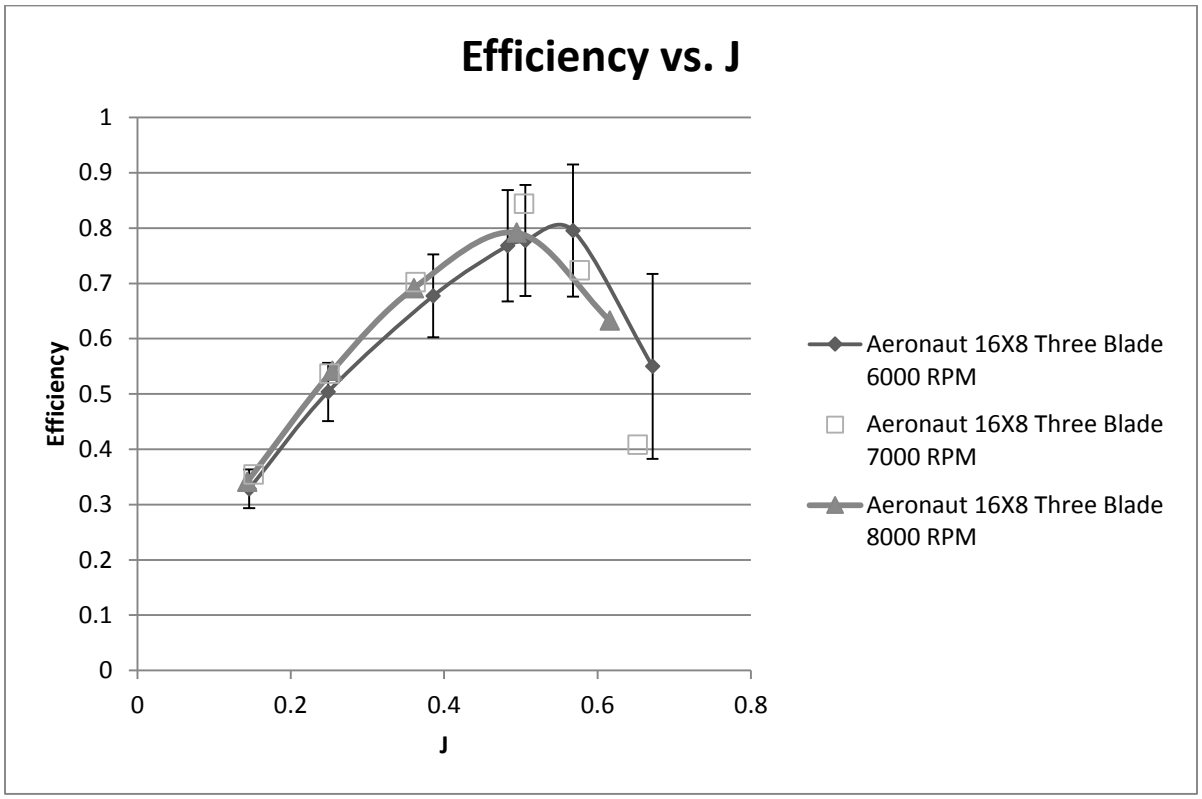

Figure 48- Aeronaut 16×8 Efficiency vs. advance ratio results for baseline

Figure 49 and Figure 50 show some interesting trends of the Aeronaut 16×8 propeller. It can be seen as the RPM increases from 6,000 to 8,000, the coefficient of thrust actually decreases when it is expected to increase. The coefficient of power shows this same trend. A possible reason for this behavior may lie in the design's intended use. The Aeronaut 16×8

propeller is designed for a radio control model motor glider. To reduce drag when not in use, the propeller folds against the fuselage. However, this design also allows the propeller to fold into the direction of the flow as well. As RPM increases the propeller blades may pivot into the freestream flow direction which changes the AOA. This change in AOA then effects how much lift and drag is produced. The trends of better performance at lower RPM are only seen in propellers manufactured by Aeronaut that fold. This result was not seen for any other propeller blade manufacturer, but they are all non-folding designs. It's also possible that the thin sections of the Aeronaut blades unload at higher RPM through deformation.

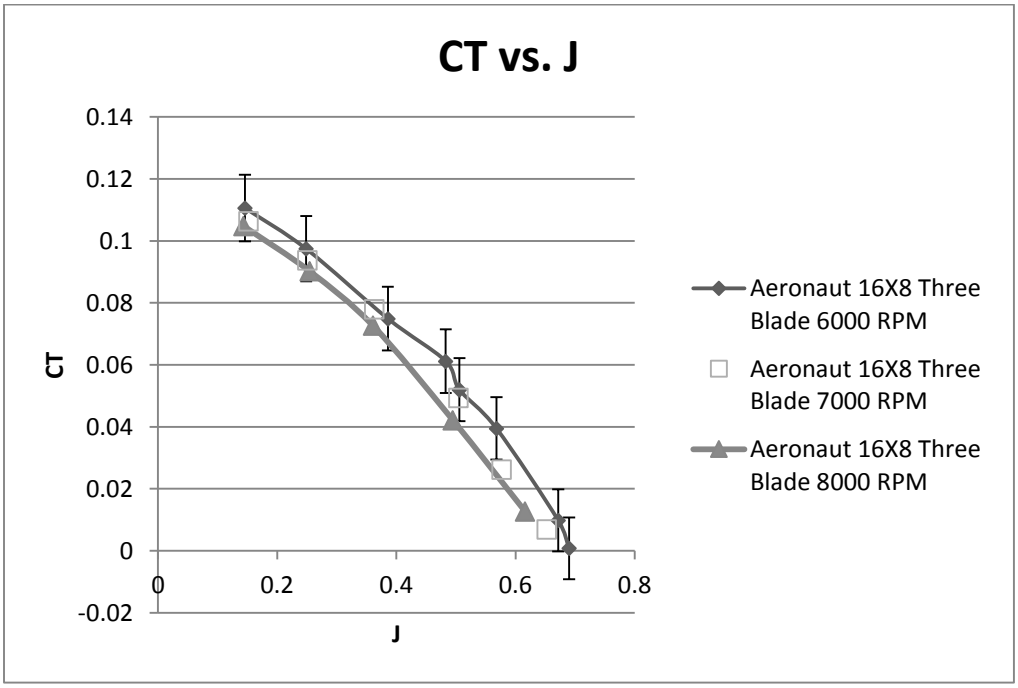

Figure 49- Aeronaut 16×8 coefficient of thrust vs. advance ratio results for baseline

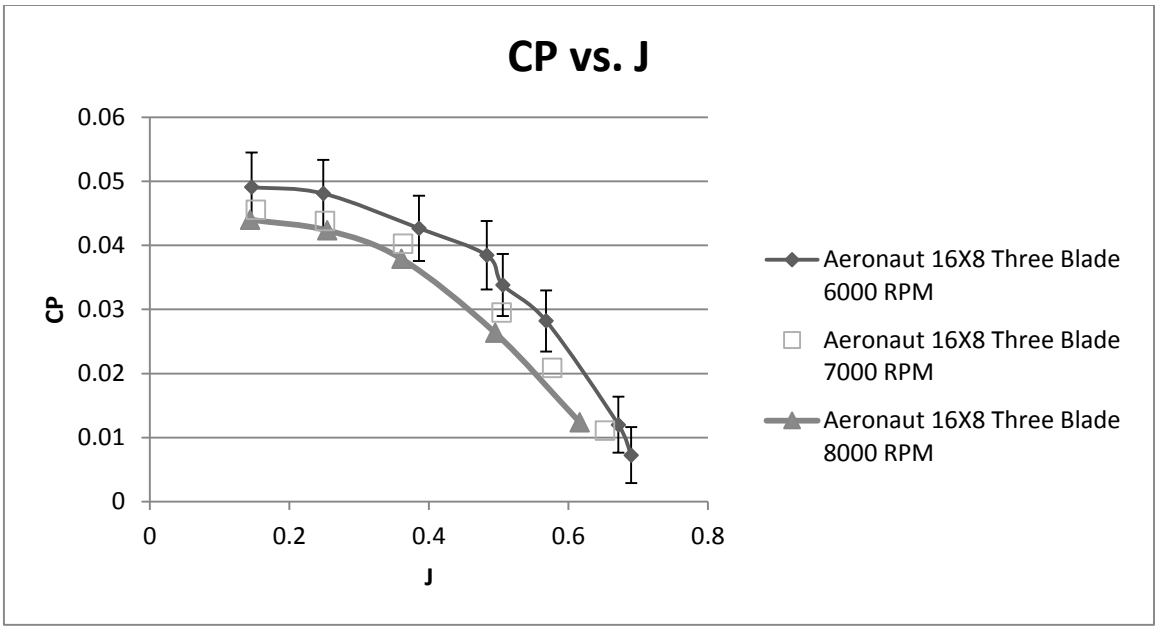

Figure 50- Aeronaut 16×8 coefficient of power vs. advance ratio results for baseline

7.3.2 ACOUSTICS

Acoustic data in the ODU Wind Tunnel were collected with zero freestream velocity. Acoustic data and performance data were collected simultaneously to create Figure 51. The efficiency shown is found by using the static efficiency, Equation (6). The SPLA dB was found by integrating under the A-weighted SPLA vs. frequency plot for each data point as seen in Figure 52. Figure 51 shows as thrust increases, hence RPM, the efficiency starts high and then decreases by 0.02 before it increases again. However, from the uncertainty study of dynamic efficiency this change is subject to error in the results. Also, the Acoustic noise increases as thrust is increased, which is expected from literature.[6]

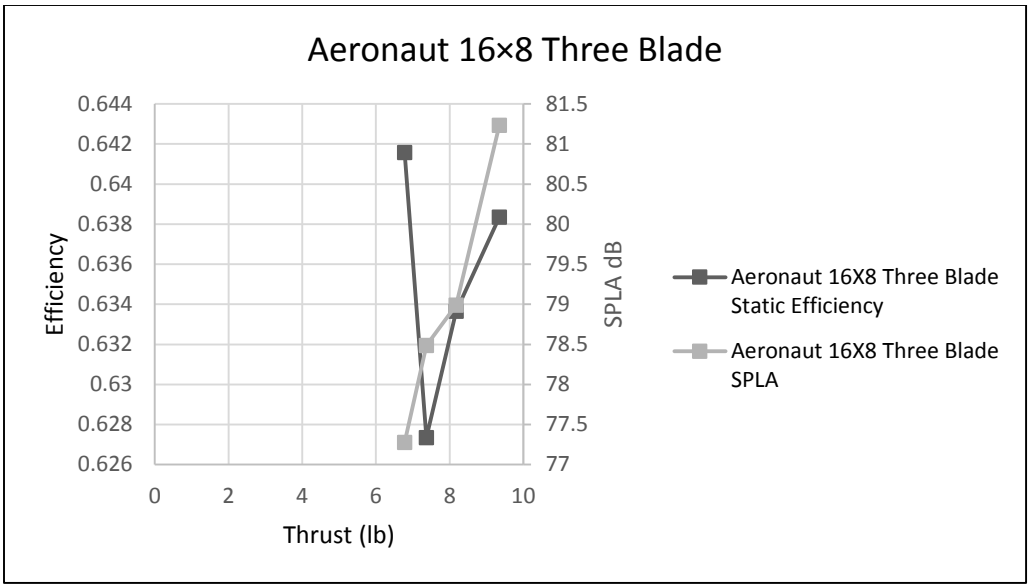

Figure 51- Efficiency and A-weighted sound pressure level vs. thrust for the Aeronaut 16×8

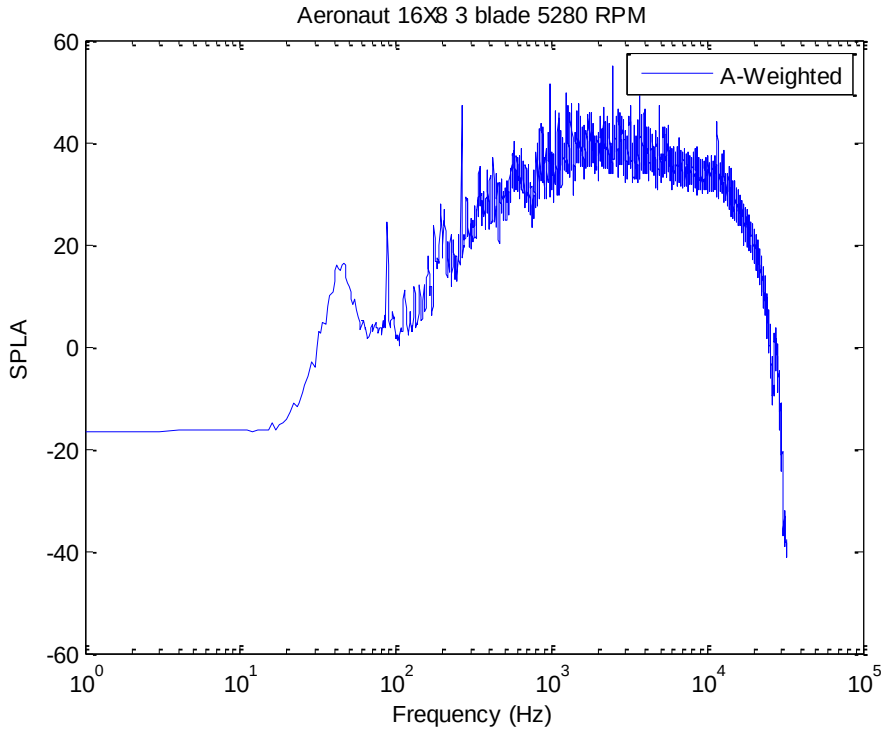

Figure 52- A-weighted sound pressure level vs. frequency for Aeronaut 16×8

Acoustic data collected in the anechoic chamber were processed the same way as the collected wind tunnel acoustic data. The anechoic chamber data were compared to the data collected in the wind tunnel. Figure 53 shows the results from each test location. As expected, for a given propeller, the SPLA measured from the wind tunnel was always greater than the anechoic chamber measurements. By evaluating SPLA versus RPM using a first order fit, there is an offset of approximately six decibels and the trend lines are almost parallel. From this result a correction factor may be found in order to eliminate the need to use an anechoic chamber for every test.

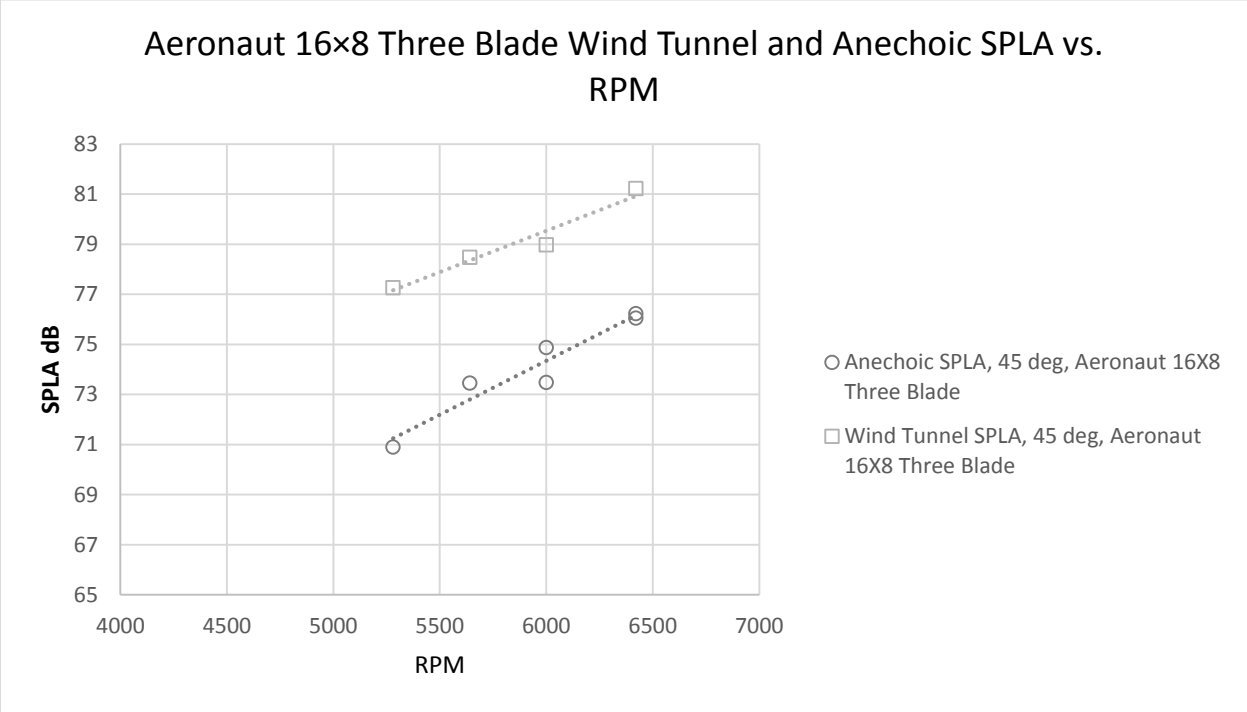

Figure 53- Comparison of wind tunnel and anechoic chamber acoustic noise

Figure 54 suggest, based on the anechoic chamber results, that the microphone placement in the wind tunnel at 45 degrees was appropriate. Lines shown are first order fits. The acoustic measurements from the anechoic chamber show the microphone in the plane of the propeller is quieter then measurements made downstream in the tunnel.

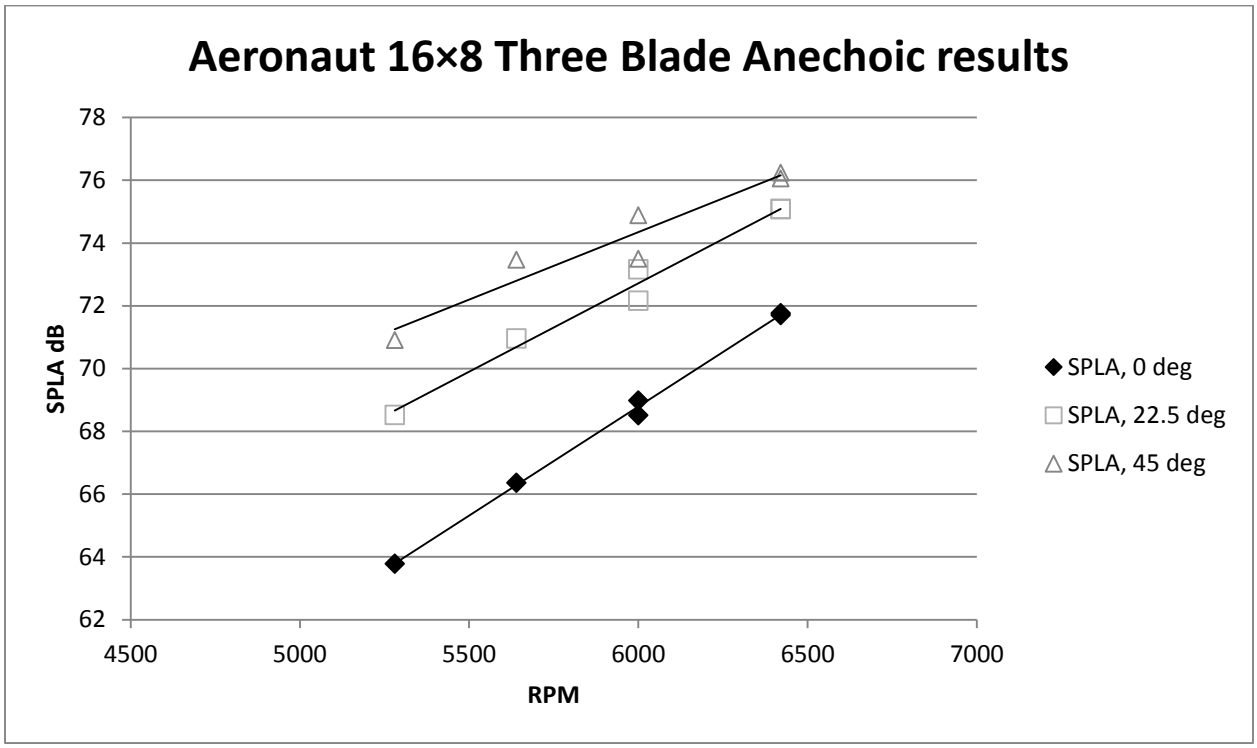

Figure 54- Anechoic chamber Aeronaut 16×8 three blade acoustic data at varying angles

7.4 GL-10 CANDIDATE PROPELLERS

In addition to evaluating the Georgia Tech propeller design, performance and acoustic data were collected for several candidate commercially available propellers. Since the current propeller on the GL-10 is a folding propeller, a logical choice of candidates included other

propellers that were within the family of Aeronaut folding propellers. If there was an Aeronaut propeller that was more appropriate for the GL-10, then redesign of a folding mechanism could be avoided and the new propeller directly installed. Following a market survey, other propeller candidates included Master Airscrew and Vess brand propellers.

7.4.1 PERFORMANCE

7.4.1.1 AERONAUT TWO BLADE PROPELLERS

Figure 55- Aeronaut 16×6, 8, 10 two blade propellers

Figure 55 shows the three different two blade Aeronaut propellers tested. Results for the measured efficiency of the Aeronaut 16×6 two blade propellers are shown in Figure 56, where performance was found to be less efficient then the baseline propeller. However, as the pitch of the Aeronaut two blade propellers was increased, efficiency increased as well and the maximum was moved towards more appropriate advance ratios for cruise conditions. Figure 57 and Figure 58 show this for the 16×8 and 16×10 Aeronaut two blade propellers, respectively.

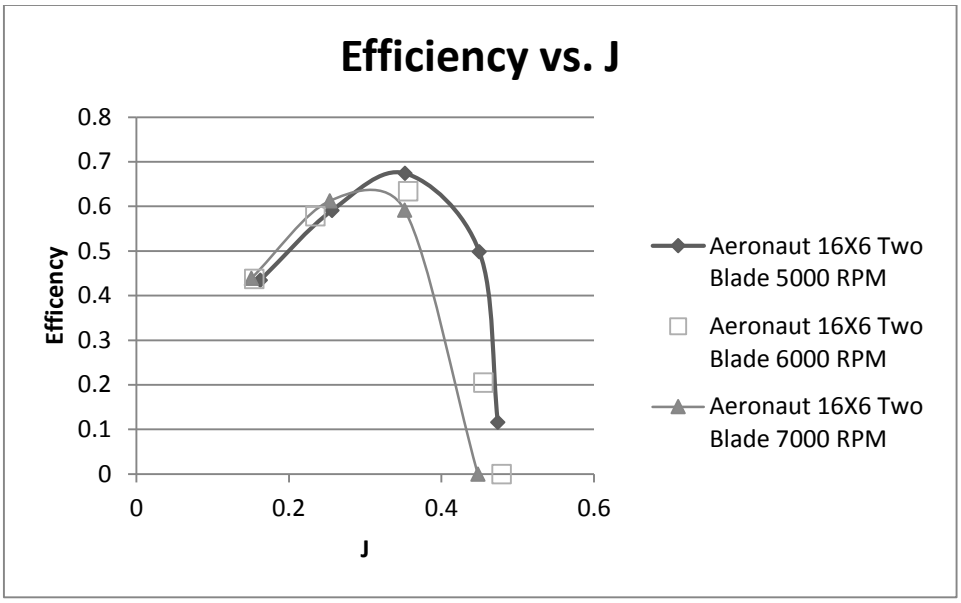

Figure 56- Aeronaut 16×6 two blade efficiency vs. advance ratio

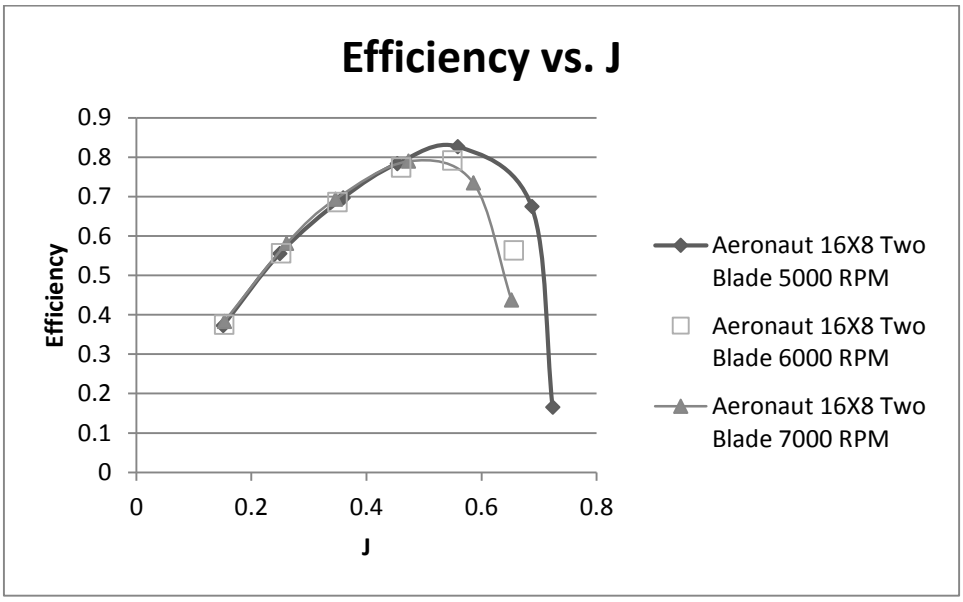

Figure 57- Aeronaut 16×8 two blade efficiency vs. advance ratio

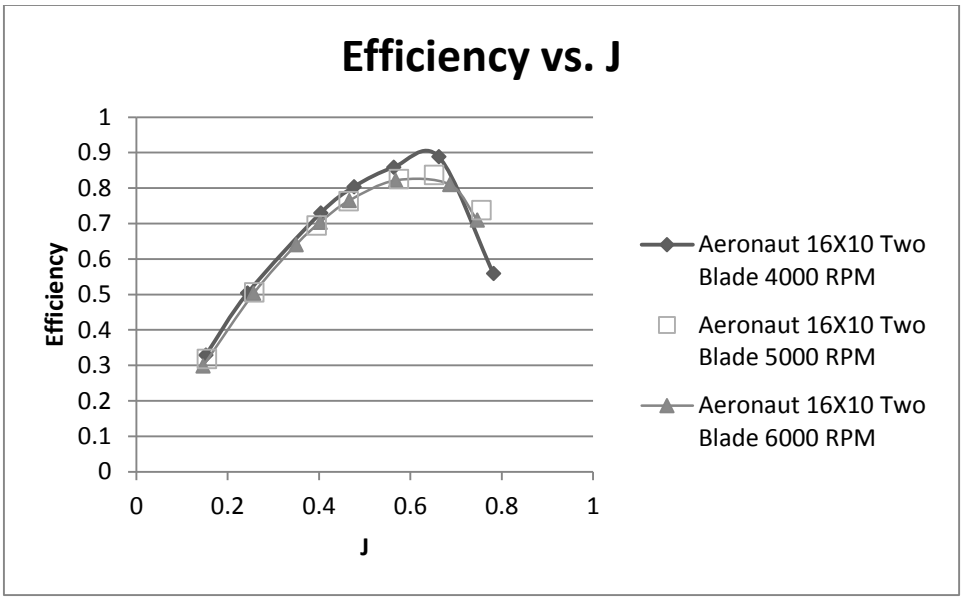

Figure 58-Aeronaut 16×10 two blade efficiency vs. advance ratio

The coefficient of thrust for these two blade propellers was found to be under the required value established by the baseline propeller. Figure 59 through Figure 61 show these results for the three different pitches. There is an increase in coefficient of thrust as pitch increases but it does not come close to the baseline. An argument could be made to increase RPM on these propellers. However, as seen in the baseline plots, increasing RPM actually decreases the coefficient of thrust. Due to the results found for this propeller, increasing the RPM is not an option to increase the coefficient of thrust.

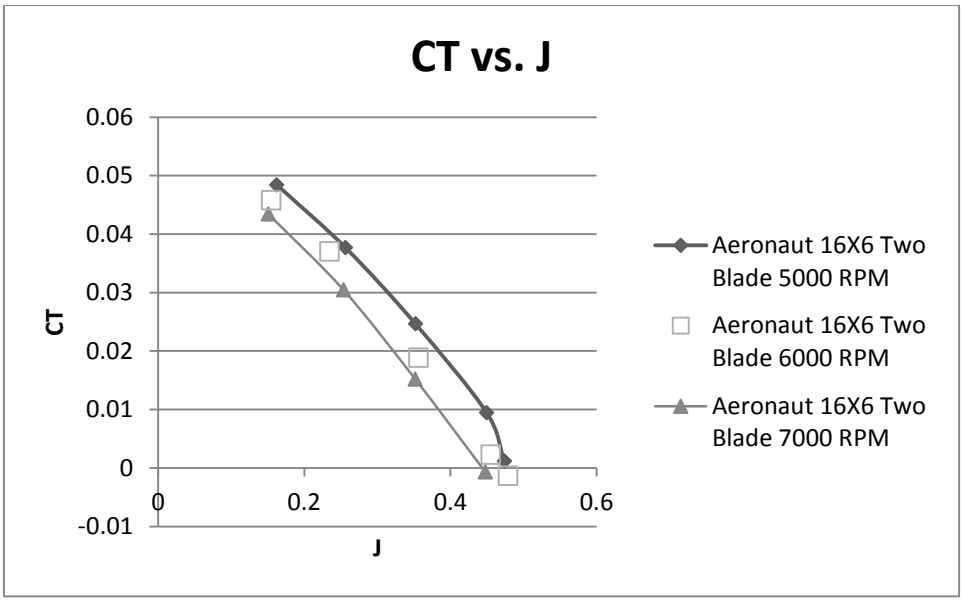

Figure 59- Aeronaut 16×6 two blade coefficient of thrust vs. advance ratio

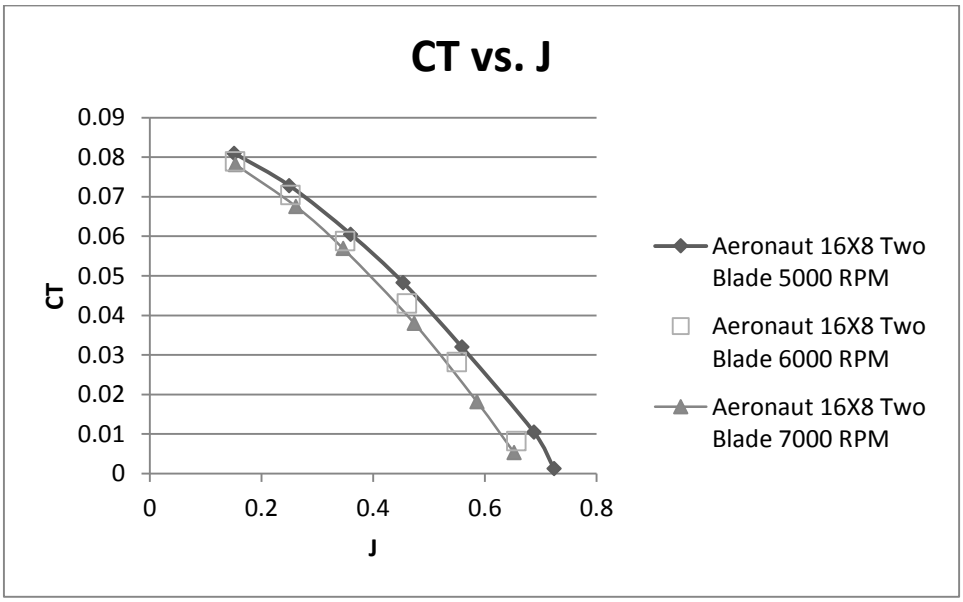

Figure 60- Aeronaut 16×8 two blade coefficient of thrust vs. advance ratio

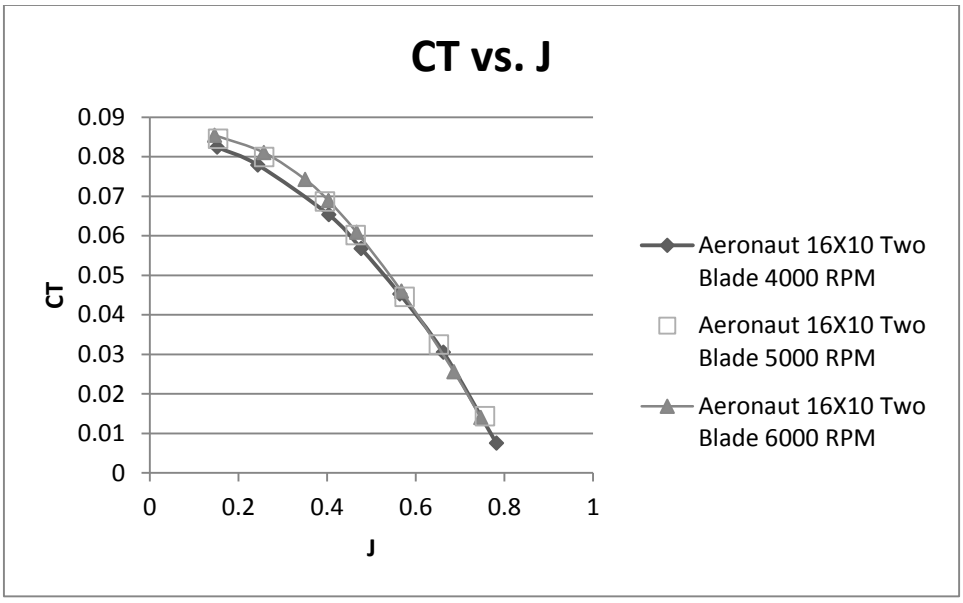

Figure 61- Aeronaut 16×10 two blade coefficient of thrust vs. advance ratio

Coefficient of power also had a significant difference from the baseline. There is one less blade from the baseline in the flow so this extra drag, or power requirement, is removed. Figure 62 through Figure 64 shows this. In these figures, it can be seen that as the pitch of a propeller blade is increased, there is a penalty in the increase of power required.

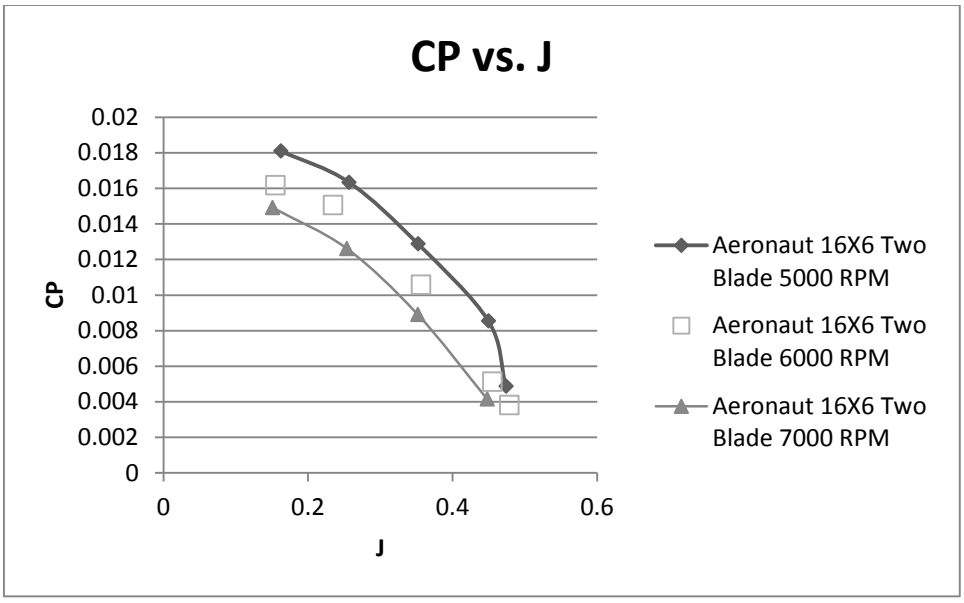

Figure 62- Aeronaut 16×6 two blade coefficient of power vs. advance ratio

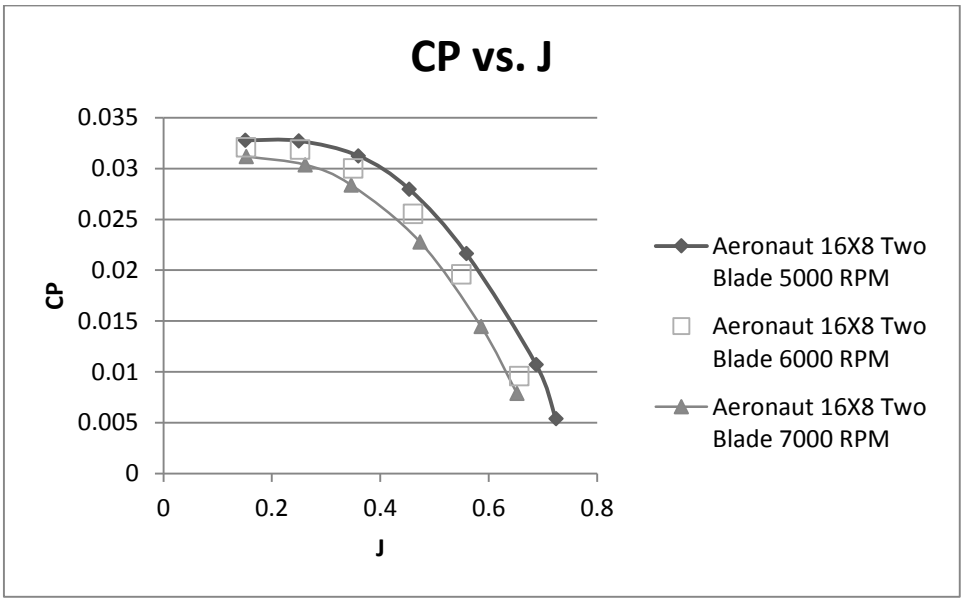

Figure 63- Aeronaut 16×8 two blade coefficient of power vs. advance ratio

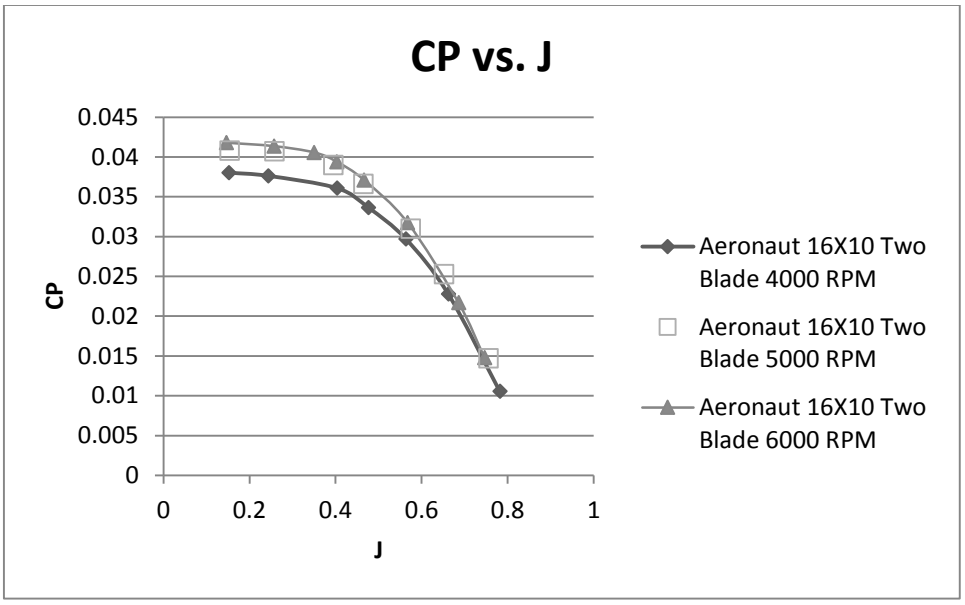

Figure 64- Aeronaut 16×10 two blade coefficient of power vs. advance ratio

7.4.1.2 AERONAUT THREE BLADE PROPELLERS

Figure 65- Candidate Aeronaut 16×6, 10 three blade propellers

Along with the baseline propeller, two other Aeronaut three bladed propellers were tested. These were the 16×6 and 16×10 which can be seen in Figure 65. Figure 66 shows the results of the Aeronaut 16×6 tests. As seen in the two blade case the efficiency has decreased from the baseline. The maximum possible efficiency is also not close to the cruising velocity advance ratio.

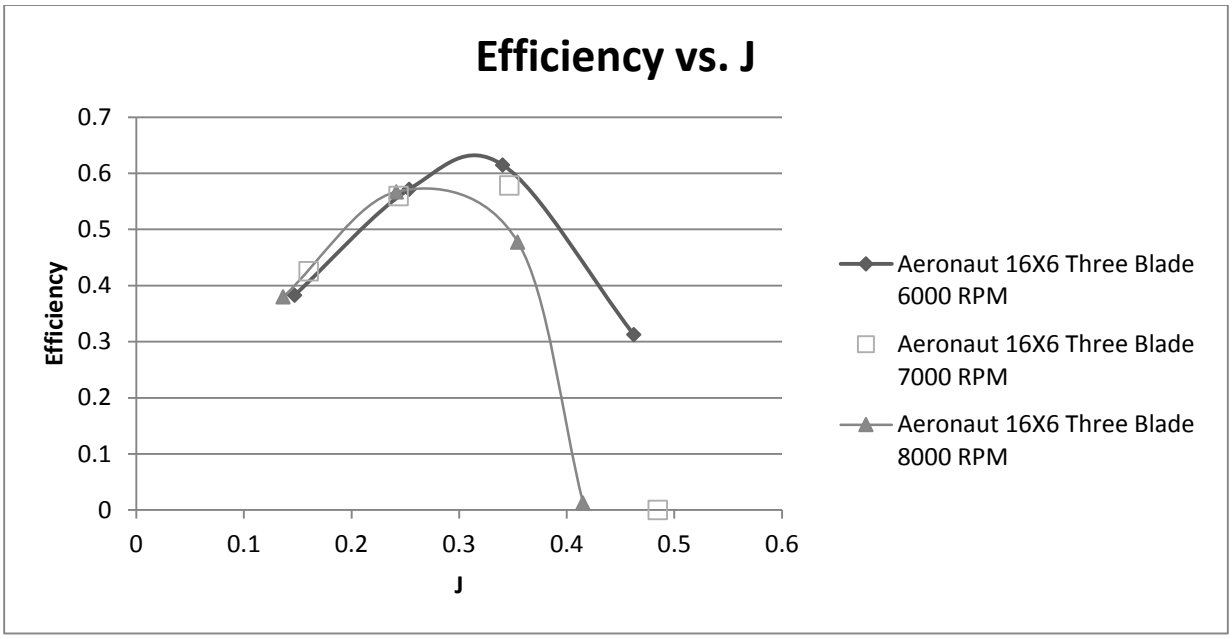

Figure 66- Aeronaut 16×6 three blade efficiency vs. advance ratio results

The results of the Aeronaut 16×10 propeller shown in Figure 67 do show an increase in efficiency. This is only a small increase and must be vetted by considering uncertainty, but it can be seen this propeller would be beneficial at higher velocities. The maximum on the plot is shifted to a higher advance ratio of 0.6 showing that the velocity for maximum efficiency is higher.

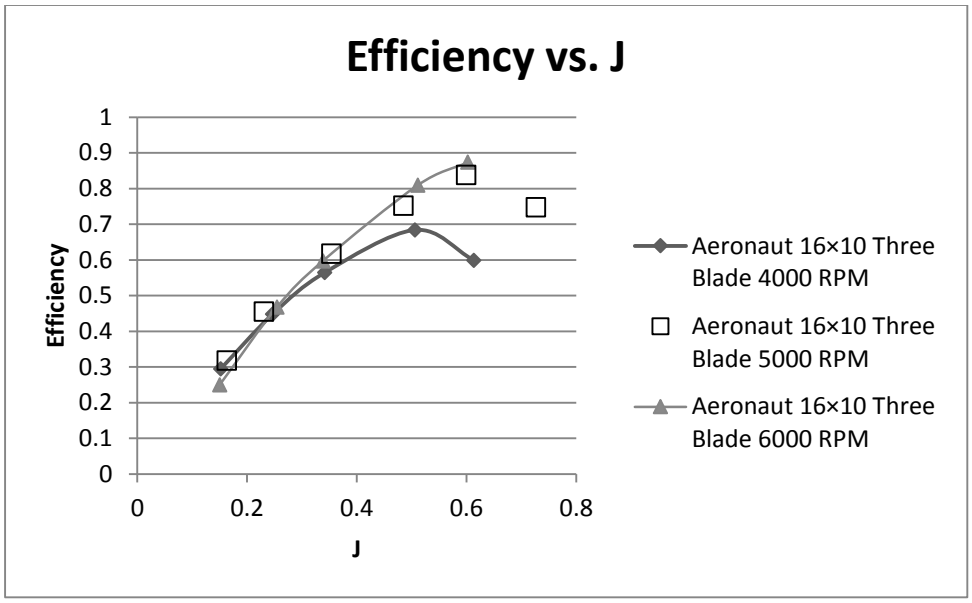

Figure 67- Aeronaut 16×10 three blade efficiency vs. advance ratio results

As for the coefficient of thrust the Aeronaut 16×6 propeller was significantly lower than the base line. Figure 68 shows the results of the 16×6 propeller. Again, as seen with other Aeronaut designs, as the RPM increases the coefficient of thrust decreases. The results of the 16×10 propeller shown in Figure 69, show this same trend as well. However, the Aeronaut 16×10 coefficient of thrust is greater or the equivalent to the baseline.

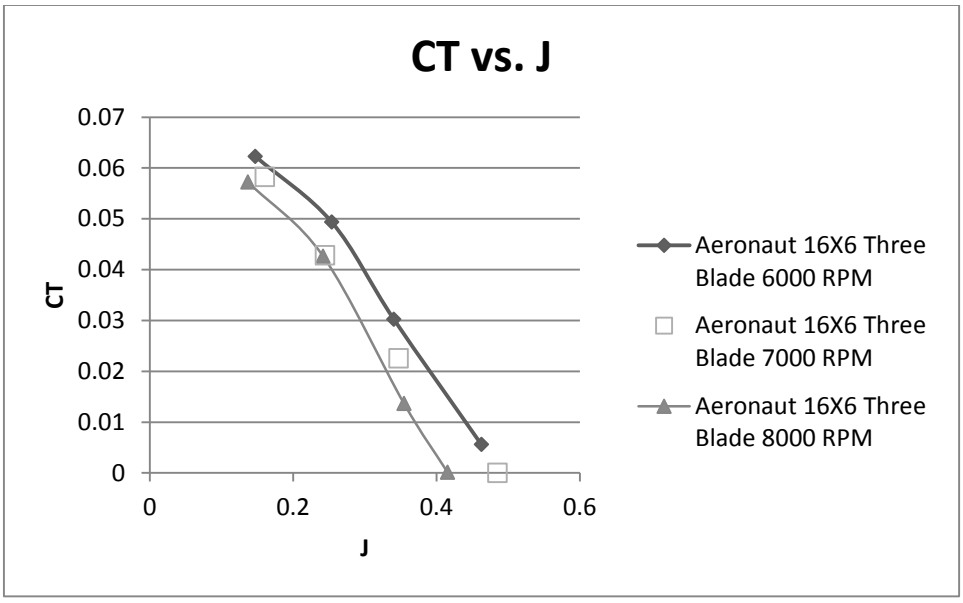

Figure 68- Aeronaut 16×6 three blade coefficient of thrust vs. advance ratio results

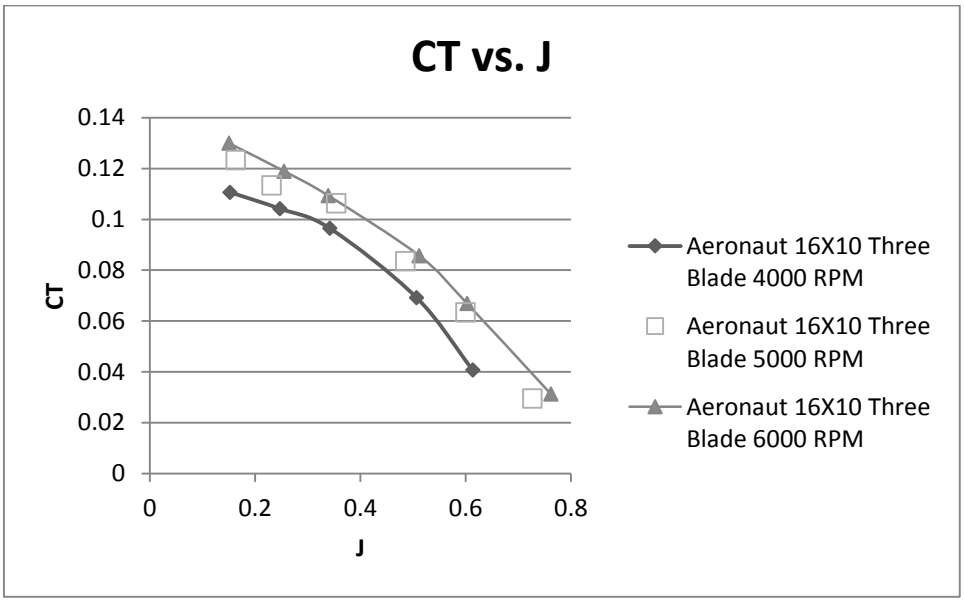

Figure 69- Aeronaut 16×10 three blade coefficient of thrust vs. advance ratio results

The coefficient of power results show the Aeronaut 16×6, shown in Figure 70, is favorable compared to the baseline. For the Aeronaut 16×10 the coefficient of power was greater than the baseline. Figure 71 shows the coefficient of power vs. advance ratio results.

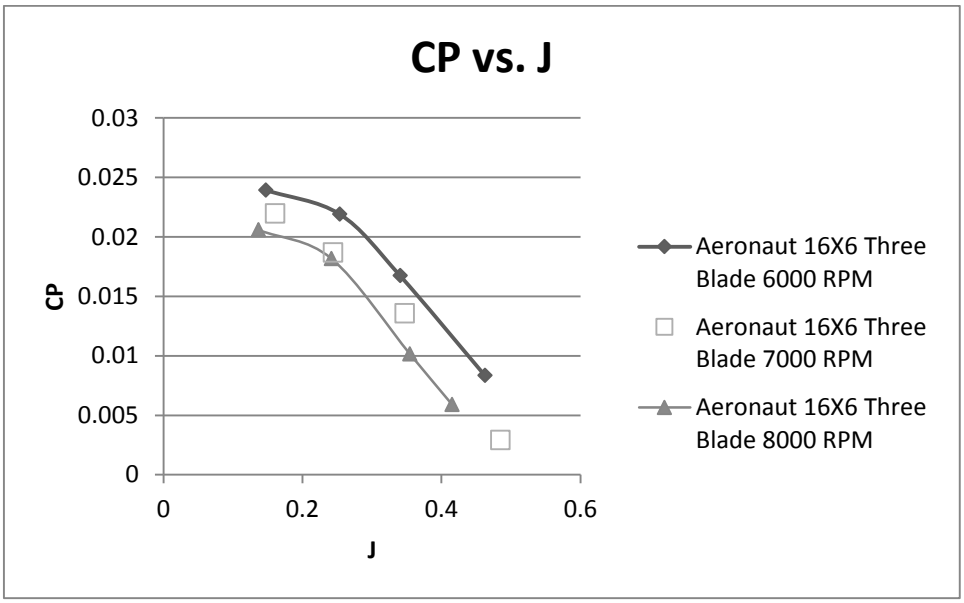

Figure 70- Aeronaut 16×6 three blade coefficient of power vs. advance ratio results

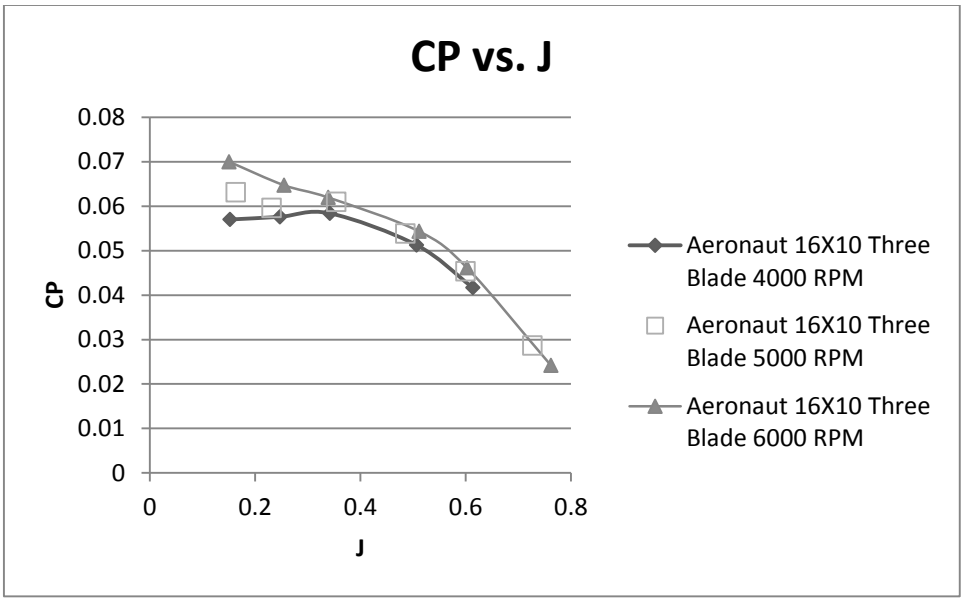

Figure 71- Aeronaut 16×10 three blade coefficient of power vs. advance ratio results

7.4.1.3 MASTER AIRSCREW THREE BLADE

Figure 72- Master Airscrew 16×8 three blade propeller top view

The Master Airscrew is another propeller designed for model airplanes. The propeller tested has three blades that do not fold as seen in Figure 72. The dimensions are 16×8 just like the baseline propeller. Figure 73 shows the efficiency is increasing with RPM unlike what was seen with the Aeronaut brand propellers. The Master Airscrew efficiency does not have a maximum as high as the baseline propeller but these results show with an increase in RPM it may be possible.

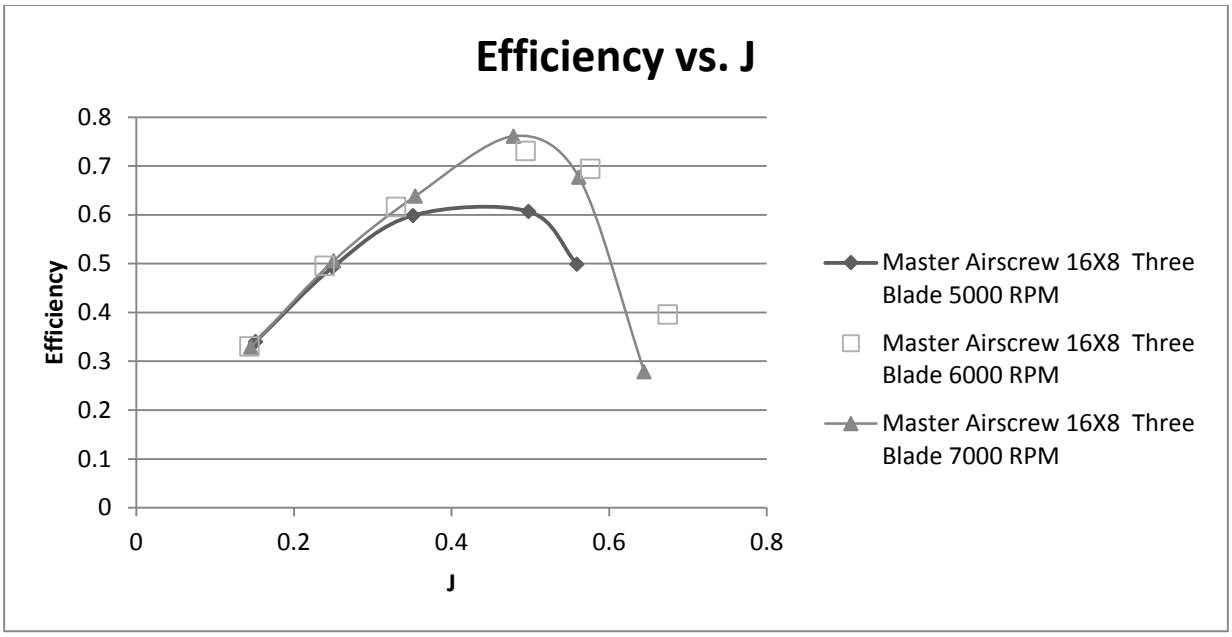

Figure 73- Master Airscrew 16×8 three blade efficiency vs. advance ratio result

Figure 74 shows the coefficient of thrust may be increasing with RPM. It is important to note because if this trend is true, the Master Airscrew 16×8 propeller actually may produce a greater coefficient of thrust at a lower RPM. Figure 75shows a comparison of the Master Airscrew and the baseline propeller. For all of the data points the Master Airscrew coefficients of thrust values are higher than the baseline but again within the uncertainty bounds the performance is equivalent to the baseline.

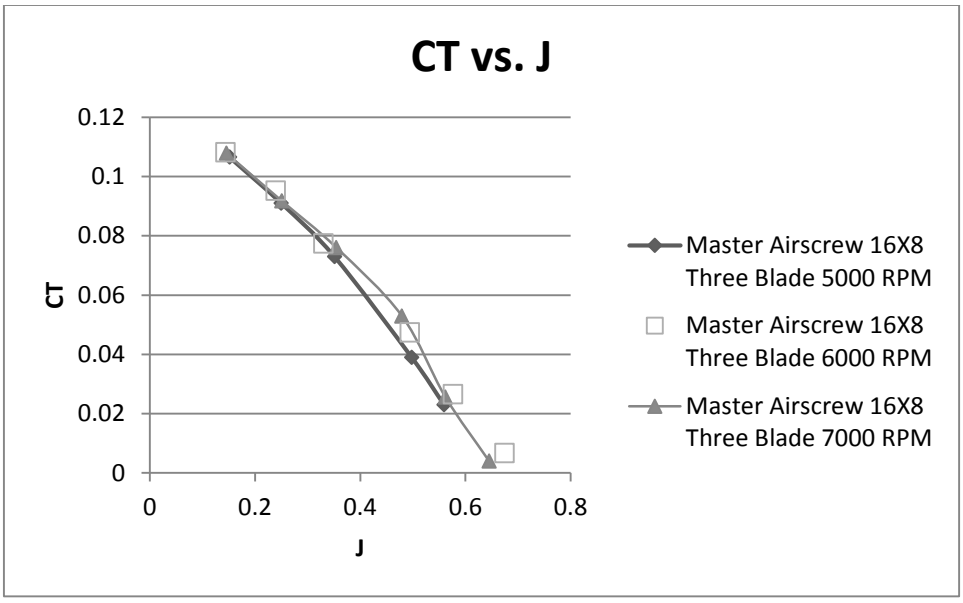

Figure 74- Master Airscrew 16×8 three blade coefficient of thrust vs. advance ratio result

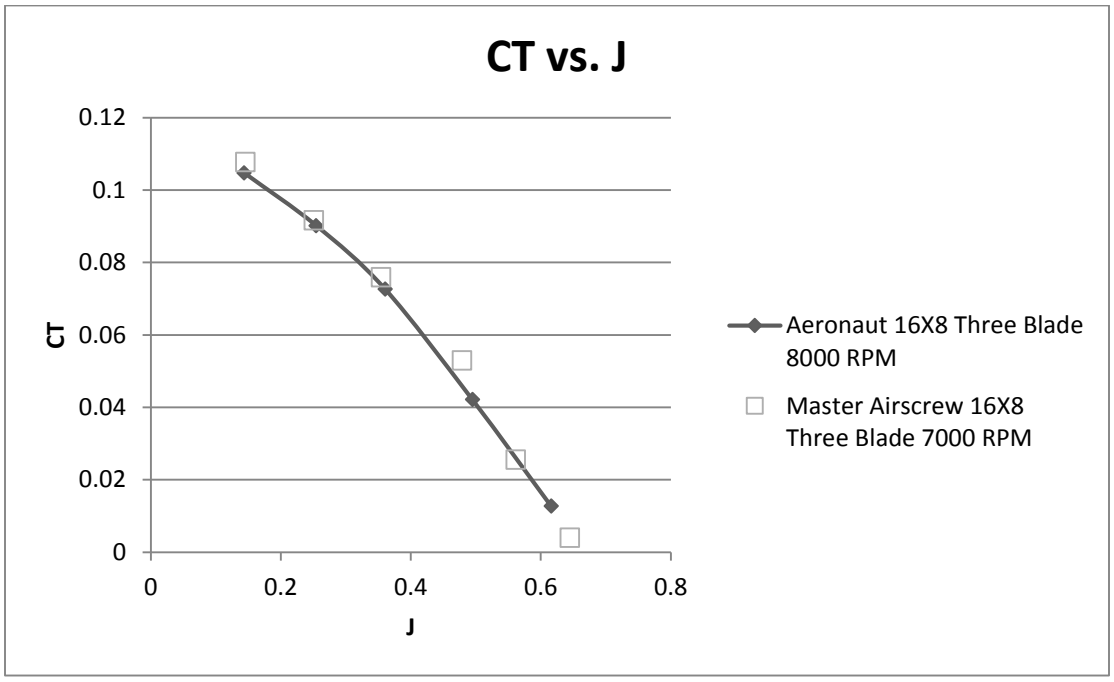

Figure 75- Master Airscrew compared to baseline Aeronaut 16×8

Figure 76 shows the Master Airscrew coefficient of power results plotted over the baseline. Results appear to be similar in magnitude for each coefficient of power particularly when considering uncertainty bounds. The Aeronaut cases for 8,000 RPM does have the lowest coefficients of power but at this RPM the coefficient of thrust is also lower.

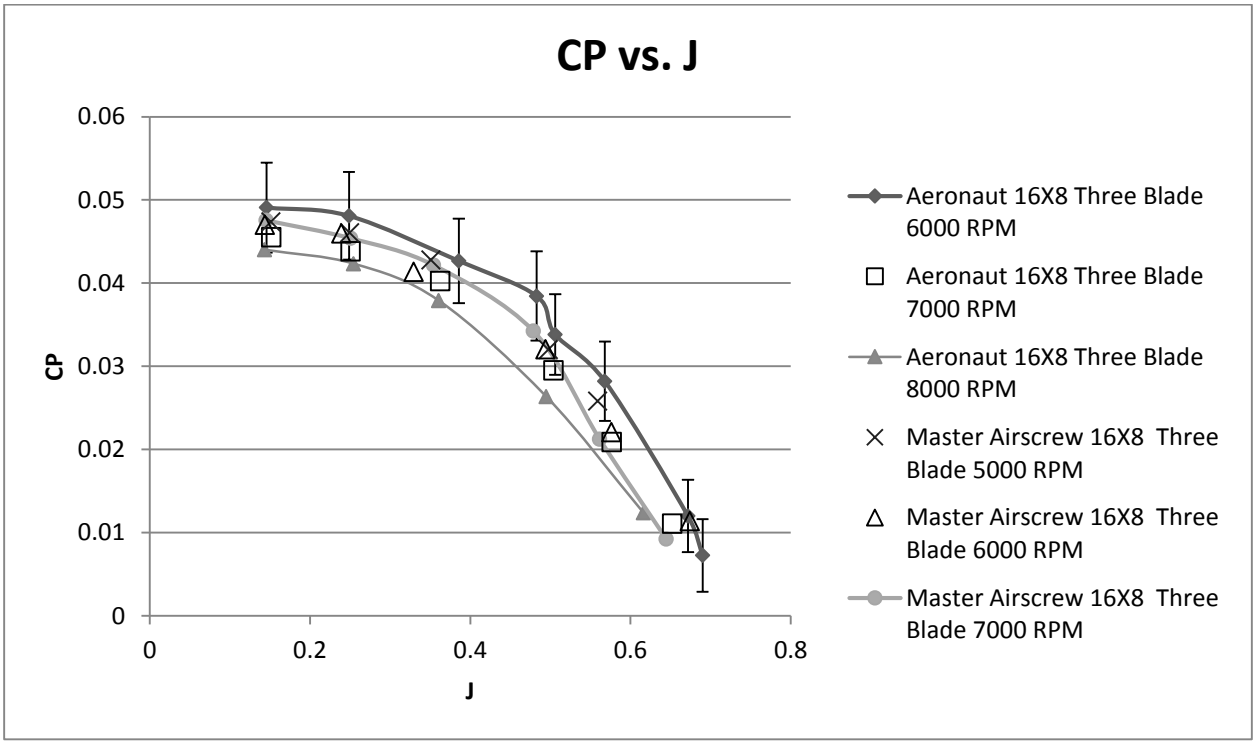

Figure 76- Master Airscrew coefficient of power vs. advance ratio results plotted with Aeronaut 16×8

7.4.1.4 VESS PROPELLERS

Figure 77- Vess 16×6, 8 two blade propeller top view

Two Vess brand propellers were selected based on their advertisement of having a low acoustic noise signature. The two propellers tested were the 16×6 and 16×8 which are shown in Figure 77. Both propellers had two blades that did not fold. From Figure 78, it can be seen that the Vess 16×8 propeller is more efficient, but at greater velocities. Since the efficiency curve of the 16×8 propeller follows the 16×6 curve, the results show it would be better to use the Vess 16×8 propeller. Also, the maximum of the Vess 16×8 propeller is close to the baseline maximum.

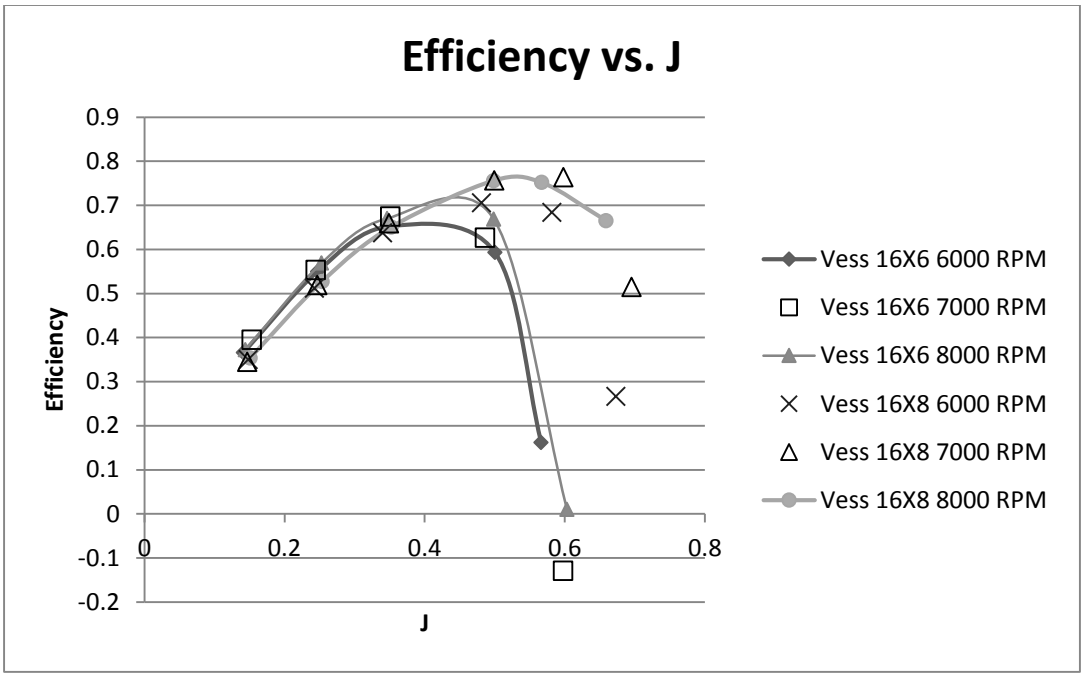

Figure 78-Vess 16×6 and 16×8 efficiency vs. advance ratio results

Figure 79 shows the increase in pitch did increase the coefficient in thrust. The maximum coefficient of thrust is still lower than the baseline. However, based on the trends found in the Vess results the RPM could be increased to match the baseline propeller. For the current GL-10 motor the limit is 8,000 RPM so this is not feasible. The acoustic noise signature also increases with RPM.[25]

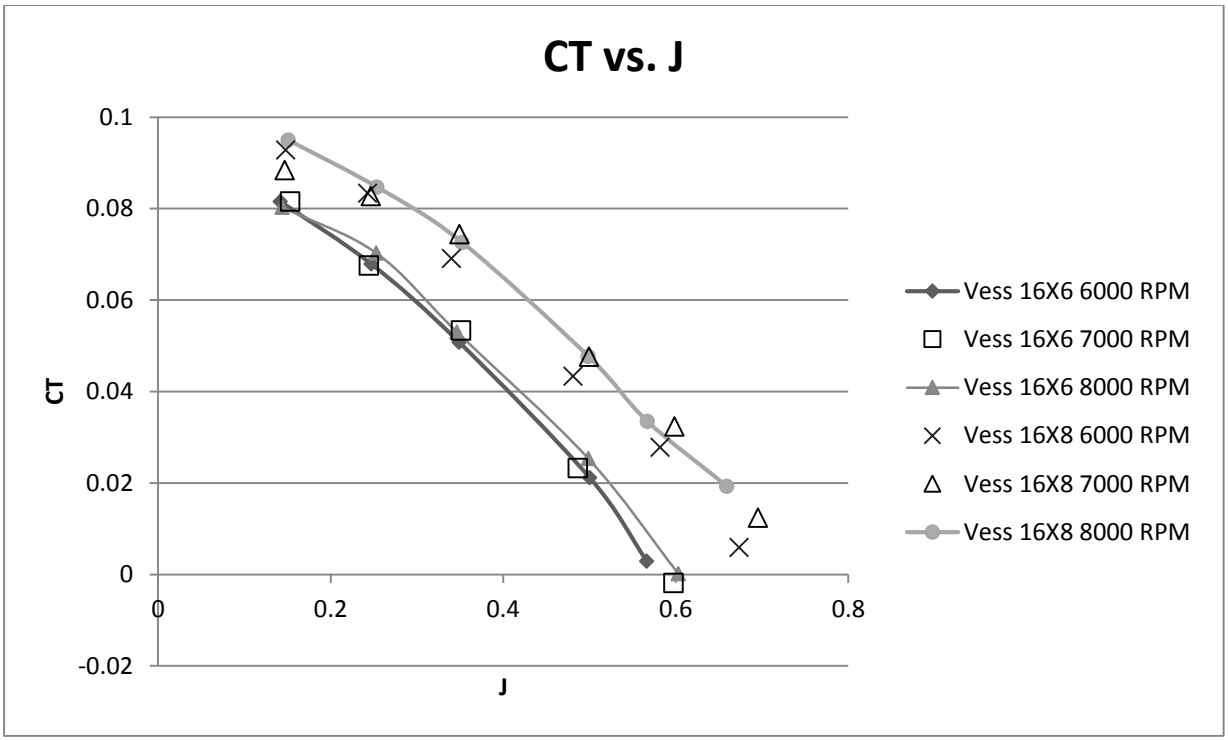

Figure 79- Vess 16×6 and 16×8 coefficient of thrust vs. advance ratio results

Figure 80 shows the two Vess propellers compared with the baseline for coefficient of power vs. advance ratio. The coefficient of power for the Vess 16×6 propeller is visibly below the baseline. As in the case of the Master Airscrew, the Vess 16×8 is almost completely overlapped by the baseline except for a few curves.

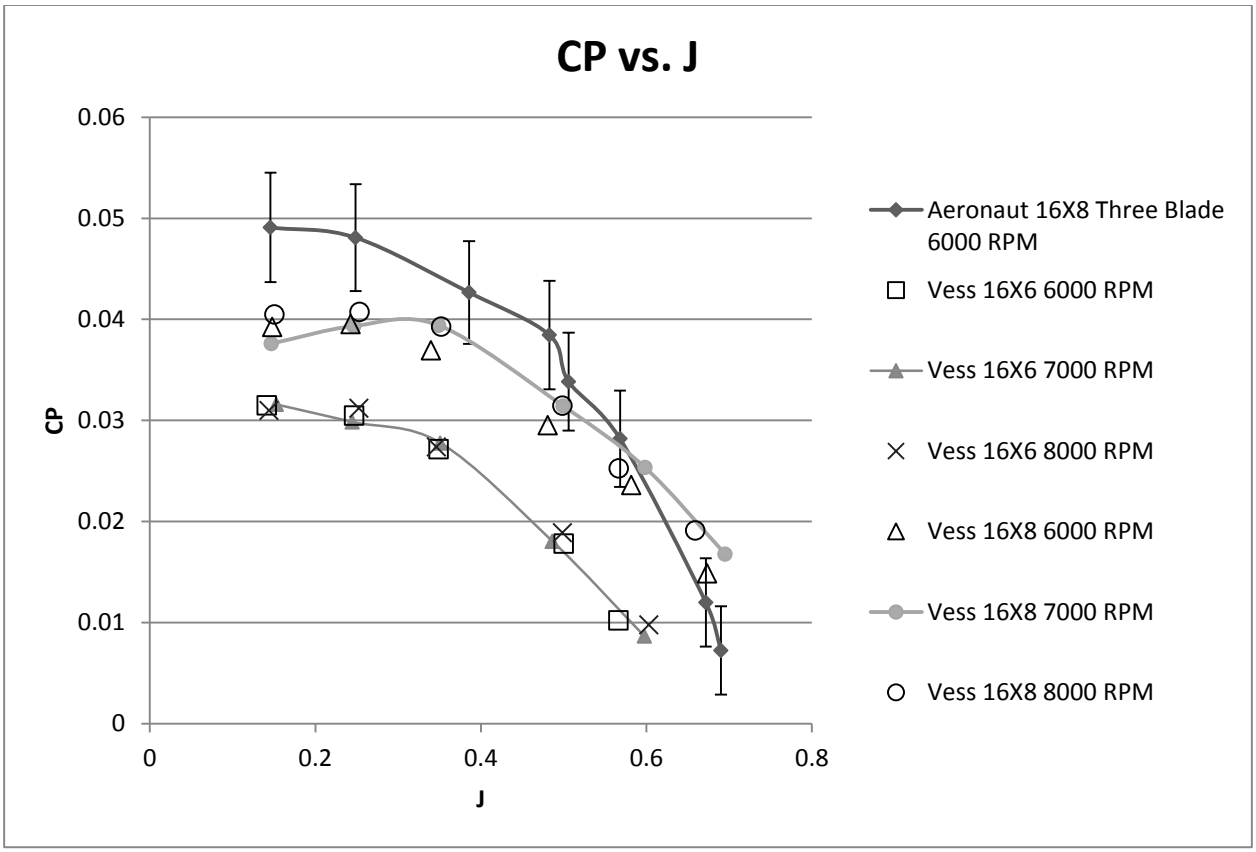

Figure 80- Vess 16×6 and 16×8 coefficient of power vs. advance ratio results compared to Aeronaut 16×8

7.4.2 ACOUSTICS

Before performing acoustic data collection on the candidate propellers, the performance data were analyzed to determine if a candidate propeller met the performance requirements for the project. From the GL-10 candidate propeller performance analysis shown previously, it was found the Aeronaut 16×6 two and three blade propeller, Aeronaut 16×8 two blade propeller, and the Vess 16×6 propeller did not meet the necessary performance requirements. The performance results showed the thrust was either not achieved or that the thrust was achieved but at an excessive RPM. The propellers that met the thrust requirements at lower RPM were analyzed.

The selected candidate propellers are the Aeronaut 16×10 two and three blade, Master Airscrew 16×8 three blade, and the Vess 16×8 two blade.

7.4.2.1 AERONAUT 16×10 TWO BLADE

Results for the Aeronaut 16×10 two blade propeller in Figure 81 show the 16×10 propeller is approximately 10 dB higher than the baseline. Since this is only a two blade propeller, the RPM required to meet minimum thrust was higher than the baseline. The increase in tip speed is seen in the increase in noise. The static efficiency has also decreased by 0.15, also due to the increase in RPM. Increasing the RPM increases the torque in the denominator of the static efficiency equation and reduces the efficiency.

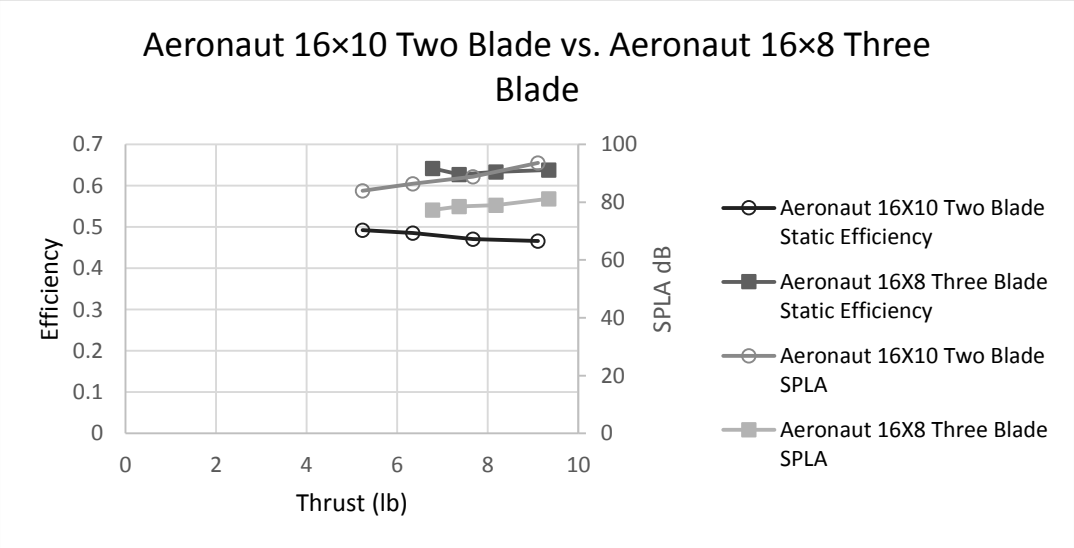

Figure 81- Comparison of Aeronaut 16×10 two blade to Aeronaut 16×8 three blade for acoustic noise

7.4.2.2 AERONAUT 16×10 THREE BLADE

Results for the Aeronaut 16×10 three blade case are shown in Figure 82 and appear to be trending in the wrong direction from the baseline as well. There is a static efficiency difference of 0.19 for the worst case. There is also still a difference in the noise production. Compared to the two blade 16×10 propeller, the acoustic noise has dropped to a 5 dB difference instead of 10 dB.

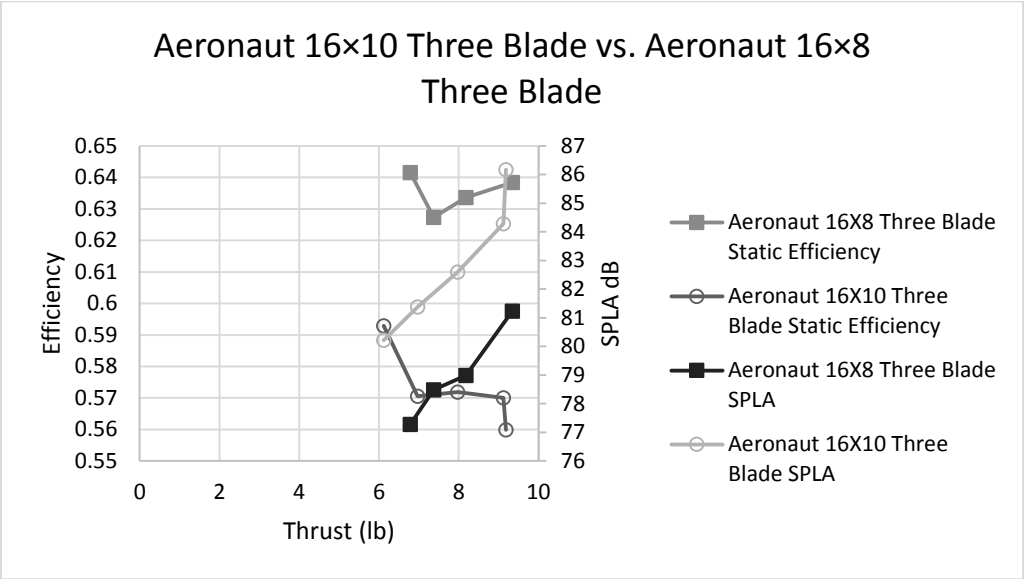

Figure 82- Comparison of Aeronaut 16×10 three blade to Aeronaut 16×8 three blade for acoustic noise

7.4.2.3 MASTER AIRSCREW 16×8 THREE BLADE

Results of the Master Airscrew 16×8 propeller versus the baseline in Figure 83 show the acoustic noise is equivalent at higher thrust values. Even at the lower thrust values there is only a half dB difference in the measurement. There is still a maximum difference in static efficiency of 0.05 at the largest difference.

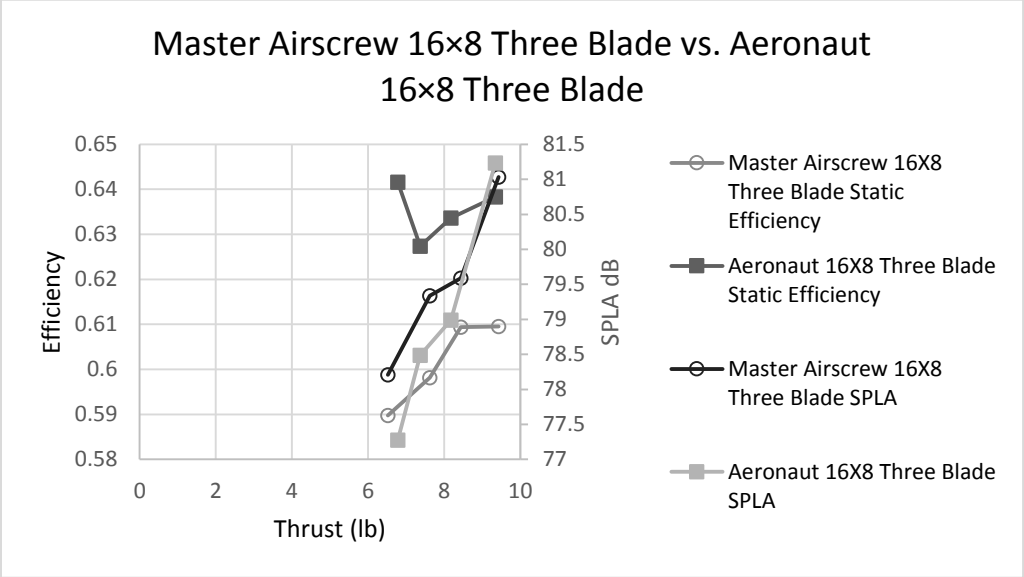

Figure 83- Comparison of Master Airscrew three blade to Aeronaut 16×8 three blade for acoustic noise

Due to the close comparison to the baseline for the wind tunnel data, anechoic chamber results were shown for the Master Airscrew as well. Figure 84 shows the anechoic noise data have small differences when comparing noise readings at the appropriate angle. At the 45 degree microphone placement there is approximately a five decibel difference between the Master

Airscrew and baseline. Similar differences followed when comparing the noise for the 0 and 22.5 degree microphone placements.

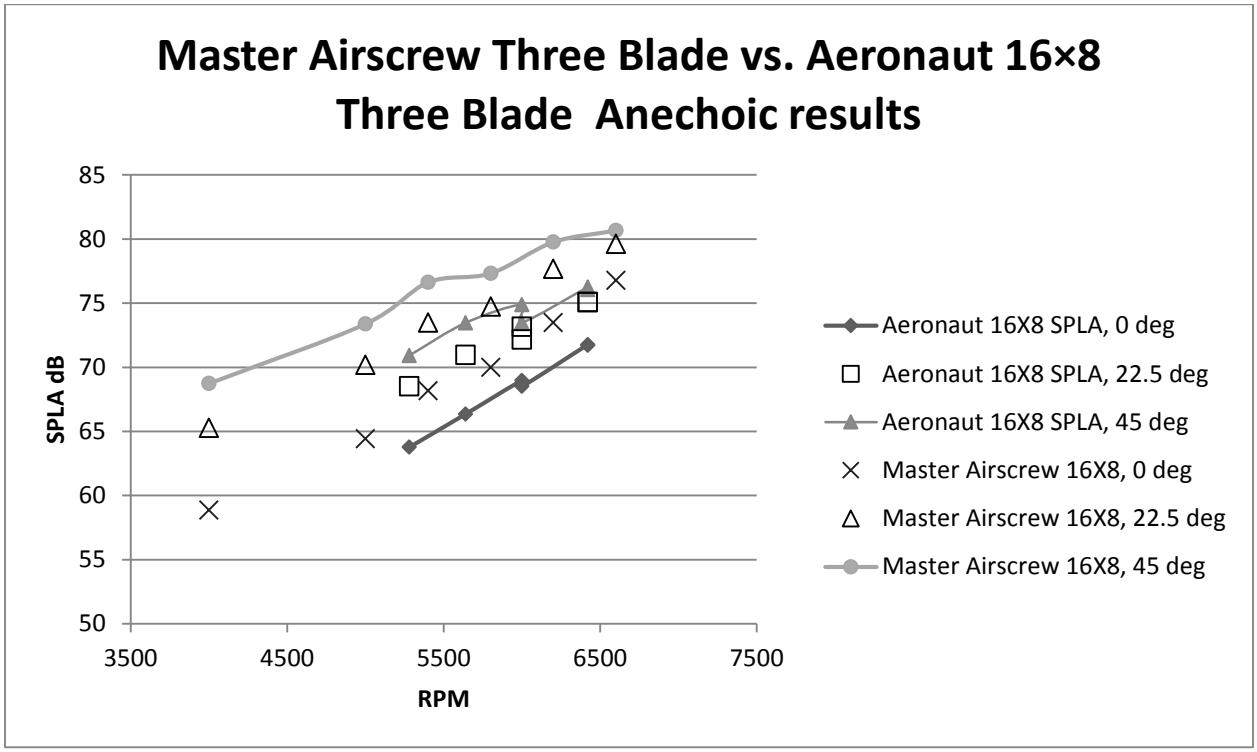

Figure 84- Comparison of Master Airscrew 16×8 and Aeronaut 16×8 with anechoic chamber results

7.4.2.4 VESS 16×8 TWO BLADE

The Vess 16×8 propeller results actually show desired trends compared to other candidate propellers. Figure 85 shows the static efficiency of the Vess propeller is greater than the baseline. Using the points located at 6.85lb, there is a difference of nearly 0.03. This difference then grows favorably with thrust or RPM. Also, the acoustic noise peaks at the same level as the baseline.

However, this is only for the maximum thrust of the Vess 16×8 and baseline. As the thrust for the Vess 16×8 propeller decreases, the difference between the baseline noise increases in an undesirable manner. The largest difference, which is at 6.85lb, is 4 dB. This is the lowest difference out of all the candidate propellers.

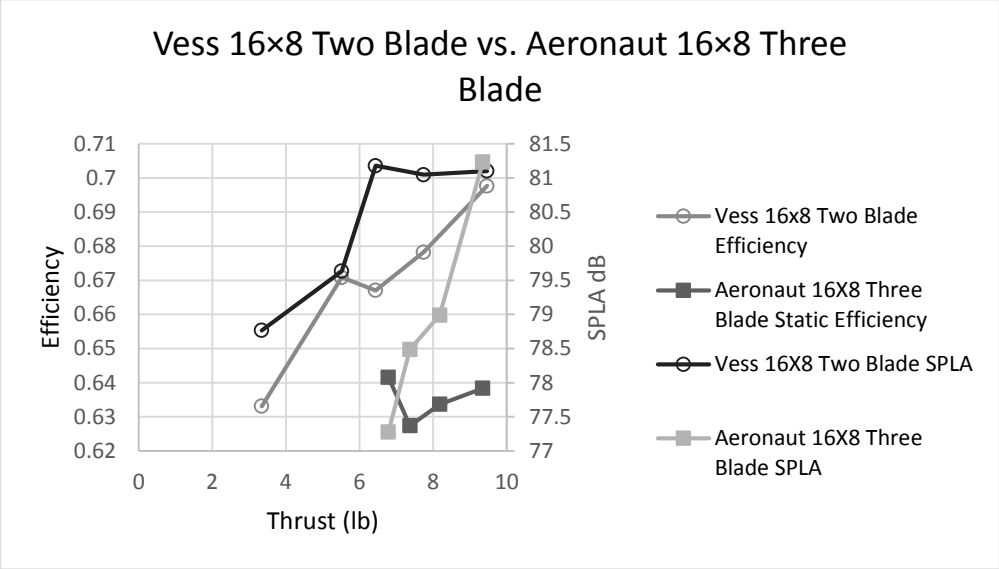

Figure 85- Comparison of Vess 16×8 two blade to Aeronaut 16×8 three blade for acoustic noise

7.5 GEORGIA TECH OPTIMIZED PROPELLER

7.5.1 PERFORMANCE

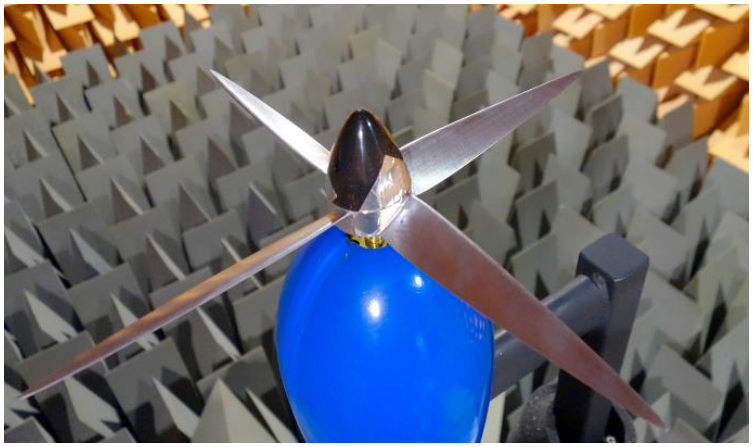

Figure 86- Georgia Tech four blade propeller

The optimized propeller from Georgia Tech(GT) is a four bladed propeller CNC machined from aluminum as seen in Figure 86. All four blades are fixed (do not fold). Figure 87 shows that the efficiency of the GT propeller is nominally less than the baseline. The results do show the GT propeller may perform better than the Aeronaut at faster flight speeds.

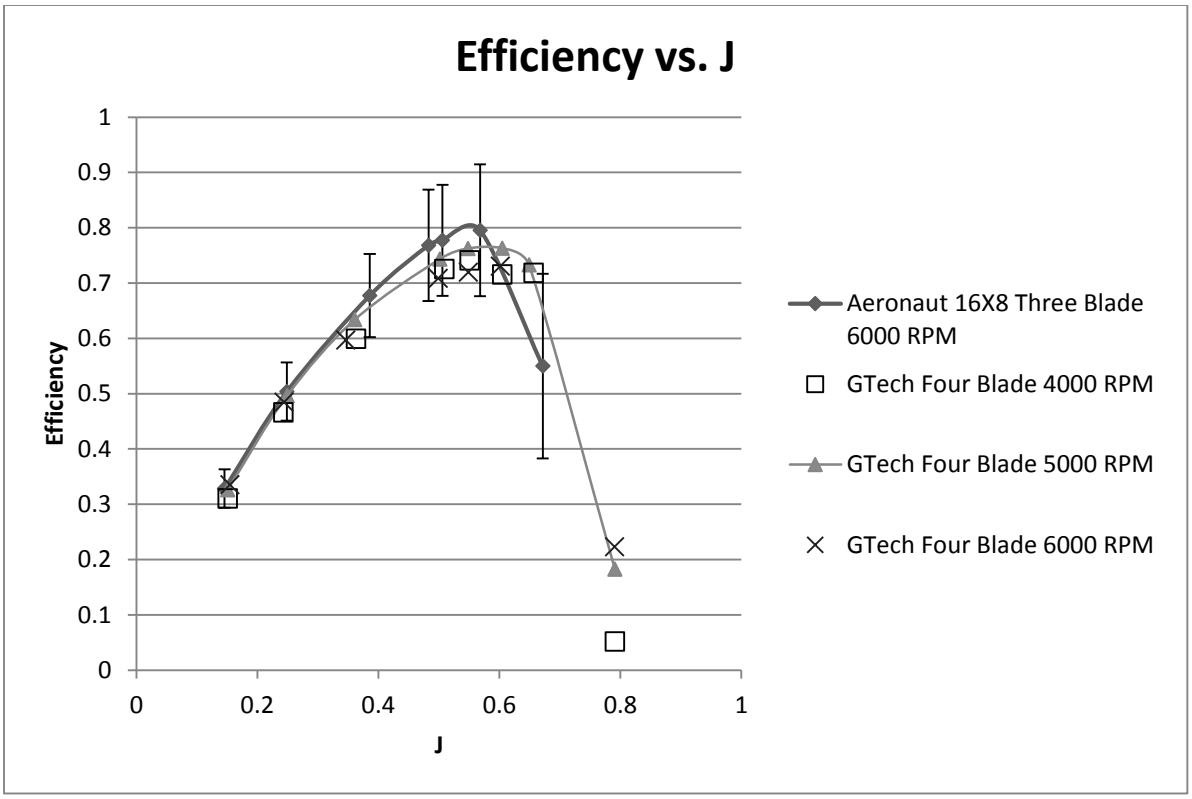

Figure 87- Georgia Tech propeller compared to Aeronaut baseline, efficiency vs. advance ratio

One of the design goals for the GT propeller was to increase thrust production at lower RPMs. Figure 88 shows this goal was met by comparing the coefficient of thrust vs. advance ratio for GT and Aeronaut propellers. There is a significant difference between the two groups. It should also be noted that the GT propeller was tested at a lower RPM compared to all the Aeronaut runs except for one. This increase in thrust is expected as the comparison is between four and three blades.

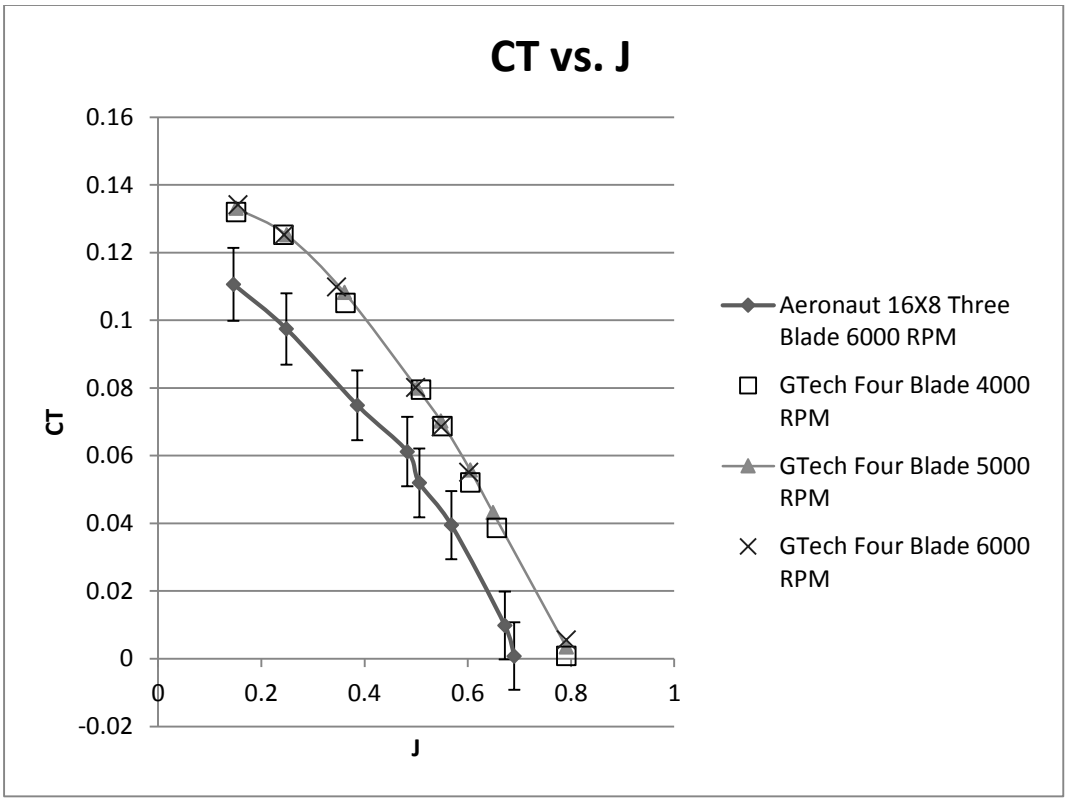

Figure 88- Georgia Tech propeller compared to Aeronaut baseline, coefficient of thrust vs. advance ratio

With this increase in coefficient of thrust comes a large power penalty as expected. Figure 89 shows the difference in the coefficient of power between the GT propeller and the baseline. This result shows a significant difference in the two curves. At the cruising speed of 44 knots and an RPM of 6,000 the advance ratio is 0.55. This difference in coefficient of power is approximately 0.015. This is the largest difference seen in any of the other tested propellers.

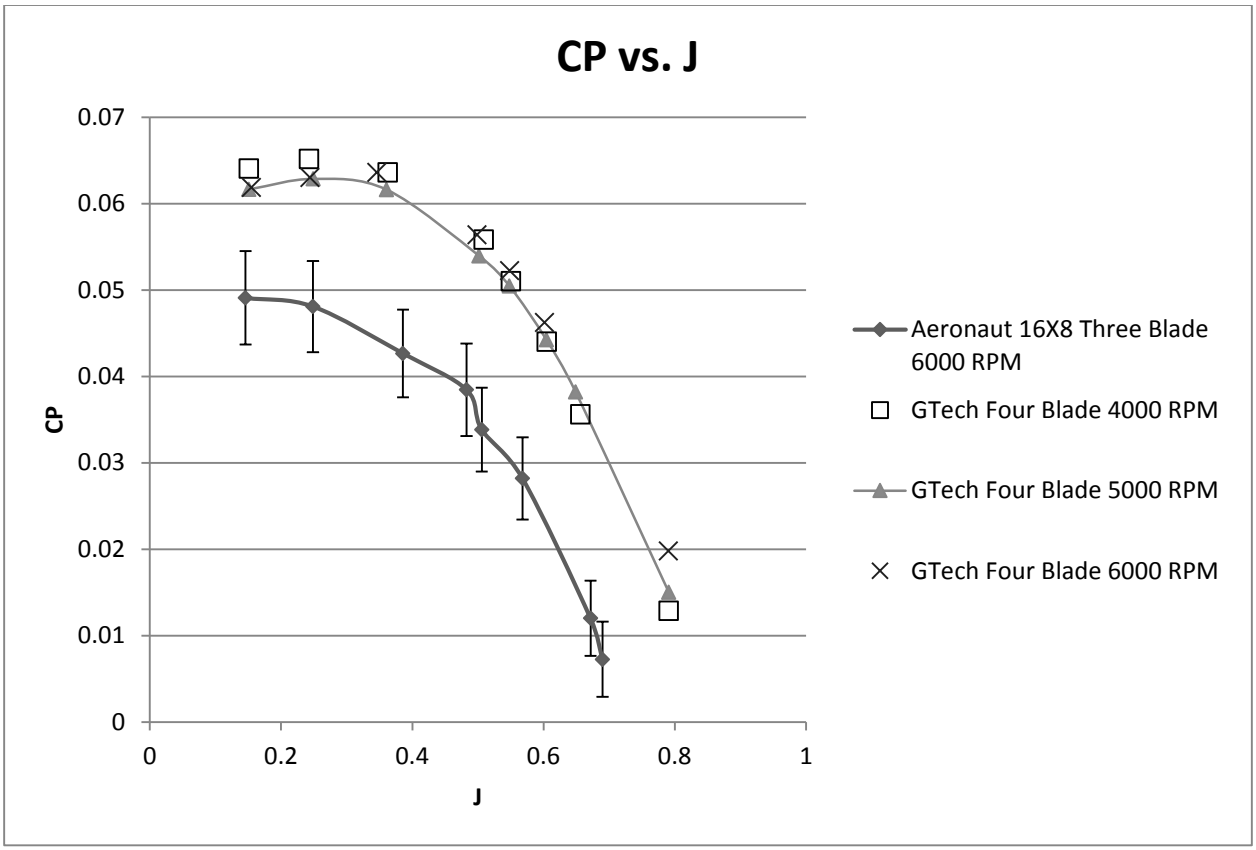

Figure 89- Georgia Tech propeller compared to Aeronaut baseline, coefficient of power vs. advance ratio

7.5.2 ACOUSTICS

The results for the GT propeller vs. the baseline showed some expected trends based on the increase from three to four blades. Figure 90 shows the static efficiency is lower than the baseline. Since the GT propeller requires more power with the higher blade count. This was shown in the performance section for the GT propeller.

The difference in noise between the GT propeller and the baseline is approximately two decibels at the peak thrust. However, near the static thrust goal this difference grows to four decibels and trends show this difference increasing.

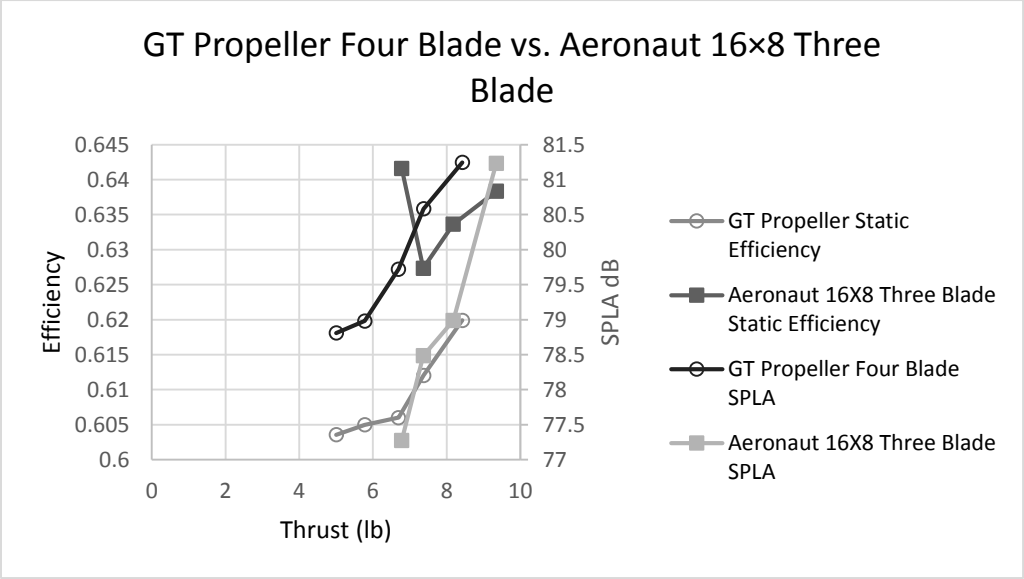

Figure 90- GT propeller compared to the Aeronaut 16×8 three blade for acoustic noise

The acoustic data collected at the anechoic chamber showed similar trends to the collected wind tunnel data. Figure 91 shows for all the microphone angles tested, the GT

propeller was louder than the baseline. The differences between the 0 and 45 degree measurements have approximately the same difference for both the GT and the Aeronaut 16×8 propellers.

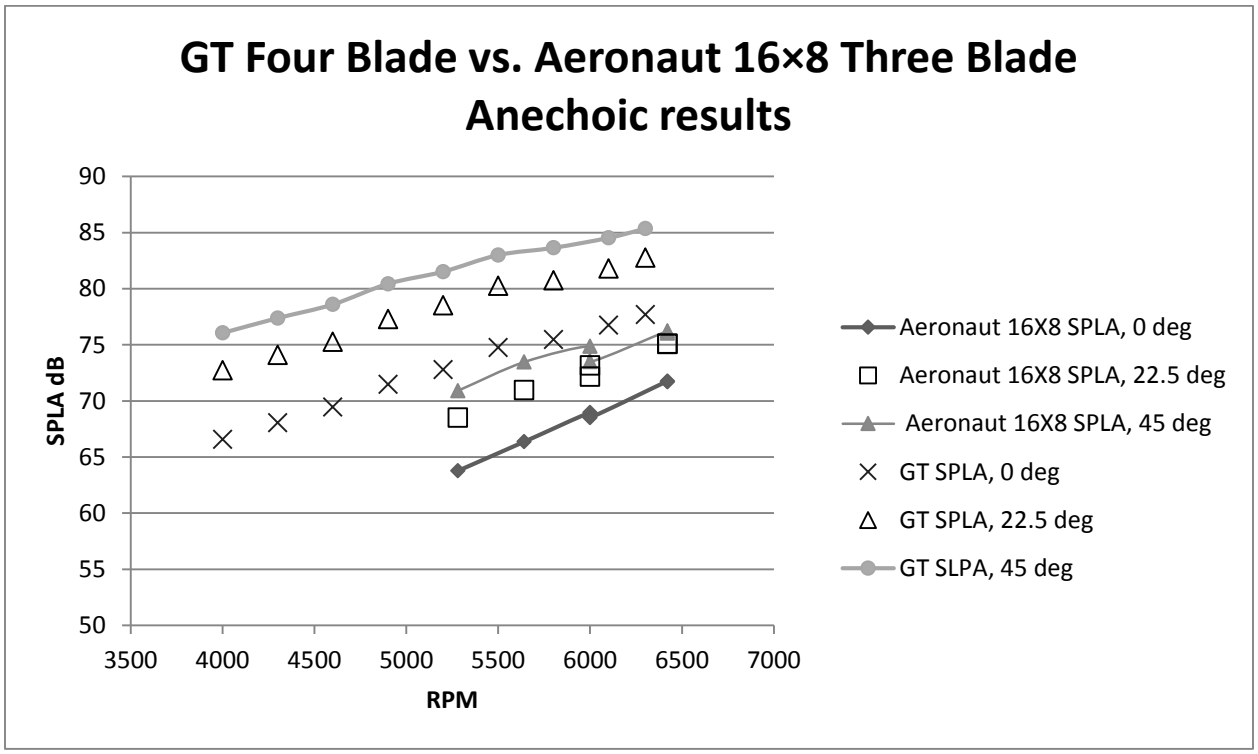

Figure 91- Comparison of GT propeller and Aeronaut 16×8 three blade with anechoic chamber results

CHAPTER 8 - CONCLUSIONS AND FUTURE WORK

The newly designed propeller test stand has been proven to function as desired. Selection and testing the implementation of each sensor was important to ensuring reliability and reducing uncertainty. The RPM sensor and servo controller were found to be reliable and accommodated the different propeller testing locations with minor problems. However, the performance from the load cell shows it could be improved. The results performed show a need for greater precision from the load cell. For some propellers tested at different RPMs the changes in coefficients were negligible. In comparison to the baseline propeller it can be seen some candidate propellers coefficient results did not vary enough to fall outside of the error bars. From this, results are lacking confidence to say for sure if the baseline propeller is truly performing better or worse than a candidate propeller. Using a load cell with a smaller loading range, other than the ATI 0-100lb range, would provide better results with greater accuracy. By having the appropriate loading range, the sensitivity, random, and systematic error would improve. The goal would be to reduce the confidence intervals for closer comparisons.

For acoustic data collection in the wind tunnel, more sophisticated microphone mounting hardware is needed. Due to resources, this project used a single microphone mounted in one location. Future designs may have the need to mount the microphone to a traverse system to allow it to be moved in a grid pattern. This allows for a greater understanding of how the angle to the propeller affects the noise level. This can also aid in studying how the acoustic reflections are formed from the walls of the wind tunnel. Using the traverse inside the wind tunnel (static testing) and at the anechoic chamber, data can then be compared and possible reflections can be seen. Future testing should address the uncertainty in acoustic measurements to better facilitate comparison testing.

Results were compared to the baseline by plotting the static efficiency, thrust, and A-weighted SPL in the same plot. This allowed for direct comparison of the performance data and acoustic data. The direct comparisons showed none of the propellers tested produced less acoustic noise then the baseline. However, the propeller that was the closest to the baseline was the Master Airscrew 16×8 three blade. The wind tunnel acoustic data comparison shows approximately half a decibel difference. The difference in static efficiency was also the smallest at 0.05. In comparisons with the Aeronaut 16×10 to the baseline, the static efficiency difference is almost two. The next best acoustically performing propeller was the GT propeller with a difference of four decibels. The static efficiency difference was only 0.04 at the largest difference. The problem with GT propeller was seen in the performance data for the coefficient of power plots. Since the GT propeller is four bladed, significantly more power is used compared to the baseline. Further revisions should study a reduction in a propeller blade count and possibly decreasing the pitch until the minimum performance conditions are met.

Based on these results the future designs are being lead to propellers with less pitch and more blades to reduce the RPM. The performance results of the GT propeller showed this. At lower RPM, the GT propeller was producing more thrust then the base line. This was also seen in the comparisons of the two blade propellers to the baseline.

The analysis did shown the current GL-10 propeller, the Aeronaut 16×8, produces the least amount of acoustic noise out of the propellers tested that met performance requirements. However, the experiments also gave insight to performance problems. For the baseline Aeronaut propeller as well as all the Aeronaut brand propellers tested the thrust decreased with RPM with the same trend for other coefficients. This is still not fully understood as to why it happens since it does not happen to any other propeller tested. One possible explanation stems from the fact

that the Aeronaut propellers can fold when not in use. This folding mechanism can then distort the propeller as the RPM is increased, hence reducing thrust, which reduces power output. These reductions then carry into the efficiency. To add to this, during testing with brand new Aeronaut propeller blades, there were two instances of structural failure. Failure was in the same location near the hub in both cases. With this, there is still room for improvement even though the Aeronaut 16×8 was found to be the quietest propeller.

REFERENCES

1. Yechout, T.R., S.L. Morris, D.E. Bossert, W.F. Hallgren, and J.K. Hall, *Introduction to Aircraft Flight Mechanics*. Second ed. 2014: American Institute of Aeronautics and Astronautics.
2. Brezina, A.J. and S.K. Thomas, *Measurement of Static and Dynamic Performance Characteristics of Electric Propulsion Systems.* AIAA, 2013 DOI: 10.2514/6.2013-500.
3. Brandt, J.B. and M.S. Selig, *Propeller Performance Data at Low Reynolds Numbers.* AIAA, 2011 DOI: 10.2514/6.2011-1255.
4. Merchant, M.P. and S.L. Miller, *Propeller Performance Measurment for Low Reynolds Number UAV Applications.* AIAA, 2006.
5. Selig, M.S., J.J. Guglielmo, A.P. Broern, and P. Giguere, *Summary of Low-Speed Airfoil Data*. Vol. 2. 1995, Virginia Beach,Virginia: SoarTech.
6. Marte, J.E. and D.W. Kurtz, *A Review of Aerodynamic Noise From Propellers Rotors, and Lift Fans.* 1970.
7. Gur, O. and A. Rosen, *Design of Quiet Propeller for an Electric Mini Unmanned Air Vehicle.* Journal of Propulsion and Power, 2009 DOI: 10.2514/1.38814: p. 717-728.
8. Roeser, R.J., M. Valente, and H. Hosford-Dunn, *Audiology Diagnosis*. 2nd ed. 2007: Thieme. 616.
9. Stuart, R., *Signals and Systems for Speech and Hearing*. 2011, BRILL. p. 163.
10. OL, M., C. Zeune, and M. Logan, *Analytical-Experimental Comparison for Small Electric Unmanned Air Vehicle Propellers.* AIAA, 2008 DOI: 10.2514/6.2008-7345.
11. Schlichting, H. and K. Gersten, *Boundary Layer Theory*. Eighth ed. 2000: Springer.

12. Barlow, J.B., H.R. William, Jr, and A. Pope, *Low-Speed Wind Tunnel Testing*. 1999, New York: Wiley.

13. H.Glauert, *The Elements of Aerofoil and Airscrew Theory*. 1983.

14. Wood, R.M. and R.G. Harris, *Some Notes on The Theory of an Airscrew Working in a Wind Channel.* Royal Aircraft Establishment, 1920.

15. Sebastian, S., H. Sebastian, K. Hyemin, S. Franz-Georg, and H. Mirko, *Development, Startup Operations and Tests of a Propeller Wind Tunnel Test Rig*, in *33rd AIAA Applied Aerodynamics Conference*. 2015, American Institute of Aeronautics and Astronautics.

16. Montgomery, D.C., *Design and Analysis of Experiments*. 8th ed. 2013: John Wiley and Sons,Inc.

17. Bell, W.A., W.L. Meyer, and B.T. Zinn, *Predicting the Acoustics of Arbitrarily Shaped Bodies Using an Integral Approach.* AIAA Journal, 1977 DOI: 10.2514/3.60712: p. 813-820.

18. Drela, M., *Xrotor User Guide*, M.I.o. Technology, Editor. 2003.

19. Holthusen, H. and H. Smit, *New Data Acquisition System for Microphone Array Measurements in Wind Tunnels*, in *7th AIAA/CEAS Aeroacoustics Conference and Exhibit*. 2001, American Institute of Aeronautics and Astronautics.

20. Coleman, H.W. and G.W. Steele, *Experimentation Validation, and Uncertainty Analysis for Engineers*. Third ed. 2009, Hoboken, New Jersey: John Wiley and Sons Inc.

21. Archer, R.D. and M. Saarlas, *Introduction to Aerospace Propulsion*. 1996, Upper Saddle River New Jersey: Prentice Hall.

22. McCormick, B.W., *Aerodynamics Aeronautics and Flight Mechanics*. Second ed. 1995, United States of America: John Wiley and Sons Inc.

23. Sho, S., D. Mark, L. Jeffrey, and O. David, *Design and Characterization of Hover Nano Air Vehicle Propulsion System*, in *27th AIAA Applied Aerodynamics Conference*. 2009, American Institute of Aeronautics and Astronautics.

24. *Advanced Precision Composites* Technical Information [cited 2016; Available from: https://www.apcprop.com/.

25. Bryce, H., G. Richard, and D.J. Jamey, *Optimal Propeller Design for Quiet Aircraft using Numerical Analysis*, in *21st AIAA/CEAS Aeroacoustics Conference*. 2015, American Institute of Aeronautics and Astronautics.

APPENDIX A

LABVIEW BACK PANEL ATI LOAD CELL INPUT

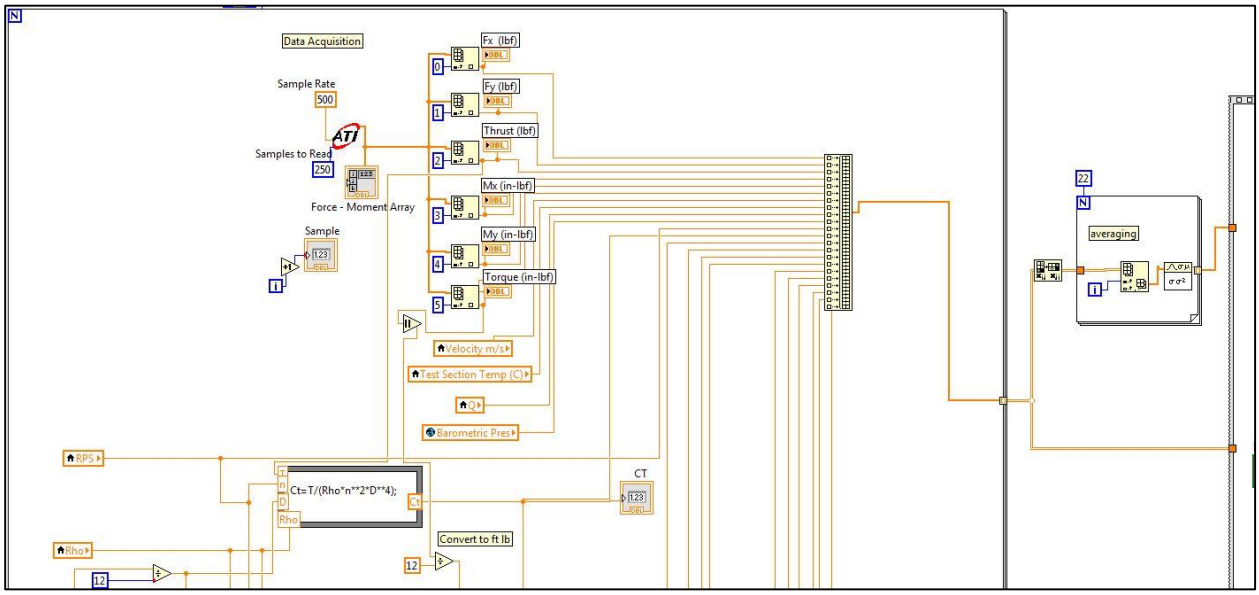

Figure 92- LabVIEW rear panel ATI load cell input

APPENDIX A.1

LABVIEW REAR PANEL SIGNAL INPUT OF RPM, VOLTAGE, AND CURRENT

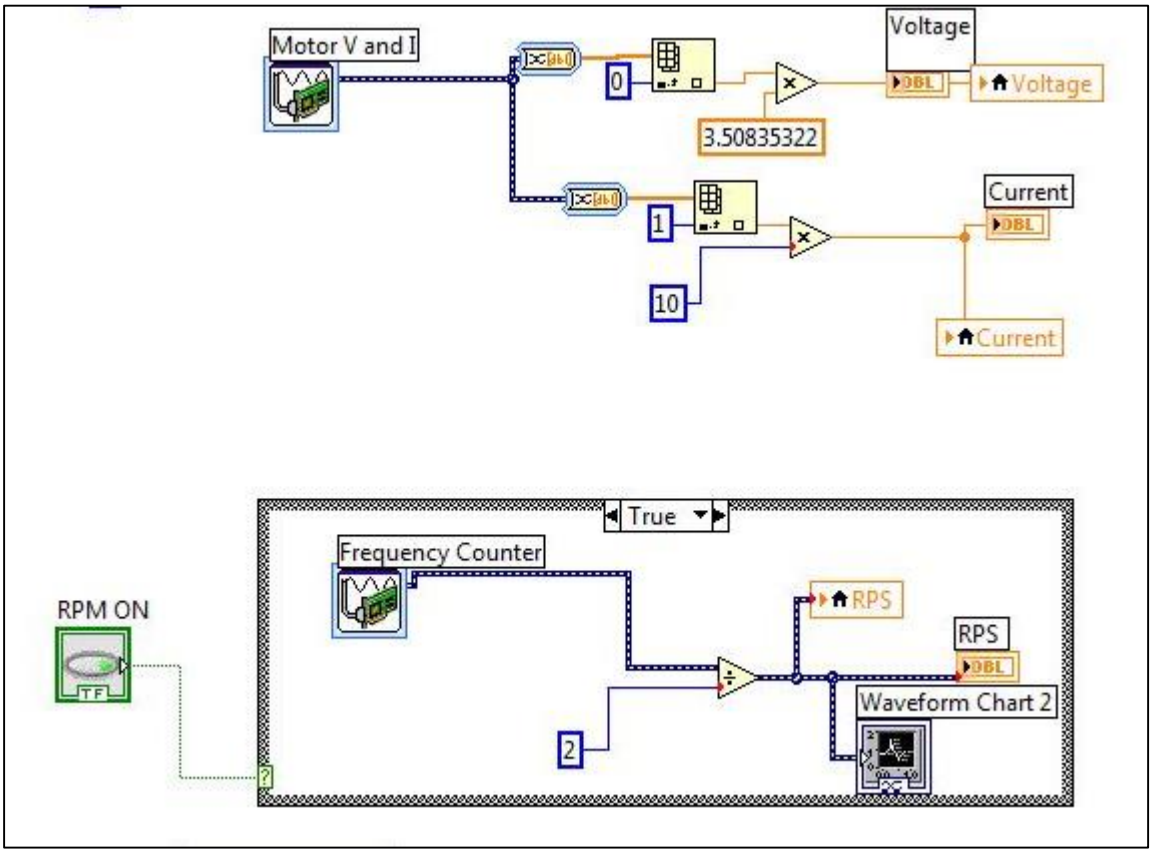

Figure 93- LabVIEW rear panel signal input of RPM, voltage, and current

APPENDIX A.2

LABVIEW REAR PANEL CALCULATIONS OF COEFFICIENTS

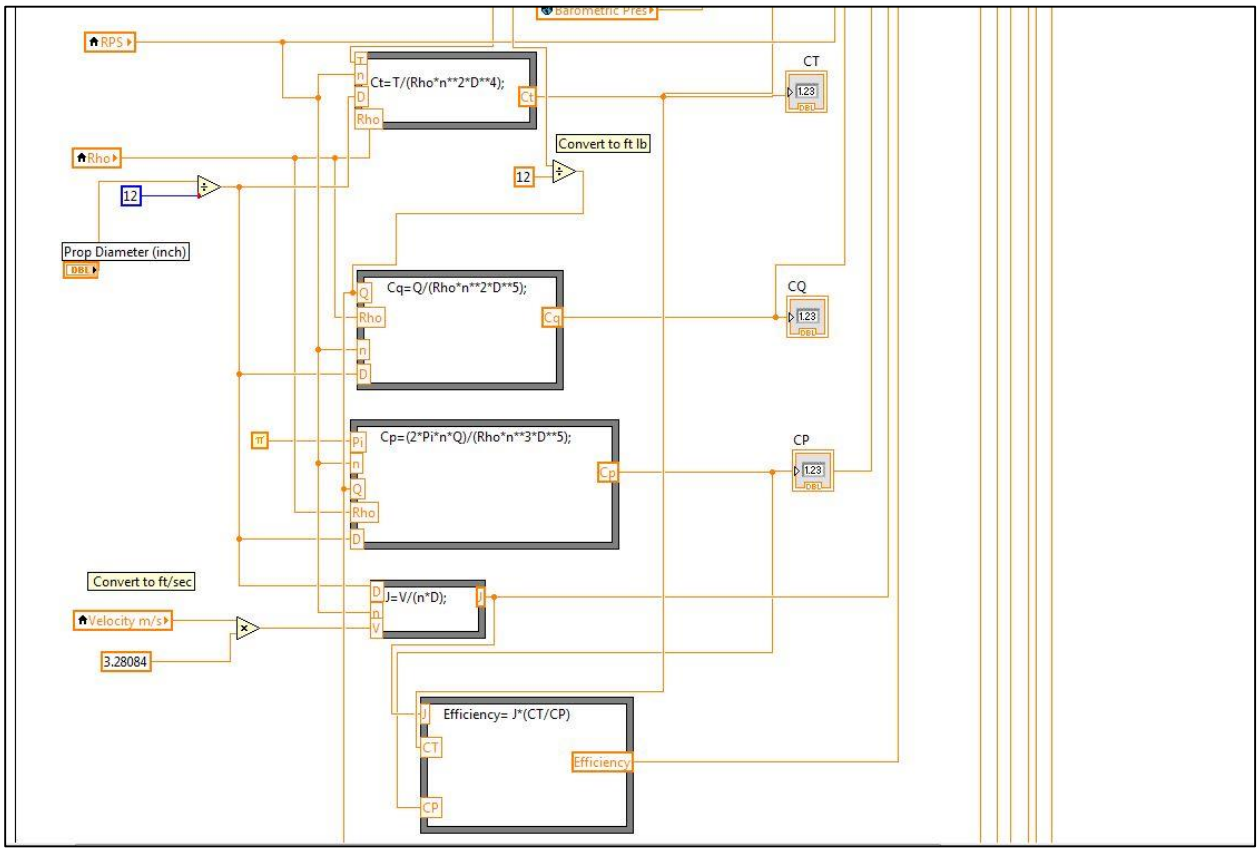

Figure 94- LabVIEW rear panel calculation of coefficients

APPENDIX B

RESULTS OF AERONAUT 16×8 3 BLADE PROPELLER

Wind Tunnel Performance Results

Aeronaut 16×8 Three Blade 7000 RPM															
Fz (lbf)	Mz (in-lb)	Velocity (m/s)	Temp (C)	q (Pa)	Baro P (pa)	RPS	CT	CQ	CP	J	Efficiency	Voltage	Current	Rho(slugs /ft^3)	Power Input (W)
10.32	-11.25	7.04	18.86	30.10	101992.00	114.18	0.1064	0.0072	0.0455	0.15	0.35	29.85	43.08	0.00236	1285.83
9.90	-11.77	12.09	17.83	89.26	101990.80	118.76	0.0938	0.0070	0.0438	0.25	0.54	29.86	48.44	0.00237	1446.29
7.51	-9.87	16.75	18.69	170.69	101991.98	113.64	0.0779	0.0064	0.0402	0.36	0.70	29.82	37.11	0.00236	1106.36
5.17	-7.86	24.27	18.97	358.12	101989.58	118.49	0.0494	0.0047	0.0295	0.50	0.84	29.82	28.50	0.00236	849.88
2.61	-5.31	27.13	19.45	446.52	101982.91	115.75	0.0262	0.0033	0.0209	0.58	0.72	29.90	18.29	0.00235	546.76
0.70	-2.86	30.94	19.65	580.41	101982.00	116.72	0.0069	0.0018	0.0111	0.65	0.41	29.91	10.06	0.00235	300.84
Aeronaut 16×8 Three Blade 6000 RPM															
Fz (lbf)	Mz (in-lb)	Velocity (m/s)	Temp (C)	q (Pa)	Baro P (pa)	RPS	CT	CQ	CP	J	Efficiency	Voltage	Current	Rho(slugs /ft^3)	Power Input (W)
8.48	-9.46	6.02	16.14	22.06	100928.00	103.37	0.1108	0.0077	0.0485	0.15	0.33	29.42	32.09	0.00236	944.10
7.41	-9.18	10.25	18.14	63.36	100929.27	107.25	0.0959	0.0074	0.0467	0.24	0.50	29.32	31.36	0.00234	919.37
5.98	-8.57	16.24	18.90	158.67	100930.40	109.09	0.0747	0.0067	0.0421	0.38	0.68	29.37	29.40	0.00233	863.45
4.87	-7.77	20.84	18.16	261.93	100931.89	108.01	0.0588	0.0059	0.0368	0.48	0.77	29.35	26.76	0.00234	785.47
4.63	-7.52	22.08	18.16	294.18	100933.58	111.06	0.0504	0.0051	0.0322	0.48	0.75	29.36	25.90	0.00234	760.46
3.85	-6.73	25.31	19.09	385.25	100934.71	115.12	0.0405	0.0044	0.0278	0.54	0.78	29.37	23.32	0.00233	684.93
2.51	-5.22	30.19	18.37	549.54	100936.27	117.18	0.0247	0.0032	0.0202	0.63	0.78	29.39	18.38	0.00234	540.30

Aeronaut 16×8 Three Blade 8000 RPM															
Fz (lbf)	Mz (in-lb)	Velocity (m/s)	Temp (C)	q (Pa)	Baro P (pa)	RPS	CT	CQ	CP	J	Efficiency	Voltage	Current	Rho(slugs /ft^3)	Power Input (W)
10.901	-11.656	6.896	20.518	28.751	101978.378	118.454	0.1048	0.0070	0.0440	0.143	0.341	29.851	46.901	0.00235	1400.016
9.612	-11.483	12.356	19.398	92.661	101976.000	119.637	0.0902	0.0067	0.0423	0.254	0.542	29.851	47.399	0.00236	1414.926
8.226	-10.924	18.092	20.300	198.026	101974.000	123.515	0.0727	0.0060	0.0379	0.360	0.691	29.784	45.550	0.00235	1356.661
5.581	-8.883	26.794	18.678	436.115	101976.000	133.279	0.0422	0.0042	0.0264	0.495	0.792	29.853	37.177	0.00236	1109.838
1.668	-4.137	33.260	19.467	669.079	101977.000	132.855	0.0127	0.0020	0.0124	0.616	0.633	29.842	15.940	0.00235	475.687

Acoustic Wind Tunnel Results

Aeronaut 16X8 Three Blade 11ms			Aeronaut 16X8 Three Blade 22ms		
RPM	Un- weighted dB	A-weighted dB	RPM	Un- weighted dB	A-weighted dB
4800	87.2574	80.3394	4800	96.8358	85.5842
5400	87.0189	77.8916	5400	96.6361	85.5983
6000	87.3988	78.7945	6000	96.421	85.5785
6600	93.999	81.4916	6600	97.4076	85.5257
7200	109.2683	91.6897	7200	101.685	87.0693

Aeronaut 16X8 Three Blade SPLA 0 m/s		
RPM	Un- weighted dB	A-weighted dB
5280	82.0222	77.2759
5640	89.7569	78.4857
6000	89.2761	78.9876
6420	95.3654	81.2329

Anechoic Chamber Acoustic Results

Aeronaut 16X8 Three Blade					
Nominal RPM	Actual RPM	SPL dB @ 0 deg	SPL dB @ 22.5 deg	SPL dB @45 deg	Thrust (lb)
5280	5271.1	63.78	68.52	70.91	6.479
5640	5569.3	66.36	70.96	73.47	7.331
6000	6041.0	68.97	73.16	74.88	8.550
6000	6009.5	68.51	72.16	73.49	8.491
6420	6440.7	71.76	75.09	76.24	9.793

Appendix B.1

RESULTS FROM THE MASTER AIRSCREW 16×8

Wind Tunnel Performance Results

Master Airscrew 16×8 Three Blade 5000 RPM															
Fz (lbf)	Mz (in-lb)	Velocity (m/s)	Temp (C)	q (Pa)	Baro P (pa)	RPS	CT	CQ	CP	J	Efficiency	Voltage	Current	Rho(slugs /ft^3)	Power Input (W)
5.573	-6.311	5.182	19.656	16.245	101587.000	85.933	0.1065	0.00754	0.0474	0.151	0.340	29.872	16.847	0.00235	503.262
4.625	-5.959	8.411	19.664	42.726	101587.000	83.458	0.0911	0.00733	0.0461	0.249	0.493	29.825	15.703	0.00234	468.344
3.636	-5.430	11.702	20.049	82.740	101587.000	82.020	0.0730	0.00681	0.0428	0.351	0.599	29.865	14.132	0.00234	422.048
1.890	-3.947	16.357	20.240	161.556	101588.378	80.877	0.0390	0.00509	0.0320	0.498	0.607	29.909	10.042	0.00234	300.352
1.180	-3.368	18.914	20.293	215.953	101588.089	83.218	0.0230	0.00411	0.0258	0.559	0.499	29.872	8.901	0.00234	265.885

Master Airscrew 16×8 Three Blade 6000 RPM															
Fz (lbf)	Mz (in-lb)	Velocity (m/s)	Temp (C)	q (Pa)	Baro P (pa)	RPS	CT	CQ	CP	J	Efficiency	Voltage	Current	Rho(slugs /ft^3)	Power Input (W)
7.808	-8.638	5.799	19.262	20.337	101575.489	102.870	0.1082	0.0075	0.0470	0.144	0.330	29.808	26.666	0.00235	794.865
7.796	-9.579	10.297	20.100	63.944	101578.378	109.629	0.0953	0.0073	0.0460	0.239	0.495	29.883	32.877	0.00234	982.472
6.077	-8.282	13.941	19.653	117.574	101580.289	109.228	0.0774	0.0066	0.0414	0.330	0.616	29.789	26.624	0.00235	793.080
3.922	-6.748	21.238	18.809	273.660	101580.000	107.550	0.0475	0.0051	0.0321	0.494	0.731	29.824	21.385	0.00235	637.780
2.090	-4.419	24.289	19.476	356.544	101579.756	107.195	0.0266	0.0035	0.0221	0.576	0.694	29.897	13.028	0.00235	389.493
0.493	-2.137	27.302	19.198	451.645	101579.444	99.628	0.0067	0.0018	0.0114	0.674	0.396	29.923	6.294	0.00235	188.326

Master Airscrew 16×8 Three Blade 7000 RPM															
Fz (lbf)	Mz (in-lb)	Velocity (m/s)	Temp (C)	q (Pa)	Baro P (pa)	RPS	CT	CQ	CP	J	Efficiency	Voltage	Current	Rho(slugs /ft^3)	Power Input (W)
10.698	-12.015	6.880	19.536	28.607	101580.289	120.250	0.1078	0.00757	0.0476	0.145	0.329	29.853	47.515	0.00234	1418.485
8.920	-11.244	11.673	17.316	83.107	101581.000	117.190	0.0917	0.00723	0.0454	0.251	0.506	29.826	45.779	0.00237	1365.387
7.586	-10.715	16.738	18.587	169.842	101581.044	118.050	0.0760	0.00671	0.0422	0.354	0.639	29.857	43.234	0.00235	1290.843
5.385	-8.861	22.791	19.589	313.805	101582.000	117.128	0.0530	0.00545	0.0342	0.479	0.761	29.853	34.501	0.00234	1029.941
2.865	-6.049	28.386	18.902	487.976	101583.000	130.892	0.0256	0.00338	0.0212	0.562	0.677	29.830	21.194	0.00235	632.213
0.433	-2.544	32.107	20.080	621.755	101583.000	128.642	0.0040	0.00147	0.0092	0.645	0.279	29.837	8.353	0.00234	249.237

Acoustic Wind Tunnel Results

Master Airscrew 16X8 Three Blade 11ms			Master Airscrew 16X8 Three Blade 22ms		
RPM	A-weighted dB	Un- weighted dB	RPM	A-weighted dB	Un- weighted dB
4800	88.7162	81.1437	4800	96.4514	85.6534
5400	91.3442	80.4964	5400	96.5759	85.1898
6000	89.7536	80.0949	6000	96.0968	85.1462
6600	95.2484	81.2216	6600	98.4411	86.0678
6900	115.8569	97.5224	7200	104.2371	88.8739

Master Airscrew 16X8 Three Blade SPLA 0 m/s		
RPM	Un- weighted dB	A-weighted dB
5280	83.8906	78.2075
5640	90.3345	79.3366
6000	87.954	79.5902
6420	93.0003	81.0338

Anechoic Chamber Acoustic Results

Master Airscrew 16X8 Three Blade					
Nominal RPM	Actual RPM	SPL dB @ 0 deg	SPL dB @ 22.5 deg	SPL dB @ 45 deg	Thrust (lb)
4000	4092.544162	58.85545884	65.26456883	68.7406823	4.282811945
5000	5071.020442	64.4360382	70.18778028	73.38685244	6.651648495
5400	5427.862541	68.1664218	73.47551652	76.62899539	7.79569531
5800	5824.438195	69.99041752	74.72045615	77.32772027	8.79794637
6200	6171.305623	73.475301	77.68222008	79.7610112	10.0241729
6600	6601.833518	76.78718131	79.62419338	80.6661269	11.60003001

APPENDIX B.2

RESULTS FROM THE GEORGIA TECH 16×8

GTech Four Blade 4000 RPM															
Fz (lbf)	Mz (in-lb)	Velocity (m/s)	Temp (C)	q (Pa)	Baro P (pa)	RPS	CT	CQ	CP	J	Efficiency	Voltage	Current	Rho(slugs /ft^3)	Power Input (W)
4.268	-5.274	4.060	20.162	9.900	101200.000	66.254	0.132	0.01020	0.06406	0.151	0.311	30.803	10.589	0.00233	326.180
4.009	-5.311	6.499	20.053	25.380	101199.067	65.895	0.125	0.01038	0.06519	0.243	0.466	30.867	10.670	0.00233	329.345
3.398	-5.238	9.765	19.971	57.319	101199.978	66.229	0.105	0.01013	0.06363	0.363	0.600	30.851	10.415	0.00233	321.303
2.608	-4.664	13.805	19.967	114.551	101200.000	66.719	0.080	0.00889	0.05583	0.509	0.725	30.865	9.313	0.00233	287.437
2.201	-4.163	14.746	19.224	130.839	101200.422	65.900	0.069	0.00812	0.05102	0.551	0.741	30.823	8.269	0.00234	254.886
1.674	-3.605	16.192	18.287	158.514	101200.000	65.865	0.052	0.00701	0.04402	0.605	0.715	30.797	7.059	0.00235	217.384
1.264	-2.963	17.770	20.258	189.621	101200.000	66.608	0.039	0.00567	0.03561	0.656	0.719	30.797	6.021	0.00233	185.443
0.027	-1.051	21.204	20.353	269.909	101200.000	65.978	0.001	0.00205	0.01288	0.791	0.052	30.853	2.469	0.00233	76.179

GTech Four Blade 5000 RPM															
Fz (lbf)	Mz (in-lb)	Velocity (m/s)	Temp (C)	q (Pa)	Baro P (pa)	RPS	CT	CQ	CP	J	Efficiency	Voltage	Current	Rho(slugs /ft^3)	Power Input (W)
6.764	-7.977	5.083	17.602	15.634	101204.000	82.758	0.133	0.00981	0.06166	0.151	0.326	30.837	20.740	0.00235	639.541
6.254	-7.995	8.336	20.347	41.720	101203.089	82.369	0.125	0.01001	0.06287	0.249	0.496	30.791	21.135	0.00233	650.754
5.423	-7.863	12.102	20.353	87.919	101203.444	82.507	0.108	0.00981	0.06163	0.361	0.634	30.872	20.926	0.00233	646.039
4.148	-7.129	17.117	20.353	175.897	101202.578	83.945	0.080	0.00859	0.05397	0.502	0.743	30.868	19.023	0.00233	587.209
3.601	-6.590	18.611	20.522	207.465	101201.889	83.552	0.070	0.00803	0.05048	0.548	0.763	30.879	17.382	0.00232	536.725
2.839	-5.731	20.409	19.649	250.676	101202.000	83.042	0.056	0.00704	0.04423	0.605	0.763	30.773	14.876	0.00234	457.767
2.136	-4.815	21.639	20.809	280.669	101201.000	82.046	0.043	0.00608	0.03822	0.649	0.733	30.838	12.172	0.00233	375.358
0.204	-2.247	28.755	21.029	495.241	101203.000	89.440	0.003	0.00239	0.01502	0.791	0.183	30.856	6.537	0.00232	201.718

GTech Four Blade 6000 RPM															
Fz (lbf)	Mz (in-lb)	Velocity (m/s)	Temp (C)	q (Pa)	Baro P (pa)	RPS	CT	CQ	CP	J	Efficiency	Voltage	Current	Rho(slugs /ft^3)	Power Input (W)
9.770	-11.477	6.260	20.760	23.495	101214.000	99.535	0.134	0.00985	0.06187	0.155	0.336	30.803	38.437	0.00233	1183.987
8.973	-11.495	9.786	20.667	57.445	101217.000	98.698	0.125	0.01003	0.06301	0.244	0.485	30.810	38.952	0.00233	1200.132
7.790	-11.492	13.805	20.640	114.318	101215.844	98.197	0.110	0.01013	0.06363	0.346	0.597	30.791	38.121	0.00233	1173.772
5.898	-10.566	20.291	20.831	246.378	101213.178	100.129	0.080	0.00898	0.05640	0.499	0.709	30.892	34.938	0.00232	1079.279
4.941	-9.588	22.085	20.960	292.235	101212.356	99.052	0.069	0.00831	0.05224	0.549	0.720	30.876	30.574	0.00233	943.996
4.124	-8.820	24.687	21.609	364.939	101210.178	100.993	0.055	0.00736	0.04626	0.601	0.731	30.867	28.347	0.00232	874.989
0.488	-4.409	35.115	21.422	736.370	101209.000	109.296	0.006	0.00315	0.01980	0.791	0.223	30.780	13.509	0.00232	415.804

Acoustic Wind Tunnel Results

GT Propeller Four Blade 11ms			GT Propeller Four Blade 22ms		
RPM	Un- weighted dB	A-weighted dB	RPM	Un- weighted dB	A-weighted dB
4800	88.9025	81.4547	4800	96.7324	87.4324
5400	90.6592	81.7328	5400	100.0076	87.2932
6000	89.8084	79.8437	6000	95.82	85.7434
6300	91.3078	80.3674	6600	95.7079	85.901

GT Propeller Four Blade SPLA 0 m/s		
RPM	Un- weighted dB	A-weighted dB
4300	86.7732	78.8089
4600	88.9506	78.9816
4900	92.0281	79.721
5200	89.0445	80.5823
5400	92.1146	81.2461

Anechoic Chamber Acoustic Results

GT Propeller Four Blade					
Nominal RPM	Actual RPM	SPL dB @ 0 deg	SPL dB @ 22.5 deg	SPL dB @ 45 deg	Thrust (lb)
4000	4118.1336	66.5792	72.7286	76.0543	4.4648
4300	4298.3776	68.0466	74.0943	77.3824	4.9322
4600	4639.9887	69.4637	75.2654	78.5994	5.6618
4900	4992.9422	71.4711	77.2813	80.4376	6.5483
5200	5218.8610	72.7976	78.5261	81.5203	7.1840
5500	5521.3709	74.7656	80.2702	83.0034	8.2334
5800	5752.8047	75.4569	80.7323	83.6446	8.7419
6100	6080.4078	76.7428	81.7867	84.5327	9.7609
6300	6153.9803	77.6986	82.7736	85.3541	10.1518

VITA

Brian Edward Duvall was born in Charlottesville, Virginia, on January 7, 1991. During his years in high school he became interested in dynamics and decided to continue his education at Old Dominion University (ODU) to learn more. At ODU, Brian completed the curriculum for a B.S. degree in mechanical engineering. In his last year in the mechanical engineering program he became interested in model aircraft which led him to pursue a M.S. degree in Aerospace engineering and continue at ODU. While Brian was pursuing his M.S. degree, he was able to help the Old Dominion University team compete in the Society of Automotive Engineering Aero East Design competition. This allowed him to further his knowledge of aircraft design and apply what he learned in the classroom to real life. He helped the 2016 team place sixth out of thirty eight international teams. Brian received his M.S degree in Aerospace engineering in August 2016.